

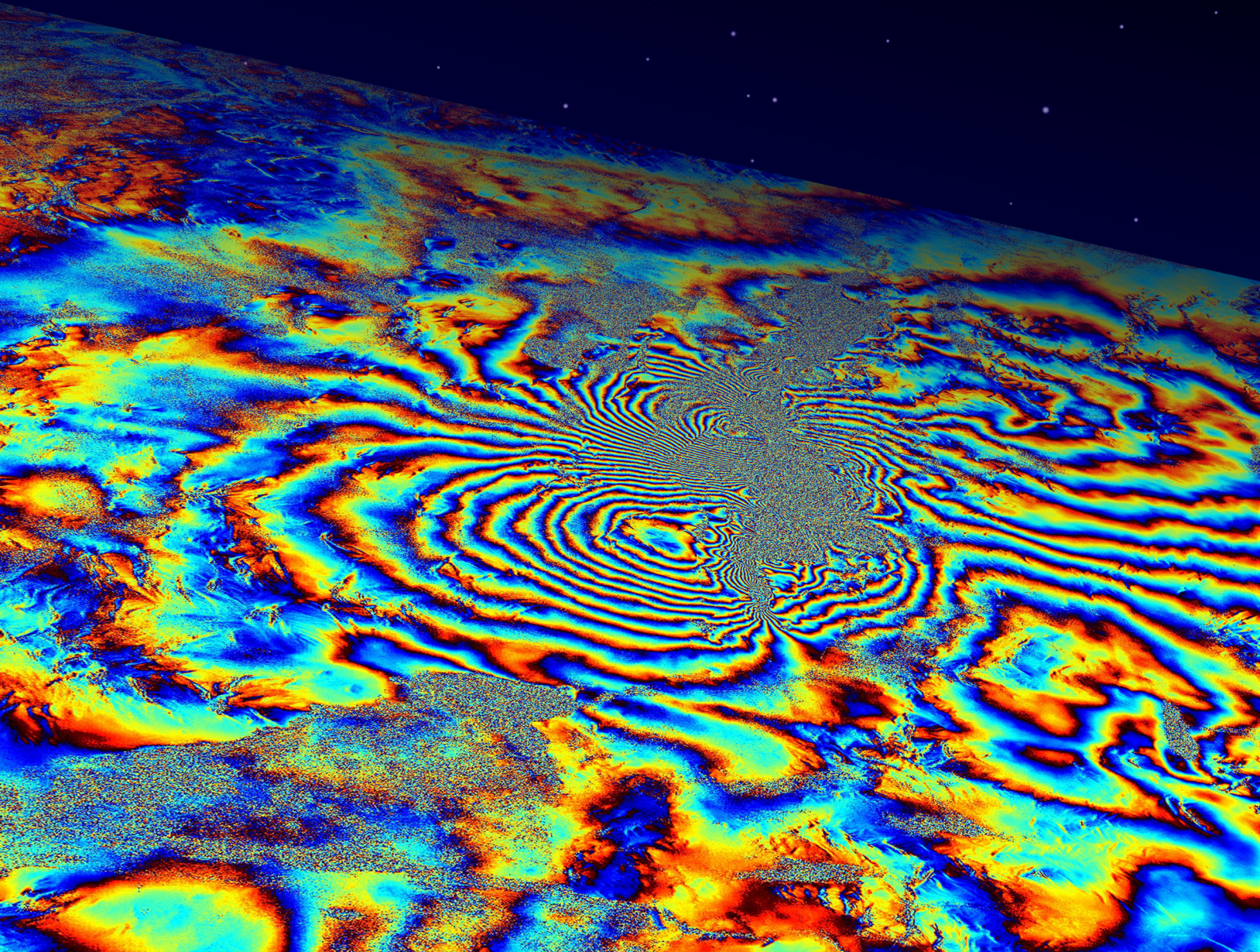


---

# EARTHQUAKE SLIP DISTRIBUTION INVERSIONS USING SYNTHETIC APERTURE RADAR INTERFEROMETRY

---

Sabine Put



**Cover illustration:**

- Ascending interferogram from ERS-2 SAR images acquired at November 12, 1995 and November 21, 1999, covering the Hector Mine earthquake in California, USA.
- Artist impression of the ERS-2 satellite (credits: EADS Astrium).



**INVERSION OF EARTHQUAKE SLIP DISTRIBUTIONS  
USING SYNTHETIC APERTURE RADAR INTERFEROMETRY**

---

**M.Sc. Thesis**

Sabine Put  
M.Sc. Geomatics  
Department of Earth Observation and Space Systems  
Delft University of Technology

December 16, 2008





# Contents

<b>Preface</b>	<b>ix</b>
<b>Summary</b>	<b>xi</b>
<b>Nomenclature</b>	<b>xiii</b>
<b>1 Introduction</b>	<b>1</b>
1.1 Motivation and research objectives . . . . .	1
1.2 Research methodology . . . . .	3
1.3 Thesis outline . . . . .	3
<b>2 Earthquakes</b>	<b>5</b>
2.1 Fault plane terminology . . . . .	5
2.2 Earthquake types . . . . .	6
2.2.1 Normal faults . . . . .	7
2.2.2 Reverse faults . . . . .	7
2.2.3 Transform faults . . . . .	7
2.2.4 Oblique faults . . . . .	7
2.3 Damage from earthquakes . . . . .	8
<b>3 Earthquake observation methods</b>	<b>9</b>
3.1 Seismology . . . . .	9
3.1.1 Types of elastic waves . . . . .	9
3.1.2 Determination of earthquake location and depth . . . . .	10
3.1.3 Fault plane solutions . . . . .	10
3.1.4 The moment magnitude scale . . . . .	11
3.1.5 Seismic data for earthquake slip distribution estimations . . . . .	12
3.2 Synthetic Aperture Radar Interferometry . . . . .	12
3.2.1 Principles of SAR and InSAR . . . . .	12
3.2.2 InSAR processing . . . . .	14
3.2.3 Interferogram interpretation . . . . .	16
3.2.4 Error sources . . . . .	17
3.3 Single-point surface deformation measurements: GPS and leveling . . . . .	18

<b>4</b>	<b>Earthquake slip distribution inversions</b>	<b>19</b>
4.1	Fault parameterization and Okada model . . . . .	20
4.2	InSAR observations . . . . .	21
4.2.1	Image selection and processing . . . . .	21
4.2.2	Data reduction . . . . .	21
4.2.3	Weighting the observations . . . . .	22
4.3	Determination of the fault plane geometry . . . . .	23
4.4	Division of the fault plane in patches . . . . .	24
4.5	Earthquake slip distribution estimation . . . . .	24
4.5.1	Additional constraints . . . . .	25
4.5.2	Inversion: Least-Squares Estimation (LSE) . . . . .	27
4.6	Slip distribution visualization and further analysis . . . . .	28
<b>5</b>	<b>Influence of errors in fault plane geometry and atmospheric delay variations in observations</b>	<b>29</b>
5.1	Synthetic InSAR data . . . . .	29
5.2	Smoothness constraint . . . . .	32
5.3	Influence of errors in fault plane orientation . . . . .	35
5.4	Influence of errors in fault plane position . . . . .	39
5.5	Influence of errors in fault plane dimensions . . . . .	41
5.6	Influence of atmospheric delay variations . . . . .	42
5.6.1	Methodology . . . . .	42
5.6.2	Results and discussion . . . . .	43
5.7	Summary and concluding remarks . . . . .	44
5.7.1	Errors in fault plane geometry . . . . .	44
5.7.2	Errors in observations due to atmospheric delay variations . . . . .	46
<b>6</b>	<b>Case study on the 1999 Hector Mine earthquake</b>	<b>47</b>
6.1	Tectonic setting and earthquake characteristics . . . . .	47
6.2	InSAR data . . . . .	48
6.3	Slip distribution estimation . . . . .	50
6.3.1	Determination of the fault plane geometry . . . . .	50
6.3.2	Smoothness constraint: trade-off between misfit and roughness . . . . .	50
6.3.3	Fault plane orientation optimization . . . . .	52
6.3.4	Comparison with previous research . . . . .	54
6.4	Influence of applied data reduction technique . . . . .	55
6.4.1	Results with uniform resampling . . . . .	55
6.4.2	Results with quad-tree partitioning . . . . .	56
6.5	Summary and concluding remarks . . . . .	58
6.5.1	Hector Mine slip distribution inversion . . . . .	58
6.5.2	Influence of different methods and degrees of data reduction . . . . .	58

<b>7</b>	<b>Conclusions and recommendations</b>	<b>61</b>
7.1	Conclusions . . . . .	61
7.1.1	Sensitivity to errors in fault plane geometry . . . . .	61
7.1.2	Sensitivity to atmospheric errors in observations . . . . .	62
7.1.3	Sensitivity to the number and spatial distribution of observations . .	62
7.2	Recommendations . . . . .	63
7.2.1	Smoothness constraint: an alternative approach . . . . .	63
7.2.2	Optimal data reduction . . . . .	63
7.2.3	General resolvability of slip distributions . . . . .	64
7.2.4	Other improvements and additions to this study . . . . .	64
	<b>References</b>	<b>65</b>
<b>A</b>	<b>Selection of inversion results for the synthetic transform fault</b>	<b>69</b>
<b>B</b>	<b>Inversion results for Hector Mine with different data reduction</b>	<b>79</b>





# Preface

The whole process of writing this final M.Sc. thesis can actually be seen as a jigsaw puzzle. Over time you have gathered a lot of different pieces that somehow fit together, but when you start the puzzle you do not see how they should fit. You normally start with solving the edge of the puzzle, which for me corresponds to the introduction and an outline of the rest of the thesis. When you are composing these boundary pieces the whole view of the puzzle starts to become clear. Then you continue to solve the puzzle by putting the remaining pieces together – the individual chapters and sections. This preface is actually the last piece, making the puzzle complete while adding your last personal touch to it.

All jigsaw pieces have been created in the past year, during my graduation project for the M.Sc. programme in Geomatics. To make sure these pieces were cut in the right shapes, Ramon Hanssen and Gertjan van Zwieten supervised my project. I thank them for all the inspiring conversations and the ongoing exchange of ideas that shaped this research and my way of academic thinking. Furthermore, I would like to thank Mahmut Arikan for answering all my ‘short questions’ – that often turned out to take hours to answer – and the rest of the Radar Remote Sensing group of Delft University of Technology for all their practical advice and comments, including fellow M.Sc. students who have often given me a hand solving Matlab issues. I also thank Sandra Verhagen and Dennis Odijk for their advice on linear estimation theory, and Freysteinn Sigmundsson for reflecting on my work and ideas during his visit to Delft. Finally, thanks go to Martijn de Milliano for his patience while listening to and commenting on hours of earthquake and radar talk at home, and for his practical help with programming.

Although this research is only a very small part of an enormous jigsaw puzzle, I hope my work can contribute to the research of Earth scientists and geo-engineers that are concerned with earthquake studies using Synthetic Aperture Radar Interferometry.

*Sabine Put  
Delft, December 2008*





# Summary

The research presented in this thesis focuses on the inversion of earthquake slip distributions using surface deformation observations. A slip distribution shows the variable amount of displacement in a certain direction on a fault plane that caused the earthquake. Slip distributions are used to study the general characteristics of earthquakes, or to investigate stress changes in the surrounding environment. Furthermore, slip distributions may show areas on the fault plane that have not yet moved, but which may move in the future. The information that can be deduced from slip distributions can be used to point out areas of potential earthquake hazard.

Synthetic Aperture Radar Interferometry (InSAR) can be used to study earthquakes from space. With InSAR, deformation can be observed in a certain area and time period by making use of repeat-pass interferometry. This makes it possible to observe coseismic deformation that is caused by earthquakes. These observations can be used in the inversion of earthquake slip distributions by using the ‘Okada model’. Okada (1985) presented a complete set of analytical expressions that relate slip on finite rectangular fault planes to surface displacements. Given this model and information about the fault plane geometry of the earthquake, the estimation of the slip distribution is a linear inverse problem.

The fault plane geometry required for the slip distribution inversion can be determined from a combination of seismic data and the InSAR data itself. However, errors in fault plane geometry will result in errors in the estimated slip distribution. To investigate the influence of errors in fault plane geometry on the estimated slip distribution, synthetic interferograms are created that correspond to three different earthquake types. It is found that in general, the sensitivity of the slip distribution estimation to errors in fault plane geometry depends on the orientation of the fault plane, the earthquake type, and the satellite viewing geometry. Since this information is available prior to the actual inversion procedure, deducing the fault plane geometry parameters for which the sensitivity of the slip distribution estimation is largest can be used to facilitate the choice of InSAR data or to prioritize the optimization of certain parameters over others.

The result of the slip distribution inversion does not only depend on the assumed fault plane geometry, but also on the quality of the observations. An important source of errors in InSAR observations are spatial and temporal variations in atmospheric delay. The influence of these errors is examined by estimating the slip distribution for many different synthetic interferograms containing atmospheric signals only. It is found that under normal weather conditions, the effect of atmosphere is negligible for large earthquakes (with a magnitude equal to or larger than the magnitude of the studied earthquakes).

A case study is performed on the 1999 Hector Mine earthquake (California). Two ascending ERS-2 images are used to estimate the slip distribution. The results correspond well to those found in other research in terms of slip distribution pattern and magnitude. For this earthquake, results are also compared for different methods and degrees of data reduction. The degree and method of data reduction is a case-dependent trade-off between

acceptable information loss, noise reduction, and available computational time. Slip distributions are estimated with both uniformly resampled and quad-tree partitioned data. It is found that the slip distribution estimation is sensitive to the spatial distribution of the observations, but not to the number of observations. Furthermore, if the quad-tree threshold and minimum number of observations to merge are chosen such that detail is preserved while at the same time noise is reduced, an increase in efficiency in terms of computational time and memory requirements can be achieved by using quad-tree partitioning (as opposed to uniform resampling).

# Nomenclature

## List of acronyms

<b>CMT</b>	Centroid Moment Tensor
<b>DEM</b>	Digital Elevation Model
<b>DORIS</b>	Delft Object-oriented Radar Interferometric Software
<b>ECSZ</b>	Eastern California Shear Zone
<b>ERS</b>	European Remote sensing Satellite
<b>ESA</b>	European Space Agency
<b>GPS</b>	Global Positioning System
<b>InSAR</b>	Synthetic Aperture Radar Interferometry
<b>LOS</b>	Line-Of-Sight
<b>LSE</b>	Least-Squares Estimation
<b>NF</b>	Normal Fault
<b>NNLS</b>	Non-Negative Least-Squares estimation
<b>QT</b>	Quad-Tree partitioning
<b>RF</b>	Reverse Fault
<b>RMSE</b>	Root-Mean-Squared Error
<b>SAR</b>	Synthetic Aperture Radar
<b>SLC</b>	Single-Look Complex
<b>SNAPHU</b>	Statistical-cost, Network-flow Algorithm for PHase Unwrapping
<b>SNR</b>	Signal-to-Noise Ratio
<b>SRTM</b>	Shuttle Radar Topography Mission
<b>TF</b>	Transform Fault
<b>UR</b>	Uniform Resampling
<b>USGS</b>	United States Geological Survey

## List of symbols

<b>A</b>	design matrix
$A_p$	area of the fault plane [m <sup>2</sup> ]
$\alpha$	strike of the fault plane [°]
$B_r$	range bandwidth [MHz]
$c$	speed of light [ms <sup>-1</sup> ]
$C(p_1, p_2)$	covariance of patch $p_1$ and patch $p_2$
$C_l$	correlation length, [m] or [km]
$c_M$	constant for moment magnitude computation
$d$	LOS deformation, [m] or [cm]



$d_{min}, d_{max}$	minimum and maximum depth of the fault plane [km]
$\text{dist}(p_1, p_2)$	Euclidean distance between patch $p_1$ and patch $p_2$ , [m] or [km]
$\delta$	dip of the fault plane [°]
$\Delta$	symbol indicating the error in a fault plane geometry parameter
$e$	error vector
$\varepsilon_m$	RMSE of the misfit between model and observations, [m] or [cm]
$\varepsilon_{sd}$	RMSE of the slip distribution [m]
$E\{\}$	expectation operator
$f, f_0$	variable and normalized angular wave number [cycle/km]
$f_w$	Laplacian smoothness weight
$\mathbf{I}$	identity matrix
$L$	length of the fault plane along strike [km]
$\lambda_L$	Lamé constant (first parameter)
$\lambda_R$	radar wavelength [m]
$m$	number of observations
$M_0$	seismic moment, [Nm] or [dyn·cm]
$M_W$	moment magnitude
$\mu_L$	Lamé constant or shear modulus of rigidity (second parameter) [Nm <sup>-2</sup> ]
$n$	number of patches
$\nu$	Poisson's ratio
$p_\alpha, p_\delta$	patch size in strike and dip direction [km]
$p_{k,l}$	$k$ -th patch in strike direction and $l$ -th patch in dip direction
$P(f)$	power as a function of angular wave number (part of the atmospheric model)
$P_0, P_I, P_{III}$	power law scaling parameters (part of the atmospheric model)
$\Psi$	(unwrapped) interferometric phase [rad]
$Q_{dd}$	variance-covariance matrix of (InSAR) observations
$Q_{pp}$	a-priori variance-covariance matrix of the slip distribution
$Q_{\hat{s}\hat{s}}$	variance-covariance matrix of the estimated slip distribution
$Q_{\nabla\nabla}$	variance-covariance matrix of pseudo observations (smoothness constraint)
$q_{min}, q_{max}$	minimum and maximum size of observation segments [m]
$q_t$	quad-tree partitioning threshold
$R_r$	range resolution [m]
$R_{sd}$	roughness (mean absolute Laplacian) of the slip distribution
$r$	rake (direction) of displacement [°]
$s$	slip distribution vector (amount of displacement) [m]
$s_{k,l}$	slip on the $k$ -th patch in strike direction and $l$ -th patch in dip direction
$\sigma_{\nabla\nabla}^2$	variance of pseudo observations (smoothness constraint)
$t$	radar pulse length [μs]
$\tau$	effective pulse interval [μs]
$\theta_{az}, \theta_i, \theta_l$	satellite azimuth angle, incidence angle, and look angle [°]
$x, y$	x- and y-coordinate of top-center of the fault plane [km]
$\nabla$	smoothness operator (discrete Laplacian)

# Chapter 1

## Introduction

### 1.1 Motivation and research objectives

Since the beginning of history, earthquakes have been one of the world's largest natural hazards. Earthquakes occur daily, varying in size from small vibrations that can barely be detected to very large movements that cause a lot of damage. Prevention of earthquakes is not possible, but preparedness by means of earthquake forecasting can limit damage. Although short-term earthquake forecasts are not and may never become reliable (Marshak, 2001), the study of earthquakes can improve the understanding of the underlying earthquake mechanisms. This in turn can contribute to the identification of areas where earthquakes can potentially occur.

Synthetic Aperture Radar Interferometry (InSAR) can be used to study earthquakes from space. With InSAR, deformation can be observed in a certain area and time period by making use of repeat-pass interferometry. Theoretically, this enables one to observe:

- pre-seismic surface deformation associated with the build-up of strain prior to an earthquake event;
- coseismic surface displacements and deformation caused by an earthquake;
- post-seismic surface deformation and surface displacements associated with after-shocks of an earthquake.

Observed coseismic surface deformation can be used to estimate the earthquake fault plane geometry and distribution of slip on the fault plane at the time of the earthquake event. These parameters describe the earthquake source, which can be used to study earthquake mechanisms. The problem of estimating the earthquake source parameters can be considered as the inverse of the forward model of Okada, who presented a complete set of analytical expressions that relate slip on finite rectangular fault planes to surface displacements in an elastic half-space (Okada, 1985). The result and quality of such an earthquake source inversion are influenced by the chosen inverse model and the observations.

**Inverse model** – going from raw data to estimated source parameters, many assumptions need to be made in the inversion process in order to obtain a unique solution. Some of these assumptions have a physical background (e.g. assuming certain rheological properties of the Earth), others are case-dependent or prone to subjectivity.

**Observations** – errors in the observed surface deformation will have a certain influence on the earthquake source estimation. For example, the observations may be affected by differences in atmospheric delay, or errors may be introduced during interferometric processing. The impact of errors in observations on the estimated source parameters depends on the propagation of these errors through the inversion procedure.

A number of studies have already been performed on earthquake source inversions with InSAR data, based on Okada’s forward model. Massonnet and Feigl (1998) simplify the problem of earthquake source inversions by dividing it into two parts:

1. estimation of the fault plane geometry assuming uniform slip on the fault plane;
2. division of the fault plane in patches and estimation of the slip on each patch for a fixed geometry, i.e. estimation of the slip distribution.

The first part, estimating the fault plane geometry, is a non-linear problem in which the fault plane location, dimensions, and orientation are estimated. The second part, estimating the slip distribution for a given geometry, is a linear problem. To bypass the non-linear estimation part (which is not straight-forward and rather computationally expensive), the fault plane geometry parameters can be fixed in the inversion procedure. The information required to fix these parameters can be obtained from seismic data – which is commonly made available shortly after an earthquake occurs – and from examination of the interferogram itself.

This study focuses on the second part of the earthquake source inversion: estimating the slip distribution for a fixed fault plane geometry. Slip distributions not only give insight into the earthquake event, they can also be used to investigate stress changes in the surrounding environment and to identify fault plane areas that have not moved during an earthquake event. This information can be used to assess the risk of future earthquakes in a certain area.

The fault plane geometry will be fixed based on both seismic data (the Harvard Centroid Moment Tensor solution) and visual interpretation of the interferogram. The sensitivity of the slip distribution estimation to errors in fault plane geometry assumptions and errors in observations is examined. The general research question is therefore defined as follows:

*What is the influence of errors in fault plane geometry and errors in observations on earthquake slip distribution estimations using InSAR?*

More specifically, an inversion algorithm based on Okada’s forward model is developed to investigate the sensitivity of the estimated slip distribution to:

1. errors in chosen fault plane geometry (research objective 1);
2. errors in the InSAR observations caused by spatial and temporal variations in atmospheric delay (research objective 2);
3. the number and spatial distribution of observations (research objective 3).



## 1.2 Research methodology

The research objectives 1, 2 and 3 defined above are investigated with synthetic earthquake data and with real earthquake data. The synthetic data set consists of ‘perfect’ interferograms that are computed for pre-defined slip distributions with Okada’s forward model. The real data is from the Hector Mine earthquake that occurred in California on October 16, 1999. This earthquake has been selected as test area because it has already been studied extensively, for example by Fialko et al. (2001), Jónsson (2002) and Salichon et al. (2004). This makes it possible to compare the results of this study with the results of previous research.

Research objective 1 is investigated with synthetic data. The use of synthetic InSAR data instead of real InSAR data has the advantage that the correct fault plane geometry and slip distribution are known, which makes it possible to assess the sensitivity of the slip distribution to errors in the orientation, location, and dimensions of the fault plane with respect to the satellite viewing geometry. The results of this part of the research will be used to optimize the fault plane geometry of the Hector Mine earthquake.

The approach to investigate research objective 2 is to apply the inversion algorithm to synthetic interferograms containing atmospheric signals only. For each interferogram, the estimated slip distribution will reflect the error caused by spatial and temporal variations in atmospheric delay. This relatively simple approach is justified because the inversion of slip for a given fault plane geometry is linear. The synthetic interferograms are created with an existing algorithm based on the theory of typical atmospheric behavior as presented by Hanssen (2001).

Research objective 3 is investigated with use of an interferogram covering the Hector Mine earthquake. The number and spatial distribution of observations depends on the method and amount of data reduction that is applied to the interferogram, which is a trade-off between several factors such as computational time, acceptable information loss, and noise reduction. The result of this trade-off is likely to have an influence on the estimated slip distribution. Therefore, slip distribution estimations are compared that are obtained with two different methods of data reduction (uniform resampling and quad-tree partitioning) and for different degrees of data reduction.

## 1.3 Thesis outline

The structure of this thesis is as follows.

- Chapter 2 explains basic earthquake and fault plane terminology and introduces the four main earthquake types that are distinguished.
- Chapter 3 provides a brief introduction to different earthquake observation methods. This chapter covers the basic principles of seismology and InSAR, and discusses their role in earthquake studies.
- Chapter 4 presents the proposed earthquake slip inversion procedure. This chapter can serve as a reference to facilitate future implementations of the inversion procedure.
- Chapter 5 covers the methodology and results associated with research objective 1 and research objective 2. The effect of errors in fault plane geometry on the estimated slip distribution is investigated. Furthermore, the influence of atmospheric delay variations in the observations is examined.

- Chapter 6 describes the methodology and results of the case study of the 1999 Hector Mine earthquake. The fault plane geometry is optimized based on the results of the investigation of research objective 1. The remainder of this chapter focuses on the effect of the number and spatial distribution of observations (research objective 3).
- Finally, Chapter 7 gives an overview of the conclusions of this work and recommendations for future research on this topic.

## Chapter 2

# Earthquakes

Earthquakes are movements in the upper layers of the Earth that result from the sudden release of built-up strain energy. A distinction can be made between shallow-focus earthquakes (less than 70 km deep), intermediate-focus earthquakes (at 70–300 km depth) and deep-focus earthquakes (at 300–720 km depth). There is no earthquake activity in areas deeper than  $\pm 720$  km, because the mantle becomes increasingly ductile with depth (Marshak, 2001). Of these three types, shallow-focus earthquakes generally cause most damage at the Earth’s surface, due to the limited spread and dissipation of the strain energy when the earthquake focus is close to the surface.

Most earthquakes are grouped together in seismic zones that are located at plate boundaries, although intra-plate earthquakes occur as well. The most common types of plate boundaries are continental rift zones, mid-oceanic spreading ridges, continent-continent collision zones, subduction zones, and lateral plate boundaries (Marshak, 2001). Some examples of these typical tectonic settings for earthquakes are illustrated in Figure 2.1. Plate boundary tectonics cause mainly shallow-focus earthquakes. However, subduction zones are an exception where also intermediate-focus and deep-focus earthquakes occur due to the geometry of this type of plate boundary (one plate dips below the other plate).

The faults on which movement occurs are either newly formed or already existing faults. The length of a fault can reach up to more than 1000 kilometers (e.g. the 2004 Indian Ocean earthquake). The depth extent of the fault is usually in the order of (tens of) kilometers for shallow-focus earthquakes (Marshak, 2001).

Four main fault geometry types can be distinguished that determine the type of earthquake. After an introduction in fault terminology in Section 2.1, these earthquake types are discussed in Section 2.2. This chapter concludes with a short note on damage caused by earthquakes in Section 2.3.

### 2.1 Fault plane terminology

Many faults intersect with the Earth’s surface; these faults are known as *rupturing faults*. The line of intersection is the *fault trace*, also referred to as the *fault line*. Vertical outcrops at the Earth’s surface that are caused by faults are known as *fault scarps*. Faults that do not extend to the surface are *blind faults* (Marshak, 2001).

The orientation of the fault plane is determined by its strike and dip (see also Figure 4.2, Chapter 4). The *strike* is the orientation of the fault trace relative to a fixed azimuth direction. By convention, the strike is the angle between the fault trace and the North with the layer dipping to the right-hand side (Aki and Richards, 1980). The *dip* is the angle

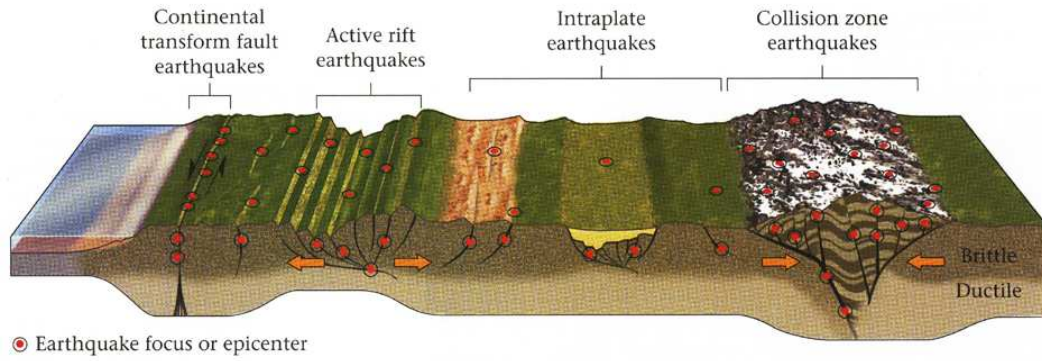


Figure 2.1: Examples of typical tectonic settings for earthquakes (adapted from Marshak (2001)). The orange arrows indicate the direction of regional plate tectonic movements. The black lines show the locations of faults.

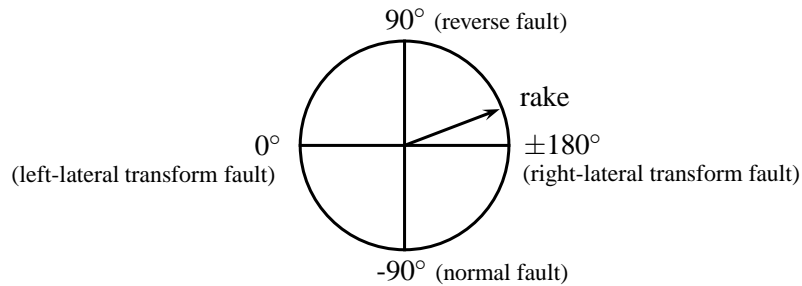


Figure 2.2: Rake corresponding to different fault types.

between a horizontal surface and the surface of the fault (defined between  $0^\circ$  and  $90^\circ$ ). For faults with a dip smaller than  $90^\circ$ , a distinction can be made between the footwall and the hanging wall of a fault. The *footwall* is the side of the fault that is located below the *hanging wall* (see Figure 2.3a and Figure 2.3b). The amount of relative displacement between both sides of the fault is the *slip*, commonly expressed in meters. The *rake* is the direction of slip (hanging wall relative to footwall, or the right side of the fault in strike direction in case of a dip of  $90^\circ$ ), expressed as an angle between  $-180^\circ$  and  $180^\circ$ . The rake determines the type of earthquake (Figure 2.2). An upward movement of the hanging wall corresponds to a rake of  $90^\circ$ , a downward movement corresponds to a rake of  $-90^\circ$ . Left-lateral movements have a rake of  $0^\circ$ , right-lateral movements have a rake of  $\pm 180^\circ$ .

## 2.2 Earthquake types

The type of earthquake is related to the tectonic setting of the area. In general, earthquakes located in spreading areas will be of a different type than earthquakes occurring in subduction zones. Different earthquakes are caused by slip on normal faults, reverse faults, transform faults, and oblique faults. The type of earthquake is determined by the rake.

### 2.2.1 Normal faults

*Normal faults* are caused mainly by tension. During normal faulting, the hanging wall slides down the footwall (Figure 2.3a). This type of earthquake occurs in diverging regions where tension is built, for instance at mid-oceanic spreading ridges and in continental rift zones such as the East African Rift. A pure normal fault has no slip in the direction of its strike (strike-slip), but only in the direction of its dip (dip-slip). Normal faults have a rake of  $-90^\circ$ .

### 2.2.2 Reverse faults

A *reverse fault* (also referred to as *thrust fault*) is caused mainly by compression. During reverse faulting, the hanging wall is thrust up the footwall, causing a relative uplift at the side of the hanging wall (Figure 2.3b). This is the opposite of a normal fault. As with a normal fault, a pure reverse fault has only dip-slip, but with a rake of  $90^\circ$ . Although the terms thrust fault and reverse fault are commonly interchanged, sometimes a distinction is made in which reverse faults have a large dip (the fault plane is more vertical) and thrust faults have a small dip (more horizontal). Both reverse and thrust faults commonly occur at locations where plates converge. This is for instance the case in subduction zones such as in Alaska and continent-continent collision zones such as the Himalayas.

### 2.2.3 Transform faults

A *transform fault* is a lateral movement, where slip occurs only along the strike of the fault (Figure 2.3c). Therefore, a transform fault is commonly referred to as a *strike-slip fault*. A distinction can be made between left-lateral (with a rake of  $0^\circ$ ) and right-lateral transform faults (with a rake of  $\pm 180^\circ$ ). In a *left-lateral* transform fault, from both sides of the fault the opposite side appears to move to the left. In a *right-lateral* transform fault, from both sides of the fault the opposite side appears to move to the right. Transform faults are common in many tectonic settings, for instance between different mid-oceanic spreading ridge segments or at lateral continent-continent boundaries such as the San Andreas Fault through California.

### 2.2.4 Oblique faults

*Oblique faults* are combinations between either normal faults and transform faults, or reverse faults and transform faults. Oblique faults have thus both strike-slip and dip-slip components of slip that have a similar order of magnitude. These faults occur at oblique plate boundaries, such as the Alpine Fault zone in New Zealand.

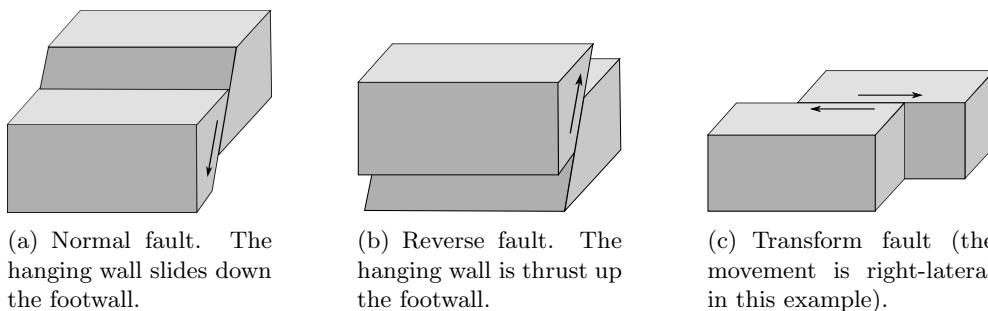


Figure 2.3: Schematic representation of fault types. The arrows indicate the direction of movement.

## 2.3 Damage from earthquakes

Local or regional damage caused by earthquakes can be divided into direct damage and indirect damage.

Direct damage is caused by displacements and ground shaking that can vary in amplitude from several centimeters for moderate earthquakes to a few meters for large earthquakes (Marshak, 2001). Figure 2.4 shows an aerial photograph of a part of the fault trace and typical surface displacements caused by the 1999 Hector Mine earthquake. These surface displacements are in the order of a few meters.

Indirect damage is caused by e.g. earthquake-triggered landslides (Figure 2.5), avalanches, and fires; tsunami; seiche (rhythmic water movements that can occur thousands of kilometers away from the earthquake focus); and sediment liquefaction, which is the disintegration of clay to form muddy, unstable substances.

A more elaborated discussion on damage caused by earthquakes and earthquake-triggered processes can be found in Marshak (2001).



Figure 2.4: Aerial photograph of a part of the fault trace and typical surface displacements caused by the 1999 Hector Mine earthquake. Photograph by Paul Otis-Diehl, USGS.



Figure 2.5: Damage caused by a landslide that was triggered by the Niigata Chuetsu Oki earthquake, which occurred in Japan on July 16, 2007. Source photograph: USGS.

## Chapter 3

# Earthquake observation methods

Different techniques exist to observe earthquakes. A distinction can be made between geodetic techniques that are used to measure deformation at the Earth's surface, and seismology, which studies the arrival and properties of elastic waves passing through the Earth. This chapter gives an introduction to seismology in Section 3.1 and InSAR in Section 3.2. Although single-point deformation measurements with geodetic techniques such as GPS and leveling are not used in this study, they can provide additional observations for slip distribution estimations. Therefore, their potential will be covered briefly in Section 3.3.

### 3.1 Seismology

Seismology is the study of elastic waves that pass through the Earth. Earthquake seismology has been of major importance for geological and geophysical investigation, since the location of earthquakes delineates the boundaries of continental and oceanic plates (Fowler, 1990). Earthquake mechanisms can be determined by analyzing elastic waves that are generated by earthquakes, observed at different locations. This section covers the basic principles of seismology. For a more detailed discussion of seismology, the reader is referred to e.g. Aki and Richards (1980) or Fowler (1990).

#### 3.1.1 Types of elastic waves

The strain energy release that causes an earthquake generates two types of elastic waves: body waves and surface waves.

##### Body waves

Body waves are waves that are spread from the earthquake focus. Two types are distinguished: P-waves and S-waves. *P-waves* – where P stands for primary or pressure wave – are longitudinal or dilatational waves. The particle motion of a P-wave is in the same direction as the direction of propagation. *S-waves* – where S stands for secondary or shear waves – are transverse or equivoluminal waves. The particle motion of an S-wave is perpendicular to the direction of propagation and can be split into a horizontal and a vertical component. S-waves do not travel through a liquid medium. This property led to the discovery of the Earth's liquid outer core.

The velocity of P-waves is larger than the velocity of S-waves. The velocities of both P- and S-waves increase with increasing density of the medium through which they travel. This means that in general the velocities increase with increasing depth, except in case of the presence of a low-velocity zone in the Earth's interior such as the transition zone between the Earth's crust and mantle.

## Surface waves

As the name suggests, surface waves propagate along the surface, away from the earthquake. They do not penetrate the deeper interior. Two types of surface waves are *Rayleigh waves* and *Love waves*, which differ in the direction of particle motion: perpendicular to the surface for Rayleigh waves, and parallel to the surface for Love waves. Surface waves have a cylindrical wavefront, hence they are larger in amplitude and longer in duration than body waves, which have a spherical wavefront (Fowler, 1990). Surface waves are the main cause of damage at the Earth's surface.

### 3.1.2 Determination of earthquake location and depth

By recording the arrival time of P- and S-waves of an earthquake at different locations on Earth it is possible to locate this earthquake. The point vertically above the focus of the earthquake is referred to as the earthquake *epicenter*. Theoretically, if the Earth would be flat and homogeneous, measuring the arrival time of P- and S-waves at three seismometers would be sufficient to determine the latitude and longitude of the epicenter, and the time of the earthquake event. However, since the Earth is neither homogeneous nor flat, in practice more seismometers are needed to determine these parameters with reasonable accuracy (Fowler, 1990). The depth of the earthquake focus can be estimated from measurements of the difference in travel time between the direct P-wave arrival and the arrival of a P-wave reflected at the Earth's surface.

### 3.1.3 Fault plane solutions

Examining the direction of movement of the seismic P-waves that arrive at different seismic stations makes it possible to reconstruct the type of earthquake and reduce the number of possible orientations of the fault plane to only two. This is illustrated in Figure 3.1. A transform fault is taken as an example here, with six seismic observations, measured at locations A to F. These locations correspond to the angle from which the wave departed from the earthquake focus, projected on the virtual lower hemisphere of the focus. The 'first arrival' is either positive (compressional: A, C, and E), negative (dilatational: B and F), or no wave is received at all (D). With many observations, quadrants can be formed that correspond to areas with only positive arrivals and negative arrivals. Two planes form these quadrants: the real fault plane and the *auxiliary plane*, which is a virtual plane without physical meaning. The quadrants can then be displayed as a *fault plane solution*, with areas with positive arrivals indicated in black and areas with negative arrivals in white.

In this example the fault is an East-West oriented right-lateral fault, but based on the fault plane solution alone it cannot be decided whether this is an East-West or North-South oriented fault. Additional information is needed (such as a mapped fault trace in case of a rupturing fault) to decide which plane is the actual fault plane. Fault plane solutions for typical transform, normal, reverse, and oblique faults are shown in Figure 3.2.



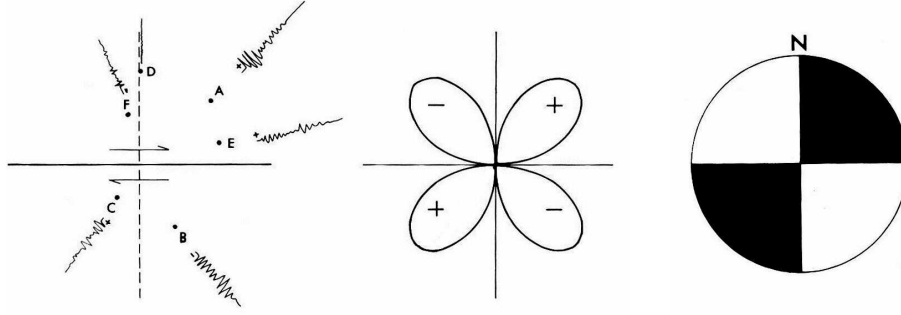


Figure 3.1: Determination of the earthquake type and possible geometry with seismic observations (adapted from Fowler (1990)). Left figure: A, C, and E correspond to positive arrivals (compression); B and F to negative arrivals (dilatation). Quadrants can be formed if a sufficient number of observations is available (middle figure). This can then be visualized as a fault plane solution (right figure).

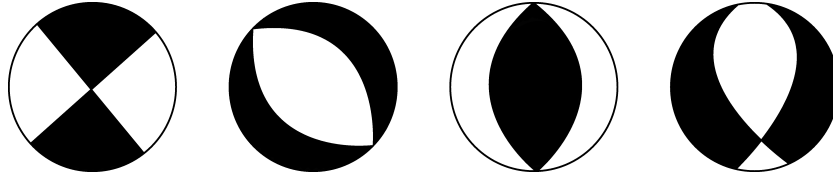


Figure 3.2: Typical fault plane solutions for the four main earthquake types. From left to right: transform fault, normal fault, reverse fault, and oblique fault.

### 3.1.4 The moment magnitude scale

Two types of scales are used to describe the magnitude of earthquakes: magnitude scales and intensity scales. *Magnitude scales* are based on measurements of the amplitude of the seismic waves generated by earthquakes, such as Richter's scale and the moment magnitude scale. *Intensity scales* are subjective scales that are based on 'measurements' of the amount of damage on the Earth's surface, such as Mercalli's scale. Widely used is the *moment magnitude scale*, which is based on the seismic moment of an earthquake. The moment magnitude  $M_W$  was introduced by Hanks and Kanamori (1979) and reads:

$$M_W = \frac{2}{3} (\log_{10}(M_0) - c_M), \quad (3.1)$$

where  $M_0$  is the seismic moment of an earthquake and  $c_M$  is a constant which value depends on the unit of  $M_0$ :  $c_M = 9.1$  if  $M_0$  is in [Nm], and  $c_M = 16.1$  if  $M_0$  is in [dyn-cm]. The *seismic moment* is defined as  $M_0 = \mu_L A_p s$ , with  $\mu_L$  the shear modulus of rigidity,  $A_p$  the area of the fault plane, and  $s$  the average slip on the fault plane. The seismic moment is determined from estimates of the fault plane area and slip or from low-frequency amplitude spectra of surface waves (Fowler, 1990). The coefficients in Equation (3.1) are chosen such that the magnitude values are in approximately the same range as those obtained with other magnitude scales (such as Richter's scale).

### 3.1.5 Seismic data for earthquake slip distribution estimations

Seismic data can be used to constrain the fault plane geometry in the estimation of earthquake slip distributions. The strike, dip, rake, and location listed by the Harvard Centroid Moment Tensor (CMT) catalog can be used for this purpose. The use of seismic data in this study will be discussed further in Chapter 4.

Seismic data can also be used to perform a joint inversion of a slip distribution with InSAR observations, or to validate results. Such a joint inversion is applied for the 1999 Hector Mine earthquake by Kaverina et al. (2002) and Salichon et al. (2004).

## 3.2 Synthetic Aperture Radar Interferometry

Synthetic Aperture Radar interferometry (SAR interferometry or InSAR) is a remote sensing imaging technique in which two radar images of the same scene are combined to *interferograms*. The three main contributions to the information in an interferogram are:

- topography of the terrain;
- surface deformation caused by natural processes or anthropogenic activity;
- atmospheric signals due to spatial and temporal differences in atmospheric delay.

There are many applications of InSAR, varying from topographic mapping and atmospheric monitoring to the mapping of deformation due to earthquakes, volcanic activity, subsidence, and ice sheet motions. The first earthquake that was studied with InSAR was the Landers earthquake of 1992 in California (Massonnet et al., 1993), where the potential of InSAR to observe coseismic deformation was explored. The possibilities to create three-dimensional coseismic displacement fields were investigated by e.g. Michel et al. (1999) and Fialko et al. (2001), who used a combination between ascending and descending interferometric pairs.

This section gives a basic overview of InSAR to provide the reader with a background in InSAR and the knowledge necessary to understand the remaining chapters of this thesis. For a more detailed (mathematical) discussion of InSAR, see for instance Bamler and Hartl (1998) or Hanssen (2001). For an overview of the geophysical applications of InSAR, see Massonnet and Feigl (1998).

### 3.2.1 Principles of SAR and InSAR

SAR systems are active systems that transmit and receive in the microwave range of the electromagnetic spectrum (with wavelengths in the order of centimeters). One of the main advantages of operating in this range is that radar waves can penetrate the atmosphere. This implies that cloud cover does not obstruct the radar from reaching the Earth's surface, which makes it an 'all-weather' remote sensing system. Moreover, active SAR systems do not depend on solar illumination which makes it possible to operate during day and night.

#### Image formation and resolution

The antenna from a satellite SAR system directs a narrow beam sideways to the Earth's surface with a certain angle from nadir; the *look angle*. For example, ESA's ERS-2 satellite has a look angle  $\theta_l$  of about  $20.5^\circ$  and a corresponding *incidence angle*  $\theta_i$  which is slightly larger ( $\sim 23^\circ$ ), depending on the local curvature of the Earth's surface. ERS-2 covers a

scene of roughly  $100 \times 100$  km. Specifications of ERS-2 and some other radar remote sensing satellites are given in Table 3.1.

While the satellite platform is moving, the SAR antenna sends radar pulses with a predefined rate and length, the pulse repetition frequency and pulse length, respectively. With a pulse length  $t$ , the *range resolution*  $R_r$  (the minimum distance in range at which two objects can be distinguished) equals the distance that a radar pulse travels in half the pulse length:

$$R_r = \frac{1}{2}ct, \quad (3.2)$$

where  $c$  is the speed of light. With a pulse length of  $t = 37.1 \mu\text{s}$  for ERS-2, this would correspond to a range resolution of approximately 5.6 km in range direction and approximately 14 km in ground range. To increase this resolution, pulses are sent with varying frequency (within a bandwidth), resulting in an effective pulse interval  $\tau$  of:

$$\tau = 1/B_r, \quad (3.3)$$

with  $B_r$  the range bandwidth. For ERS-2, which has a bandwidth of 15.55 MHz, this results in an effective range resolution of approximately 9.6 m in range direction and approximately 25 m in ground direction (Curlander and McDonough, 1991).

A condition for InSAR is that the sensor of the imaging radar is coherent, i.e. the phase needs to be stable between transmitting and receiving the radar pulses (Hanssen, 2001). The received radar signals consist of amplitude and phase information (time delay and phase fraction).

With the redundancy of the subsequent pulse returns from the same objects on the Earth's surface, it is possible to improve the *azimuth resolution*, which is the resolution in the direction of the satellite track. The inverse problem of reconstructing the response of the object from a series of pulse returns is known as SAR *focusing*. See Hanssen (2001) for a list of focusing algorithms and corresponding references. A focused SAR image is also referred to as a *Single-Look Complex* (SLC) image. With two SLC images covering exactly the same area (aligned), an interferogram can be created by complex multiplication of the two images.

Table 3.1: Specifications of a few SAR satellite missions. Compiled from Hanssen (2001), and websites of ALOS (2008), RADARSAT-2 (2008), and TerraSAR-X (2008).

Satellite mission	ALOS	Envisat	ERS-2	RADARSAT-2	TerraSAR-X
Year of launch	2006	2002	1995	2007	2007
Repeat time [days]	46	35	35	24	11
Incidence angle $\theta_l$ [°]	8-60	20-50	$\sim 23$	20-60	20-55
Radar band	L	C	C	C	X
Radar wavelength $\lambda_R$ [cm]	23.6	5.66	5.66	5.66	3.1
Altitude [km]	692	800	790	798	514
Swath [km]	40-350	100-500	100	20-500	10-100
Range bandwidth $B_r$ [MHz]	28/14	14.00	15.55	12-100	150/300

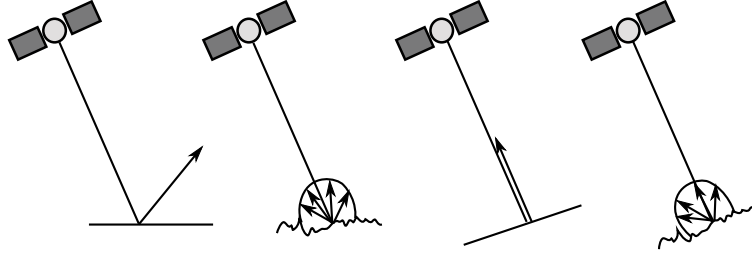


Figure 3.3: Effect of slope and surface roughness on radar signal scattering. From left to right: specular scattering on a smooth, flat surface, resulting in no backscatter; diffuse scattering on a rough, flat surface, resulting in little backscatter; specular scattering on a sloping surface perpendicular the satellite incidence angle, resulting in maximum backscatter; and diffuse scattering on a rough sloping surface, resulting in little backscatter.

### Conditions for InSAR: temporal and perpendicular baseline

SAR systems receive the radar pulses that are scattered from objects on the Earth’s surface. The amplitude of the received signal depends on several factors, such as the slope of the object and its roughness (Figure 3.3).

Scattering does not only influence the amount of energy (amplitude) that is returned to the sensor; it also affects the phase of the signal. One pixel in an SLC image is normally composed of backscatter from many individual objects. Therefore, the behavior of the backscattered phase is unpredictable. However, it may be stable in time (coherent), which is, in fact, a necessary condition for interferometry. Factors such as weathering, vegetation growth, and human-induced changes in the environment result in a change of the scattering behavior of the pixel over time. At some level this change leads to *decorrelation* in the interferogram, i.e. complete loss of coherence. The *temporal baseline*, which is the time between two SAR acquisitions, is therefore a limiting factor in interferometry. The maximum possible temporal baseline before large parts of the interferogram become decorrelated depends on the area of interest. For example, arid, uninhabited areas generally allow for a much larger temporal baseline – in the order of years – than areas with dynamic vegetation cover, which is in the order of weeks (Villasenor and Zebker, 1992). This is an important issue that needs to be considered during SAR image selection.

Another condition for InSAR is a limited perpendicular baseline, which is the distance between two satellite acquisition spots perpendicular to the satellite viewing direction, the Line-Of-Sight (LOS). The larger the perpendicular baseline, the larger the reduction in coherence, until decorrelation occurs at the *critical baseline*. For ERS-2 this critical baseline is approximately 1100 m, depending on the local topography and the gradient of the surface deformation (Hanssen, 2001). A small perpendicular baseline is preferred for the study of surface deformation, because the sensitivity to topography decreases with decreasing perpendicular baseline. This is due to the increase in height ambiguity, which is the height difference corresponding to one phase cycle.

### 3.2.2 InSAR processing

Several software packages exist to process InSAR data. DORIS (Delft Object-oriented Radar Interferometric Software), developed by Delft University of Technology (Kampes and Usai, 1999) is used as processing software for this study. A description of the required and optional processing steps is given in Hanssen (2001). In summary, the following steps are required:

- preprocessing raw data: checking raw data for inconsistencies and SAR focusing;
- co-registration of the two SLC images (aligning on a sub-pixel level) and resampling;
- interferogram generation by complex multiplication (Figure 3.4a);
- subtraction of reference phase due to the reference ellipsoid (‘flattening’, Figure 3.4b).

Apart from these required steps, filtering the SAR data prior to interferogram computation as well as after the interferogram computation can enhance the signal-to-noise ratio (SNR) of the interferogram. Depending on the application at hand, one or more of the following steps may be required as well:

- subtraction of a reference Digital Elevation Model (DEM) to remove topography from the interferogram (known as differential-InSAR, Figure 3.4c);
- phase unwrapping;
- conversion of the unwrapped phase information to LOS deformation (or topographic height in case of topographic mapping);
- geocoding: conversion of the local radar coordinates to real-world coordinates.

The DEM required to remove topography can be either an external DEM, e.g. from the Shuttle Radar Topography Mission (SRTM), or a DEM interferogram computed from two SAR images of which it is known that no or negligible deformation took place in the time between the two acquisitions (usually a very short temporal baseline is used for this purpose). For earthquake deformation mapping, one of the images required for the DEM interferogram can also be used for the coseismic interferogram, but this is not necessarily the case. This technique is referred to as *three-pass interferometry* if both interferograms share one image and *four-pass interferometry* if the images of the DEM interferogram are not used for the coseismic interferogram. Differential-InSAR with an external DEM is known as *two-pass interferometry*.

For further analysis and to reduce noise it is often convenient to multi-look the original interferogram in such a way that the pixels of the resulting interferogram are approximately square. For ERS-2, with pixels of about  $4 \times 20$  m, this results in a multi-look factor of  $5 \times 1$ , i.e. 5 pixels of 4 m are averaged to 1 pixel of about 20 m.

Initially the phase information in an interferogram is wrapped in cycles of  $2\pi$  rad. For visualization purposes this is suitable, however for most applications unwrapped phase information is needed. Different methods to perform *phase unwrapping* are described in Bamler and Hartl (1998). After phase unwrapping, the LOS deformation  $d$  can be calculated using:

$$d = \Psi \frac{\lambda_R}{4\pi}, \quad (3.4)$$

where  $\Psi$  is the unwrapped interferometric phase and  $\lambda_R$  is the wavelength of the radar. It is important to note that all observations are relative, i.e. it is not known which point corresponds to zero deformation.

Finally, *geocoding* converts the local radar coordinates to a real-world coordinate system. This is particularly useful when combining other sources of data, for interpretation, and for visualization purposes.

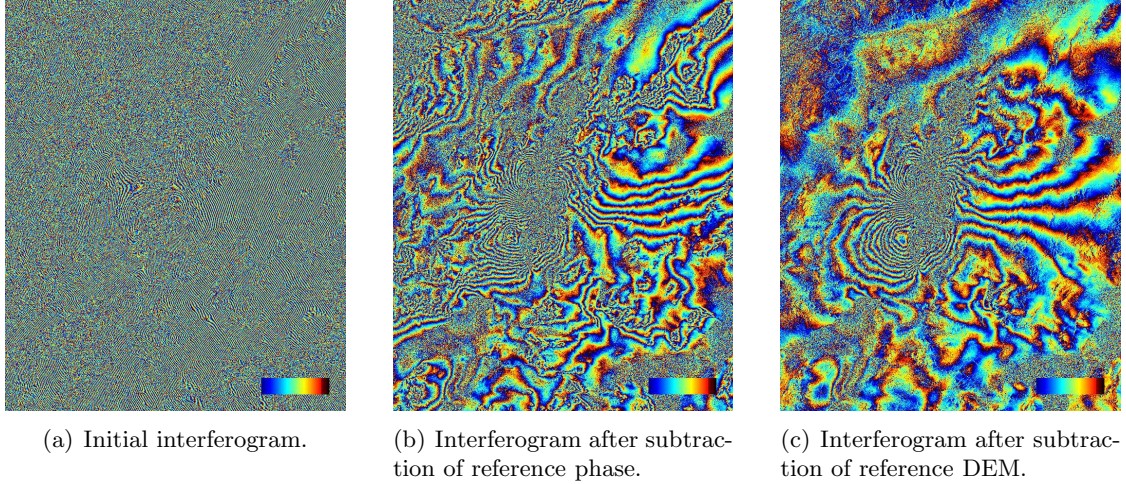


Figure 3.4: Interferogram of the 1999 Hector Mine earthquake: initial interferogram and interferogram after subtraction of reference phase and reference DEM. The radar images were acquired at November 12, 1995 (master, orbit 2937), and November 21, 1999 (slave, orbit 23979). The full interferogram covers an area of approximately  $97 \times 118$  km. One fringe corresponds to one phase cycle ( $2\pi$  rad).

### 3.2.3 Interferogram interpretation

Figure 3.5 is an enlarged and filtered version of the interferogram shown in Figure 3.4c. This interferogram is computed from two ERS-2 images from ascending satellite orbits (i.e. the satellite moved roughly from South to North during image acquisition, as opposed to descending orbits, where the satellite moves roughly from North to South). The ERS-2 satellite operates at a frequency of 5.3 GHz, which corresponds to a wavelength of 5.66 cm. Therefore, each color cycle or *fringe* represents 2.83 cm deformation in satellite LOS.

The color bar in the bottom-right of the image shows a color cycle from blue via turquoise, yellow, and red to dark-red, and then back to blue. This corresponds to an increase in range towards the satellite if the acquisition time of the master image is earlier than the acquisition time of the slave image and vice versa. The interferogram shows relative deformation only: the location that corresponds to zero deformation is unknown.

Note that the deformation is observed in satellite Line-Of-Sight (LOS) only, which is a projection of the horizontal and vertical deformation component. In this example interferogram a butterfly-like pattern is visible, which is typical for transform faults when the horizontal component of the satellite LOS is more perpendicular to the strike of the fault plane than parallel. When the horizontal component of the satellite LOS is approximately parallel to the fault plane, a butterfly pattern will not be observed. Knowing the satellite LOS is therefore important when interpreting coseismic interferograms.

In case of a rupturing fault the area near the rupture commonly lacks coherence. The extent of this area depends on the setting and the amount of damage caused by the earthquake. In particular inhabited regions near a fault trace tend to become decorrelated in a coseismic interferogram.



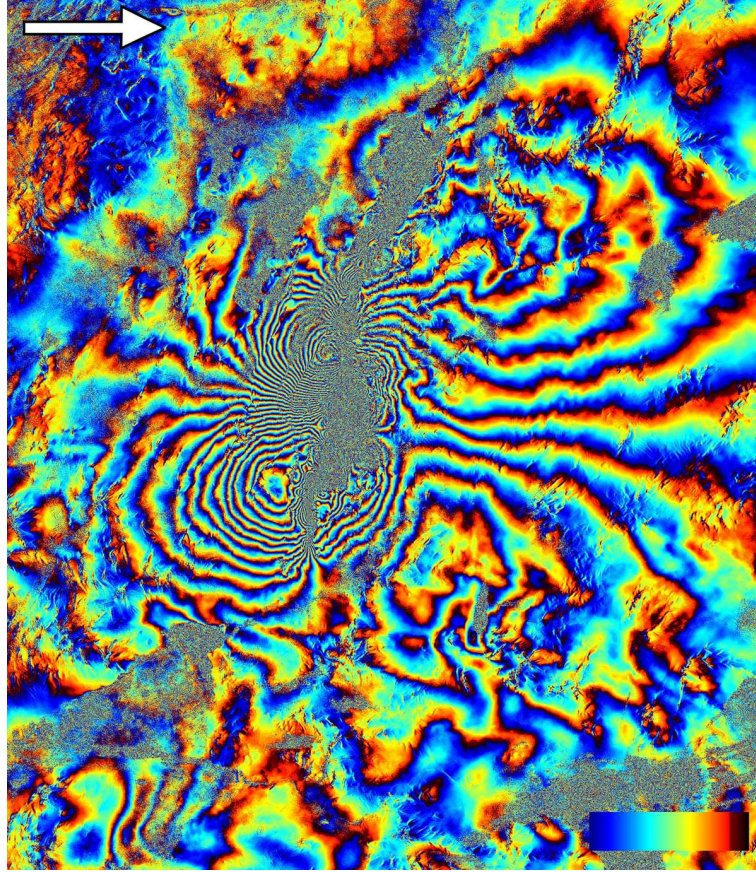


Figure 3.5: Interferogram of the 1999 Hector Mine earthquake (filtered version of the interferogram shown in Figure 3.4c). One fringe corresponds to 2.83 cm deformation in satellite Line-Of-Sight (LOS). The white arrow indicates the satellite viewing direction.

### 3.2.4 Error sources

Two important sources of errors in InSAR data are errors due to spatial and temporal variations in atmospheric delay and errors that are introduced by interferometric processing.

#### Errors due to variations in atmospheric delay

Temporal and spatial variations in refractivity of the atmosphere cause variability in atmospheric delay. Two processes can be distinguished that cause different types of delay (Hanssen, 2001):

- Turbulent mixing: causes heterogeneity in the refractivity and affects both flat areas and areas with topography.
- Vertical stratification variability: causes changes in refractivity profile. This source of atmospheric delay is topography-dependent and does not affect flat areas.

The total atmospheric delay can be divided in a *dry delay* term and a *wet delay* term. The dry delay term depends on the pressure and temperature of the atmosphere and may be visible as a trend in the interferogram. The wet delay mainly depends on the distribution

of water vapor, because variations in water vapor in the lower troposphere are the main cause of the variations in refractivity. The wet term accounts for vertical delay variability of several centimeters (Hanssen, 2001). Examples of atmospheric delay variations can be found in Massonnet and Feigl (1998) and Hanssen (2001).

It is not yet possible to measure the atmospheric delay with sufficient accuracy and resolution to correct interferograms for it. However, it is possible to describe the behavior of atmospheric signals in interferograms by using a stochastic atmospheric delay model. The model presented by Hanssen (2001) uses a power-law with three scaling regimes. This atmospheric delay model is used to create the synthetic atmospheric interferograms and will be discussed further in Section 5.6.

### **Errors introduced by interferometric processing**

There are several sources of errors that can be introduced during interferometric processing. This list includes, but is not necessarily limited to:

- Errors (commonly visible as trends) due to the use of incorrect satellite orbit parameters. The interferogram can be ‘detrended’ to correct for these errors.
- Decorrelation due to errors in co-registration and resampling. Those can be reduced by using well-designed filtering procedures (Hanssen, 2001).
- Errors in reference DEM, but the effect of those errors decreases with increasing height ambiguity.
- Errors in phase unwrapping. Especially when there are relatively large areas that are decorrelated, errors during unwrapping occur easily. A possibility is to unwrap the ‘islands’ of coherent areas in the interferogram separately. It is also possible to digitize fringes manually, see for example Wright et al. (1999).

## **3.3 Single-point surface deformation measurements: GPS and leveling**

Observations obtained with the Global Positioning System (GPS) and leveling are single-point geodetic observations. This is clearly a disadvantage when used for the observation of earthquakes, since a significant number of observations are required to be able to estimate the slip distribution. This makes both GPS and leveling labor-intensive and hence expensive techniques. They can, however, be used as additional observations to validate the estimation results, or to introduce more redundancy in the model. Furthermore, with these types of geodetic measurement techniques it is possible to obtain three components of deformation. For instance, Pedersen et al. (2003) successfully applied a joint inversion of both InSAR and GPS observations to estimate the slip distribution of two June 2000 earthquakes in Iceland. Another example is the study of Simons et al. (2002), who performed a joint inversion of GPS and InSAR to the Hector Mine earthquake. A joint inversion of leveling and InSAR data has been applied by Motagh et al. (2006).

To keep the scope of this study focused, single-point surface deformation observations are not used for the slip distribution inversions. However, correct use of these type of measurement techniques can provide useful observations to improve earthquake modeling results. Readers interested in the use of GPS for geodetic measurements are referred to e.g. Seeber (2003). A description of leveling is given in Vanicek et al. (1980).



## Chapter 4

# Earthquake slip distribution inversions

An earthquake can be modeled by one or more rectangular fault planes in an elastic half-space (Okada, 1985). Simple models assume that the slip on such a fault plane is uniform. This implies that there is a sharp transition between areas with significant slip and areas with no slip at all. This is assumed to be physically not realistic (Pedersen et al., 2003). Therefore, the fault plane should be divided in smaller patches to allow ‘tapering’ of the slip to zero towards the edges of the fault plane. The combination of all patches results in a *slip distribution*, which can contribute to the understanding of fault dynamics (Hernandez et al., 1997).

This chapter explains the procedure of earthquake slip distribution inversions as applied in this study. An overview of the inversion procedure is given in Figure 4.1. Each step of the procedure is explained in more detail in the following sections.

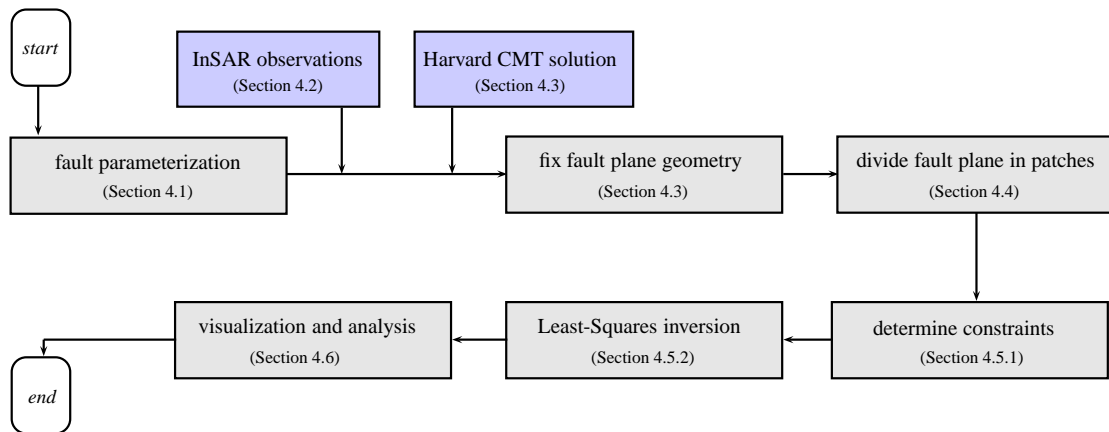


Figure 4.1: Overview of the inversion procedure. Each step is described in more detail in the corresponding section.

## 4.1 Fault parameterization and Okada model

The following set of source parameters is used to represent fault planes (Figure 4.2, see also Section 2.1):

$x$	x-coordinate of the top-center of the fault plane [km]
$y$	y-coordinate of the top-center of the fault plane [km]
$\alpha$	strike of the fault plane [ $^{\circ}$ ]
$\delta$	dip of the fault plane [ $^{\circ}$ ]
$d_{min}, d_{max}$	minimum and maximum depth of the fault plane [km]
$L$	length of the fault plane along strike [km]
$s$	slip (amount of displacement) [m]
$r$	rake (direction) of displacement [ $^{\circ}$ ]

An alternative way to parameterize the direction of displacement on a fault plane is to decompose the slip in the direction specified by the rake in a strike-slip and a dip-slip component. The strike-slip component is the slip in the direction parallel to the strike and the dip-slip component is slip in the direction parallel to the dip. However, previous studies (e.g. Ji et al. (2002), Wright et al. (2003)) show that in general the slip on the fault plane is predominantly in one direction. Therefore, the parameterization with only one direction of slip specified by the rake is used for simplicity.

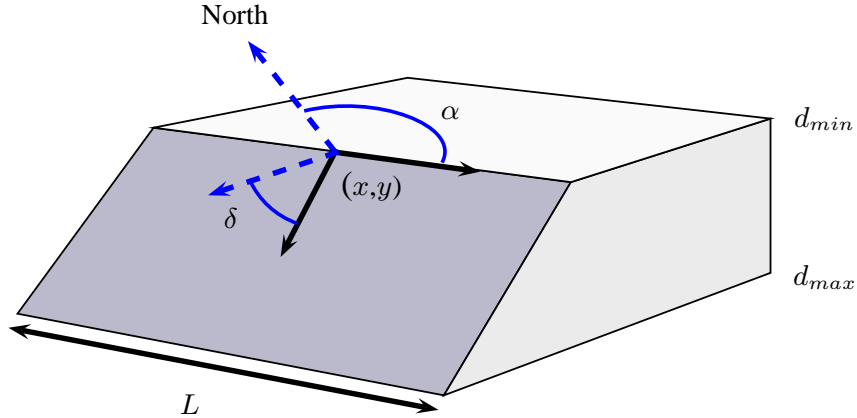


Figure 4.2: Fault parameterization. Not shown are the amount of slip and the rake, which is the angle between the slip direction vector and the strike (see also Figure 2.2).

Okada (1985) presented analytical expressions to calculate surface displacements based on the source parameters of an earthquake. These expressions are based on the assumption of a homogeneous elastic half-space, with the Earth's surface taken as the boundary of the half-space. The rheological properties of this half-space are determined by Lamé constants  $\mu_L$  and  $\lambda_L$ . It is commonly assumed that  $\mu_L$  and  $\lambda_L$  are equal, implying a Poisson's ratio  $\nu = 0.25$  (Massonnet and Feigl, 1998). DeformTool, an open-source implementation of Okada's expressions (van Zwieten, 2008) is used as a basis for the earthquake slip distribution inversions in this study.

## 4.2 InSAR observations

### 4.2.1 Image selection and processing

The selection of the SAR images should be based mainly on a trade-off between perpendicular baseline and temporal baseline. For two reasons the perpendicular baseline should be as small as possible:

1. to improve overall coherence of the interferogram; and
2. to reduce the sensitivity to topography (to limit the effect of DEM errors).

The temporal baseline should be such that at least the instance of the event is covered. For coseismic earthquake studies, the temporal baseline should be as short as possible, because:

- pre-seismic and / or post-seismic deformation can contribute to the observed deformation, which causes errors in the slip distribution estimation; and
- changes due to natural and / or anthropogenic processes can reduce the coherence of the interferogram.

However, the requirement of a short temporal baseline is sometimes not feasible, either because there are not enough images available (e.g. ERS-2 ascending images are generally acquired with a longer time interval than descending images), or because the available images cannot be processed to usable interferograms due to large perpendicular baselines. A baseline plot, i.e. a plot of the temporal baseline against the perpendicular baseline, can be convenient for a quick overview of the possible interferometric combinations of the available radar images (Hanssen, 2001).

Another issue to consider is the combination of ascending and descending image pairs. With only one image pair the deformation is observed in satellite LOS only, which is composed of deformation in the horizontal and the vertical directions. The combination of ascending and descending interferograms may make it possible to derive the three-dimensional displacement field of an earthquake (Fialko et al., 2001).

After image selection the data can be processed following the steps described in Section 3.2.2. All steps (except filtering, multi-looking, and geocoding) that have been discussed are mandatory for real-world case studies.

### 4.2.2 Data reduction

Due to the large amount of data, data reduction techniques need to be applied to reduce the computational time and memory requirements. Two well-known techniques are considered here: uniform resampling and quad-tree partitioning.

#### Uniform resampling

Uniform resampling is the most simple form of data reduction. In this algorithm, neighboring pixels are merged into one pixel, which receives the value of the average of the merged pixels. The number of pixels that is merged determines the amount of data reduction. The disadvantage of this technique is that the information loss can be significant, since no information about the variance of the pixels is included in the resampling process. For instance, resampling a  $3 \times 3$  pixel area that contains the values  $[4, 4, \dots, 4]$  to one

pixel will result in the value ‘4’ for the new pixel. However, resampling a pixel area of similar size that contains the values [4, 0, 1, 5, 12, 0, 13, 0, 1] will result in a new pixel with the value ‘4’ as well. This example illustrates that a trade-off is required between noise reduction, acceptable information loss, and the degree of data reduction.

### Variable resolution resampling and quad-tree partitioning

Variable resolution resampling is similar to uniform resampling, except that the number of pixels to be merged in the resampling process may differ. For instance, an interferogram contains more information near the fault trace of an earthquake, than some distance away from it. With variable resolution resampling, the number of pixels to be merged near the fault trace can be chosen to be much lower than away from the fault trace, resulting in less information loss than with uniform resampling.

*Quad-tree partitioning* (e.g. Welstead (1999)) is an example of variable resolution resampling. It has been widely used in different fields of research to reduce the amount of (spatially correlated) data significantly, while at the same time controlling the loss of information. A quad-tree algorithm divides an interferogram into four segments, and calculates the spread (variance) of LOS deformation or maximum difference in LOS deformation of each segment. If this spread or difference exceeds a certain threshold, then this particular segment is again divided into four segments. This process is repeated until all segments have a spread or difference less than the defined threshold. The higher the threshold, the lower the detail that is present in the quad-tree generalization of the original interferogram. An optimal threshold combines the advantage of data reduction while preserving the important details of the interferogram. The relations between the different segments of a quad-tree partitioned data set are stored in a tree, hence the name ‘quad-tree’.

#### 4.2.3 Weighting the observations

There are several possibilities to weight the InSAR observations. First of all, when applying quad-tree partitioning as a data reduction technique, the observations should be weighted according to their corresponding pixel size. For example, quad-tree segments that are composed of 16 original pixels (a  $4 \times 4$  segment) should be weighted a fourth of quad-tree segments that contain 64 original pixels (an  $8 \times 8$  segment). Weighting the observations based on their pixel size is also mandatory when comparing cases with different degrees of data reduction. It is therefore advised to apply this weighting method, regardless of the data reduction method.

Observations can be weighted based on their coherence as well. Coherence can be used to calculate first-order approximations of the variance of the observations (Bamler and Hartl, 1998). An advantage of weighting the observations based on their variance is that estimations of the variance and covariance of the estimated slip distribution can be obtained. A derivation of the variance based on coherence is given in Hanssen (2001).

If applicable, it is also possible to assign different weights to different data sets (e.g. ascending and descending interferograms). For example, Jónsson (2002) assigned different weights to GPS observations, an ascending interferogram, and a descending interferogram based on their estimated uncertainty and the number of observations.

### 4.3 Determination of the fault plane geometry

Several data sources can be used to fix the geometry of a fault plane, two of which are used in this study: seismic information and the InSAR data itself.

Seismic information can be obtained from the Harvard CMT catalog, which is freely available on the internet ([www.globalcmt.org](http://www.globalcmt.org)). The online database includes earthquakes with a magnitude of 5.5 and larger since January 1976. The information provided includes, but is not limited to:

- date, time, and location of the earthquake;
- orientation of the fault plane and auxiliary plane;
- depth of the earthquake focus;
- rake of the slip;
- seismic moment and moment magnitude;
- fault-plane solution (graphical representation of the type of earthquake).

In combination with the interpretation of one or more interferograms this information is sufficient to determine most of the fault plane geometry parameters. Visual interpretation of the interferogram provides information about the approximate location, strike, and length of the fault plane, since the fault trace can often be identified in coherent interferograms by an increase in the number of fringes per area from both sides of the fault. The location and strike can also be compared with the CMT solution as an additional check and to distinguish between the fault plane and the auxiliary plane given by the CMT solution.

Table 4.1 gives the information sources for each fault plane parameter. A problem arises for the  $d_{min}$  and  $d_{max}$  parameters, since the CMT solution only provides the focal depth, and not the depth extent of the fault plane. From the interferogram it can often be deduced whether the fault plane extends to the surface (a rupturing fault) or not (a blind fault), but it is not possible to determine the minimum and maximum depth of the fault plane. As will be shown in Chapter 5, an increase in fault plane depth does not influence the estimation result significantly, as long as the depth extent of the fault plane is chosen such that the slip reaches zero at the boundaries of the fault plane (except for

Table 4.1: Information sources for each fault plane parameter.

Parameter	Determined from
$x$	interferogram or CMT solution
$y$	interferogram or CMT solution
$\alpha$	interferogram or CMT solution
$\delta$	CMT solution
$d_{min}, d_{max}$	trial-and-error procedure
$L$	interferogram
$r$	CMT solution

the surface in case of a rupturing fault). Therefore, the determination of the depth extent can be done by a simple trial-and-error procedure.

Other possible information sources that can be used to determine the fault plane geometry include field measurements (mapped fault traces), single-point geodetic measurements and observations of aftershock activity.

## 4.4 Division of the fault plane in patches

After the geometry of the fault plane has been determined, the fault plane is divided into patches. The number of patches in strike and dip direction determines the level of detail of the final slip distribution. The chosen level of detail can depend on the scale of the earthquake, e.g. earthquakes with a fault length of 500 km can be modeled with a larger patch size than earthquakes that have a fault length of 25 km. In this study the synthetic slip distribution (see Chapter 5) has a patch size of  $1 \times 1$  km and the slip distribution estimated for the 1999 Hector Mine earthquake has a patch size of  $2 \times 2$  km (Chapter 6). With these patch sizes the computational time is limited, while at the same time a reasonable level of detail of the slip distribution is achieved.

## 4.5 Earthquake slip distribution estimation

The forward model to calculate LOS surface deformation based on a slip distribution can be written as the following system of equations:

$$d_p = \mathbf{A}s, \quad (4.1)$$

where  $d_p$  is the predicted LOS surface deformation,  $s$  is the set of slip values for all patches (the slip distribution), and  $\mathbf{A}$  is the design matrix that links the slip distribution to surface displacements. This model is used in Chapter 5 for the calculation of synthetic LOS surface deformation.

Due to model imperfections and errors in real observations, the observed surface deformation will not equal the predicted deformation (Tarantola, 2005). Therefore, the inverse model:

$$d = \mathbf{A}s + e, \quad (4.2)$$

includes an error vector  $e$ , which contains the errors in the observations. The observed surface deformation is denoted by  $d$ . This system is commonly referred to as the *system of observation equations*. The linear inverse problem is to estimate  $s$  based on the observations  $d$ . Assuming that the errors are unbiased, i.e.  $E\{e\} = 0$ , the model of observation equations can be written as  $E\{d\} = \mathbf{A}s$ , where  $E\{\}$  is the expectation operator.

The design matrix  $\mathbf{A}$  is constructed as follows. A unit amount of slip (e.g. 1 m) on one patch contributes to the LOS deformation in all  $m$  observation points. The deformation of each observation point can therefore be written as a linear combination of the deformation contributions of all patches to that observation point. For example, the first row in  $\mathbf{A}$  can be written as  $[a_{11} \ a_{12} \ \dots \ a_{1n}]$ , with  $a_{11}$ ,  $a_{12}$ , and  $a_{1n}$  the contributions to observation  $d_1$  of a unit amount of slip on patch 1, 2, to  $n$ , respectively. These contributions  $a_{mn}$  are computed by Okada's forward model. The deformation in observation  $m$  can thus be written as:

$$d_m = s_1 a_{m1} + s_2 a_{m2} + \dots + s_n a_{mn}. \quad (4.3)$$

The model of observation equations, Equation (4.2), does not yet include the estimation of additional unknown parameters. More specific, the design matrix  $\mathbf{A}$  should be extended to account for the offset in deformation that is present in the interferogram. This can be explained as follows. The phase unwrapping algorithm that attempts to reconstruct the unwrapped phase from the wrapped phase starts at a certain pixel in the interferogram (e.g. in the top-left corner of the interferogram) and sets that point to zero deformation. This results in an offset of absolute phase and thus of the absolute deformation, since the chosen zero-deformation point may not be a point of zero deformation in reality. This offset will be referred to as the *zero-deformation offset*. The offset is estimated by adding a column  $[1, 1, \dots, 1]^T$  to  $\mathbf{A}$ . Other parameters that can be estimated are for example parameters to correct for possible trends in the interferogram, but this is not applied in this study.

#### 4.5.1 Additional constraints

In general, geophysical inverse problems such as slip distribution estimations are ill-posed (Du et al., 1992).

- The solution is non-unique: there are many slip distributions that give the same surface deformation field.
- The solution is instable: a slightly different set of observations can result in a completely different slip distribution.

Mathematically, this problem is expressed in the fact that the normal matrix  $\mathbf{A}^T \mathbf{A}$  is singular, i.e. its inverse does not exist. The addition of constraints is therefore an important step in the inversion procedure, since it reduces the number of possible solutions and stabilizes the solution.

The most important constraint used in this study is that the solution should be smooth to a certain degree. It is thereby assumed that it is physically not realistic to have sharp transitions in slip between neighboring patches (Pedersen et al., 2003). A common method to implement smoothness is to introduce a set of equations which minimizes the discrete second-order spatial derivative  $\nabla$  (discrete Laplacian) of the slip distribution. The added set of equations is referred to as a set of *pseudo observations*. The system of equations then becomes:

$$E\left\{\begin{pmatrix} d \\ 0 \end{pmatrix}\right\} = \begin{pmatrix} \mathbf{A} \\ \nabla \end{pmatrix} s. \quad (4.4)$$

The degree of smoothness is determined by the variance that is assigned to the pseudo observations. This variance is contained in the stochastic model, which is written as:

$$D\left\{\begin{pmatrix} d \\ 0 \end{pmatrix}\right\} = \begin{pmatrix} Q_{dd} & 0 \\ 0 & Q_{\nabla\nabla} \end{pmatrix}, \quad (4.5)$$

where  $Q_{dd}$  and  $Q_{\nabla\nabla}$  are the variance-covariance matrices of the observations and pseudo observations, respectively. The degree of smoothness can be implemented as a smoothness weight, which is considered more intuitive to use compared to  $Q_{\nabla\nabla}$ . The relation between the smoothness weight  $f_w$  and the variance of the smoothness operator  $\sigma_{\nabla\nabla}^2$  is defined as:

$$\sigma_{\nabla\nabla}^2 = \frac{p_\alpha \cdot p_\delta}{f_w^2}, \quad (4.6)$$

where  $p_\alpha$  and  $p_\delta$  are the patch sizes in strike direction and dip direction, respectively. Note that for one value for  $f_w$  the variance  $\sigma_{\nabla\nabla}^2$  can differ due to different patch sizes.

With a uniform variance for all pseudo observations and assuming all covariances zero, the variance-covariance matrix  $Q_{\nabla\nabla}$  is given as:

$$Q_{\nabla\nabla} = \sigma_{\nabla\nabla}^2 \mathbf{I}_n, \quad (4.7)$$

with  $\mathbf{I}_n$  an  $n \times n$  identity matrix, where  $n$  corresponds to the number of patches. The relation between  $Q_{\nabla\nabla}$  and  $f_w$  is chosen such that a lower smoothness weight results in a larger variance. This reduces the weight of the smoothness operator in the estimation of the slip distribution. The smoothness operator  $\nabla$  for one patch  $p_{k,l}$  of the fault plane is the following second-order differentiation kernel (Jónsson, 2002):

$$\nabla(p_{k,l}) = \frac{1}{p_\alpha^2}(s_{k-1,l} - 2s_{k,l} + s_{k+1,l}) + \frac{1}{p_\delta^2}(s_{k,l-1} - 2s_{k,l} + s_{k,l+1}), \quad (4.8)$$

where the indices  $k$  and  $l$  are patch numbers in respectively the strike and dip direction (Figure 4.3). This expression holds for patches that are not located on the boundary of the fault plane. For patches on e.g. the lower boundary of a fault plane it is assumed that deeper patches have zero slip. For these boundary patches, the smoothness operator becomes:

$$\nabla(p_{k,l}) = \frac{1}{p_\alpha^2}(s_{k-1,l} - 2s_{k,l} + s_{k+1,l}) + \frac{1}{p_\delta^2}(s_{k,l-1} - 2s_{k,l}). \quad (4.9)$$

Similar expressions can be derived for patches on the left and right boundary and, in case of a blind fault, also the upper boundary. For those patches that intersect with the surface, the second order derivative in dip direction is reduced to:

$$\nabla(p_{k,l}) = \frac{1}{p_\alpha^2}(s_{k-1,l} - 2s_{k,l} + s_{k+1,l}) + \frac{1}{p_\delta^2}(-1s_{k,l} + s_{k,l+1}), \quad (4.10)$$

due to the discontinuity of slip at the Earth's surface. The structure of  $\nabla$  depends on the numbering of the patches.

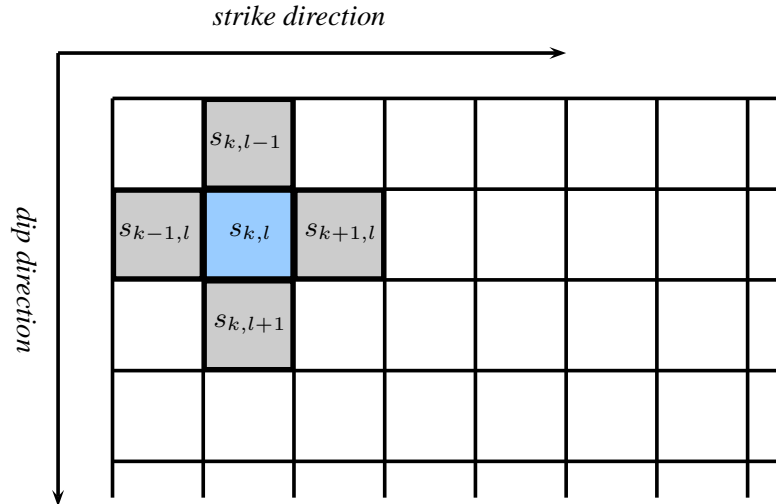


Figure 4.3: Patches of a fault plane.  $s_{k,l}$  is the slip on the  $k$ -th patch in strike direction and  $l$ -th patch in dip direction. The smoothness constraint implies that the discrete second-order difference in strike and dip direction should be small (depending on the chosen variance  $\sigma_{\nabla\nabla}^2$ ). Large transitions in slip between neighboring patches are therefore avoided.



Another constraint that can be implemented is a non-negativity constraint. This constraint solves the system of equations such that the estimated parameters can only be positive. This constraint makes the system of equations to solve non-linear and therefore increases the computational time significantly.

#### 4.5.2 Inversion: Least-Squares Estimation (LSE)

The general weighted Least-Squares Estimation (LSE) of the system of observation equations, Equation (4.2), is given by:

$$\hat{s} = (\mathbf{A}^T Q_{dd}^{-1} \mathbf{A})^{-1} \mathbf{A}^T Q_{dd}^{-1} d, \quad (4.11)$$

where  $\hat{s}$  is the estimate of the slip distribution. The LSE of the more complex system of observation equations, Equation (4.4), is derived as:

$$\hat{s} = \left[ \begin{pmatrix} \mathbf{A} \\ \nabla \end{pmatrix}^T \begin{pmatrix} Q_{dd} & 0 \\ 0 & Q_{\nabla\nabla} \end{pmatrix}^{-1} \begin{pmatrix} \mathbf{A} \\ \nabla \end{pmatrix} \right]^{-1} \begin{pmatrix} \mathbf{A} \\ \nabla \end{pmatrix}^T \begin{pmatrix} Q_{dd} & 0 \\ 0 & Q_{\nabla\nabla} \end{pmatrix}^{-1} \begin{pmatrix} d \\ 0 \end{pmatrix} \quad (4.12)$$

$$= [\mathbf{A}^T Q_{dd}^{-1} \mathbf{A} + \nabla^T Q_{\nabla\nabla}^{-1} \nabla]^{-1} \mathbf{A}^T Q_{dd}^{-1} d. \quad (4.13)$$

If the observations are not weighted, the variance-covariance matrix  $Q_{dd}$  can be considered as an identity matrix  $\mathbf{I}_m$ , with  $m$  the number of observations. The coupled normal matrix  $\mathbf{A}^T Q_{dd}^{-1} \mathbf{A} + \nabla^T Q_{\nabla\nabla}^{-1} \nabla$  is not singular unless  $Q_{\nabla\nabla}^{-1}$  approaches zero.

The total size of the system of equations is  $j \times q$ , with  $j = m + n$  the sum of the number of observations and pseudo observations and  $q$  the number of parameters to be estimated, consisting of the slip distribution, the zero-deformation offset, and, if estimated, the corrections for trends in the interferogram.

One problem with the LSE approach is that slip can become negative on certain patches, implying that there is slip in opposite direction of the rake. To solve this problem a non-negativity constraint can be implemented by using Non-Negative Least-Squares (NNLS, see Lawson and Hanson (1974)). However, three problems are associated with the use of NNLS:

- Some parameters are allowed to be negative, such as the zero-deformation offset.
- NNLS is a non-linear estimation procedure which is rather computationally expensive compared to conventional LSE.
- Due to its non-linear nature, NNLS complicates the quality control of the estimated slip distribution.

The first problem can be solved and the computational time can be reduced by estimating the slip distribution in three steps:

1. Estimate the initial slip distribution and additional parameters with conventional LSE.
2. Correct the observations for the zero-deformation offset and, if necessary, for trends estimated in step 1.
3. Perform a NNLS estimation based on the initial estimate for the slip distribution of step 1 with the corrected observations of step 2.

Whether or not such a three-step procedure is required depends on the available time and the significance of negative slip that is estimated. For the 1999 Hector Mine earthquake, this significance is investigated in Chapter 6.

## 4.6 Slip distribution visualization and further analysis

The estimated slip distribution is the vector  $\hat{s}$  (possibly with additionally estimated parameters) that can be visualized in several ways, depending on the application and personal preference. For this study the slip distribution is visualized three-dimensionally, with a transparent gray plane representing the Earth's surface.

The Root-Mean-Squared Error (RMSE) of the misfit between the modeled surface deformation and the interferogram can be calculated to investigate the degree of correspondence between the model and the observations. The RMSE of the misfit  $\varepsilon_m$  is defined as:

$$\varepsilon_m = \sqrt{\sum_{k=1}^m \frac{e_k^2}{m}}, \quad (4.14)$$

with  $m$  the number of observations and  $e_k$  the misfit (residue) of observation  $k$ . For synthetic data studies (Chapter 5), the Root-Mean-Squared Error (RMSE) of the slip distribution can be computed as well. The RMSE of the slip distribution  $\varepsilon_{sd}$  is defined as:

$$\varepsilon_{sd} = \sqrt{\sum_{i=1}^n \frac{\Delta s_i^2}{n}}, \quad (4.15)$$

where  $n$  is the number of patches and  $\Delta s_i$  is the error in slip on patch  $i$ .

When the variance-covariance matrix  $Q_{dd}$  is known, the variance-covariance matrix of the slip distribution  $Q_{\hat{s}\hat{s}}$  can be calculated by using:

$$Q_{\hat{s}\hat{s}} = [\mathbf{A}^T Q_{dd}^{-1} \mathbf{A} + \nabla^T Q_{\nabla\nabla}^{-1} \nabla]^{-1}. \quad (4.16)$$

Further analysis can include, but is not limited to:

- a calculation of the seismic moment  $M_0$  and the moment magnitude  $M_W$  and comparison of these values with seismic data;
- a general test on discrepancies between the observations and assumed model (e.g. applying an Overall Model test);
- a comparison of cross-sections through the model and through the observations (see for example Salichon et al. (2004)).

## Chapter 5

# Influence of errors in fault plane geometry and atmospheric delay variations in observations

As outlined in the introduction, fixing the fault plane geometry of an earthquake in the inversion of the slip distribution has the advantage that the inverse problem becomes linear. This makes it both more easy to implement and less computationally expensive. However, if the fault plane geometry is not estimated in the inversion, it should be fixed on the basis of prior information about the fault plane geometry. This information comes from both seismic data and InSAR data, as discussed in Section 4.3. However, errors in the fault plane geometry will have a certain influence on the estimated slip distribution. In this chapter, synthetic interferograms representing three main earthquake types are used to investigate this influence (research objective 1).

Due to the linearity of the inverse problem, it is possible to investigate the influence of atmospheric delay variations in the observations on the estimated slip distribution as well (research objective 2). Atmospheric signals are simulated with the atmospheric model proposed by Hanssen (2001). These are used as observations to estimate the slip distribution, which reflects a typical error that can be expected due to atmospheric delay variability in observations.

In Section 5.1, a description is given of the synthetic InSAR data sets that are used. After that, the effect of different smoothness weights is examined in Section 5.2. The influence of errors in fault plane orientation, position, and dimensions is then discussed in Section 5.3, Section 5.4, and Section 5.5, respectively. The influence of atmospheric delay variations in the observations is discussed in Section 5.6. Finally, concluding remarks are presented in Section 5.7. A selection of plots of the estimated slip distribution and modeled surface deformation can be found in Appendix A.

### 5.1 Synthetic InSAR data

Six synthetic InSAR interferograms are created that represent three different earthquake types, viewed from two different satellite LOS. The three earthquake types, a transform fault (TF), a normal fault (NF), and a reverse fault (RF), differ in their fault plane geometry only in dip and rake. The fault plane geometry parameters are given in Table 5.1. A slip distribution with  $M_W = 6.9$  is defined for a rupturing fault plane of 30 km in length and 15 km in depth (Figure 5.1). The patches on this fault plane are  $1 \times 1$  km in size.

The interferograms are created with Okada's forward model, which is used to calculate displacements in x-, y-, and z-direction caused by the slip distribution on the proposed fault planes. These three-dimensional displacements are then projected onto two different LOS-vectors. The LOS-vectors differ only in azimuth angle  $\theta_{az}$ , which is the angle between the satellite orbit and a reference (usually the North). For both LOS-vectors, the incidence angle  $\theta_i$  equals the average incidence angle of the ERS-2 satellite ( $\theta_i = 23^\circ$ ). The LOS-vector is given by  $(-\cos \theta_{az} \sin \theta_i, \sin \theta_{az} \sin \theta_i, \cos \theta_i)$ , corresponding to the East, North, and Up components (Arikan and Hanssen, 2008). The synthetic interferograms for the transform fault, normal fault, and reverse fault are presented in Figure 5.2. For the purpose of visualization the surface deformation in satellite LOS is wrapped to cycles of 5 cm deformation.

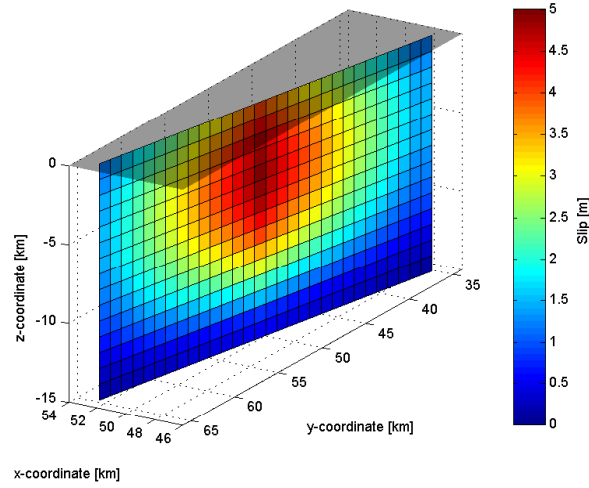
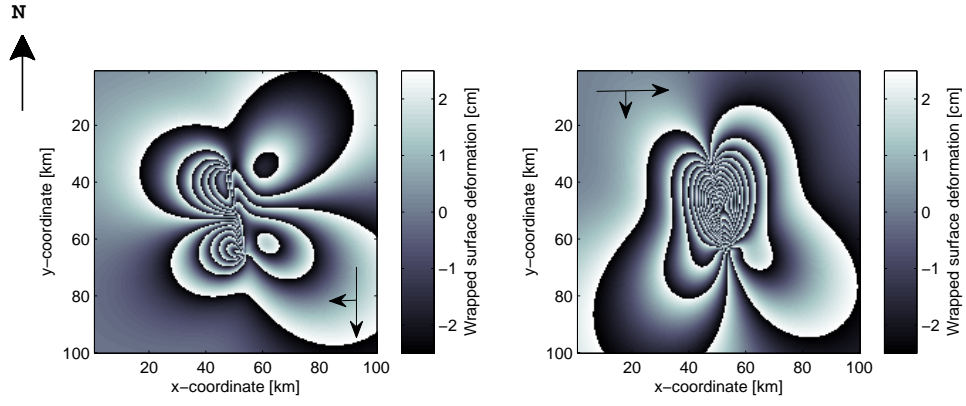


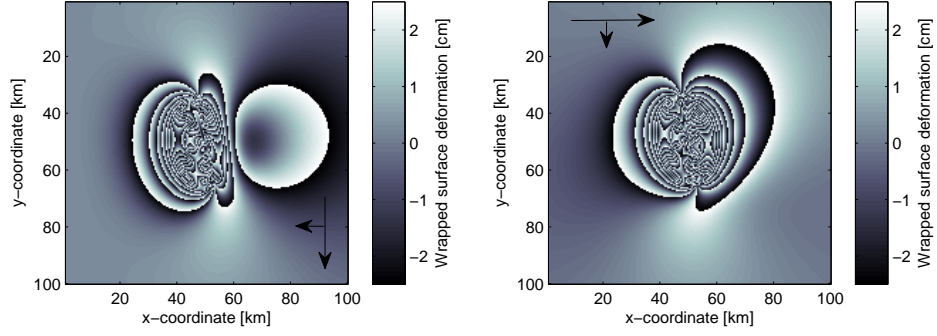
Figure 5.1: Slip distribution with  $M_W = 6.9$ , which is used to create the synthetic interferograms. Here, the slip distribution is shown on the fault plane geometry of the transform fault.

Table 5.1: Fault plane geometries of the three different earthquakes: transform fault (TF), normal fault (NF), and reverse fault (RF). The strike is specified w.r.t. the North. ★ The depth extent is specified as  $(d_{min}, d_{max})$ .

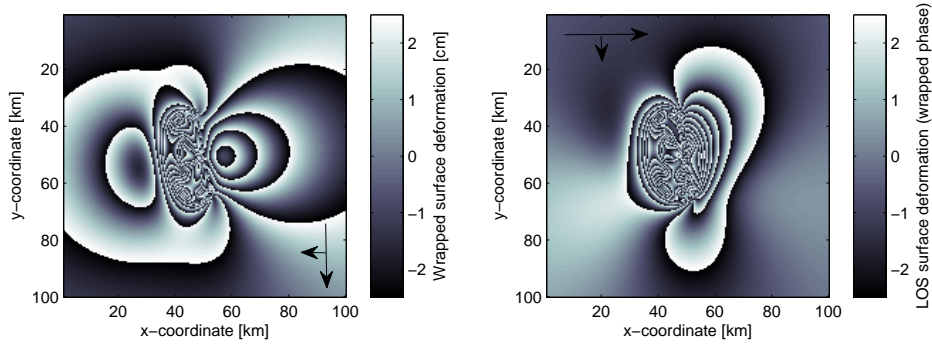
Type	Strike	Dip	Rake	Length	Depth extent★
TF	$170^\circ$	$90^\circ$	$0^\circ$	30 km	(0,15) km
NF	$170^\circ$	$75^\circ$	$-90^\circ$	30 km	(0,15) km
RF	$170^\circ$	$50^\circ$	$90^\circ$	30 km	(0,15) km



(a) Synthetic interferograms of the transform fault.



(b) Synthetic interferograms of the normal fault.



(c) Synthetic interferograms of the reverse fault.

Figure 5.2: Synthetic interferograms for two different LOS-vectors and the three earthquake types. The arrows indicate the satellite viewing geometry. The interferograms are shown in a local ground coordinate system and all are oriented to the North.

## 5.2 Smoothness constraint

As discussed in Section 4.5.1, constraints need to be added to the inverse model in order to obtain a unique solution. The smoothness operator  $\nabla$  is implemented as a set of pseudo observations which is added to the model of observation equations. The relative weight of the smoothness operator in the inversion is determined by the variance of the smoothness operator, which is contained in  $Q_{\nabla\nabla}$ . The variance is specified by a smoothness weight  $f_w$ . A larger weight  $f_w$  corresponds to a smaller variance, hence more weight is assigned to the pseudo observations in the inversion.

An important question that immediately arises is: how to choose the correct degree of smoothness? To investigate this question, the performance of the smoothness operator  $\nabla$  is tested using the synthetic interferogram representing the transform fault at  $\theta_{az} = 180^\circ$  (left interferogram in Figure 5.2a). For different scenarios, the RMSE of the slip distribution  $\varepsilon_{sd}$  and the RMSE of the misfit  $\varepsilon_m$  between the estimated model and the synthetic interferogram are computed as a function of the smoothness weight  $f_w$ . The scenarios that are used to test the performance of  $\nabla$  differ in fault plane geometry:

**Scenario 1** - all fault plane geometry parameters are correct (they are consistent with the parameters that were used to create the synthetic interferogram).

**Scenario 2** - the fault plane geometry has an error in strike of  $\Delta\alpha = 0.5^\circ$ .

**Scenario 3** - the fault plane geometry has an error in strike of  $\Delta\alpha = 5.0^\circ$ .

**Scenario 4** - the fault plane geometry has errors in strike:  $\Delta\alpha = 3.0^\circ$ , dip:  $\Delta\delta = 3.0^\circ$ , and rake:  $\Delta r = 5.0^\circ$ .

The error values for these scenarios are arbitrarily chosen. However, they lie within the maximum error range for the strike, dip, and rake of about  $\pm 10^\circ$  that is expected in the CMT solution (Sigmundsson, 2008).

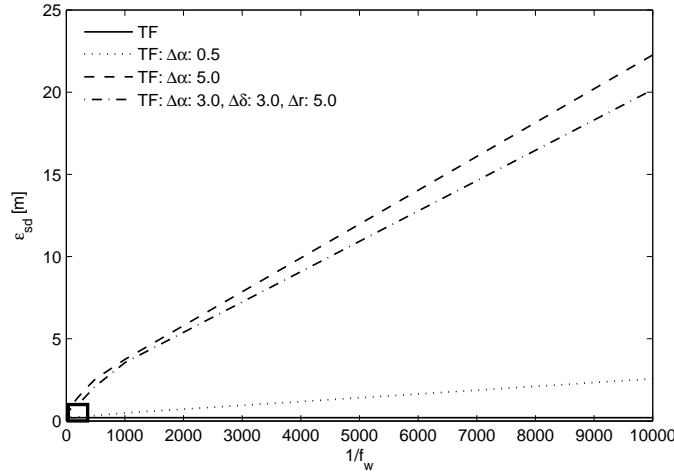


Figure 5.3: Effect of the smoothness weight  $f_w$  on the RMSE error  $\varepsilon_{sd}$  of the estimated slip distribution. Larger values for  $1/f_w$  correspond to lower smoothness weights, hence the roughness of the slip distribution increases. This results in a larger  $\varepsilon_{sd}$ . The minimum in  $\varepsilon_{sd}$  for these scenarios, which corresponds to the optimal choice for  $f_w$ , is located within the region bounded by the black rectangle. This region is shown enlarged in Figure 5.4.

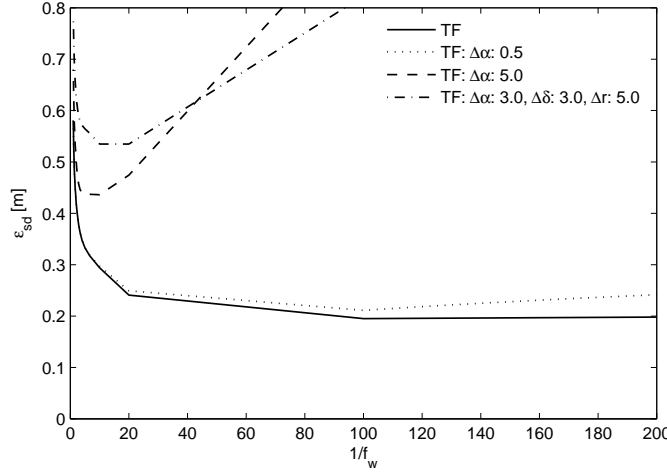


Figure 5.4: Enlargement of the region bounded by the black rectangle shown in Figure 5.3. The minimum in  $\varepsilon_{sd}$  corresponds to the optimal smoothness weight  $f_w$ , which is different for each scenario.

Figure 5.3 and Figure 5.4 show  $\varepsilon_{sd}$  as a function of  $1/f_w$ . It is observed that the minimum RMSE of the slip distribution corresponds to smoothness weights in the approximate interval  $2 < 1/f_w < 200$ , but this  $f_w$  is different for each scenario. Thus, the optimal value for  $f_w$  is case-dependent. Since the four scenarios examined here are sufficient to draw this conclusion, more test scenarios need not be considered.

For real-world cases the problem of finding the optimal smoothness weight is even more complicated, because  $\varepsilon_{sd}$  cannot be computed, since the true slip distribution is unknown. Figure 5.5 shows the RMSE of the misfit  $\varepsilon_m$  as a function of the smoothness weight  $f_w$ . For the correct fault plane geometry,  $\varepsilon_m$  approaches zero when  $f_w$  approaches zero. Clearly, there is no way of determining the optimal smoothness weight based on only the RMSE of the misfit. As was already concluded by Jónsson (2002) and Wright et al. (2003), amongst others, the degree of smoothness should thus be determined by a trade-off between the RMSE of the misfit  $\varepsilon_m$  and the roughness  $R_{sd}$  of the estimated slip distribution. The roughness of the slip distribution is defined as the mean absolute Laplacian of the estimated slip distribution at a certain smoothness weight:

$$R_{sd} = \frac{1}{n} \sum_{i=1}^n |\nabla(p_i)|, \quad (5.1)$$

where  $n$  is the number of patches and  $\nabla(p_i)$  is the discrete Laplacian of patch  $p_i$  (Equation (4.8)). The roughness parameter  $R_{sd}$  can be plotted as a function of the misfit  $\varepsilon_m$  or vice versa, see Figure 5.6. The arrows indicate the smoothness weight and roughness corresponding to the minimum RMSE of the slip distribution  $\varepsilon_{sd}$ .

The remaining analyses of this chapter are based on a uniform smoothness weight for simplicity. This weight is chosen to be  $f_w = 0.1$ , which lies in the interval  $2 < 1/f_w < 200$ . This smoothness weight corresponds to the optimal smoothness weight for scenario 3 and lies close to the optimal smoothness weight for scenario 4. The influence of errors in strike, dip, rake, position, and dimensions of the fault plane will be amplified for lower values of  $f_w$ , and damped for larger values of  $f_w$ . Note that the relative weight of the observations and smoothness operator in the inversion is not only determined by  $f_w$ , but also by the variance-covariance matrix of the observations, see Equation (4.12).

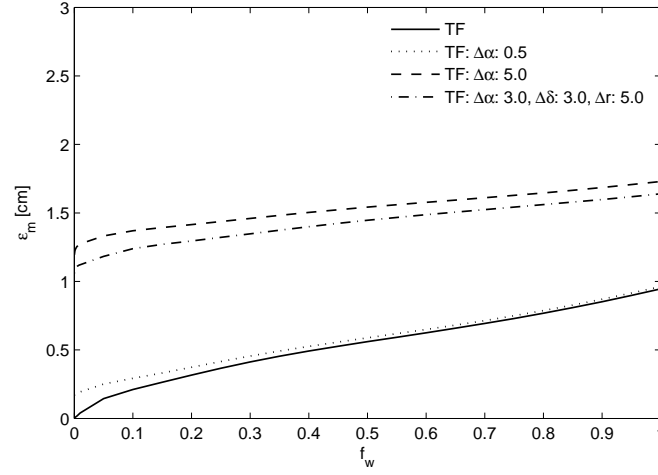


Figure 5.5: Effect of the smoothness weight  $f_w$  on the RMSE error  $\varepsilon_m$  of the misfit.

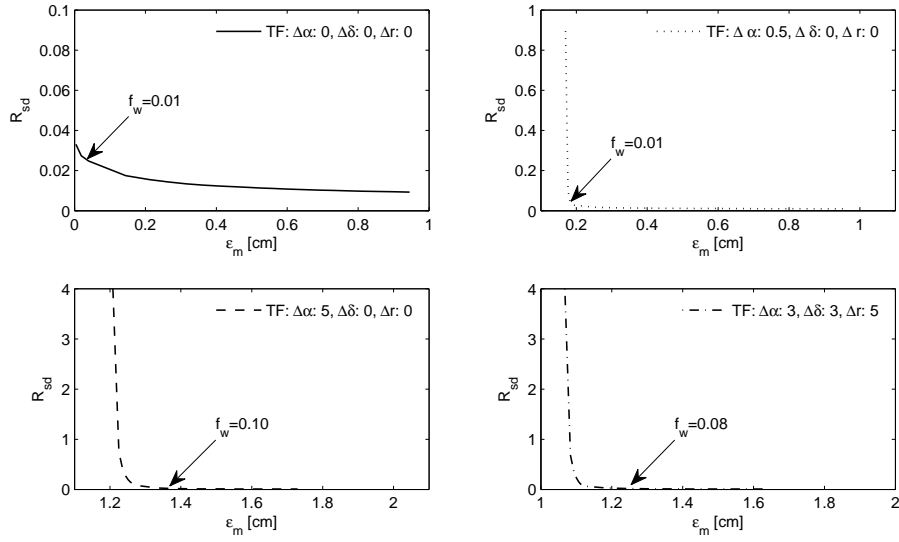


Figure 5.6: Roughness of the slip distribution  $R_{sd}$  as a function of the RMSE of the misfit  $\varepsilon_m$ . The arrows indicate the smoothness weight and roughness corresponding to the minimum RMSE of the slip distribution  $\varepsilon_{sd}$ . Note that the scale of the axes is different for each plot. A large roughness  $R_{sd}$  corresponds to a small average misfit.



### 5.3 Influence of errors in fault plane orientation

The orientation of the fault plane is defined by its strike, dip, and rake. The error in strike is denoted by  $\Delta\alpha$ ; errors in dip and rake are denoted by  $\Delta\delta$  and  $\Delta r$ , respectively. For all six synthetic interferograms, the RMSE of the slip distribution  $\varepsilon_{sd}$  and misfit  $\varepsilon_m$  are calculated for the range  $[-10^\circ < \Delta\alpha < 10^\circ]$ ,  $[-10^\circ < \Delta\delta < 10^\circ]$ , and  $[-10^\circ < \Delta r < 10^\circ]$  individually. Next, (some) possible relations between these three parameters are investigated by adding an additional error of  $5^\circ$  to one of the fixed parameters. These relations can be taken into account when optimizing the fault plane geometry. For example, one would like to know whether the strike corresponding to the minimum misfit remains constant for different errors in dip and rake. In theory, to investigate all possible relations between the individual orientation parameters would correspond to computing  $\varepsilon_{sd}$  and  $\varepsilon_m$  at  $[-10^\circ < \Delta\alpha < 10^\circ]$  for  $[-10^\circ < \Delta\delta < 10^\circ]$  and  $[-10^\circ < \Delta r < 10^\circ]$ , which is a large three-dimensional search space. Therefore, the investigation is confined to the following tests:

**Case 1** - for the TF, NF, and RF at  $\theta_{az} = 180^\circ$  and  $\theta_{az} = 90^\circ$ :

- $\varepsilon_{sd}$  and  $\varepsilon_m$  at  $[-10^\circ < \Delta\alpha < 10^\circ]$  for  $\Delta\delta = 0^\circ$  and  $\Delta r = 0^\circ$ ;
- $\varepsilon_{sd}$  and  $\varepsilon_m$  at  $[-10^\circ < \Delta\delta < 10^\circ]$  for  $\Delta r = 0^\circ$  and  $\Delta\alpha = 0^\circ$ ;
- $\varepsilon_{sd}$  and  $\varepsilon_m$  at  $[-10^\circ < \Delta r < 10^\circ]$  for  $\Delta\alpha = 0^\circ$  and  $\Delta\delta = 0^\circ$ .

**Case 2** - for the TF, NF, and RF at  $\theta_{az} = 180^\circ$  and  $\theta_{az} = 90^\circ$ :

- $\varepsilon_{sd}$  and  $\varepsilon_m$  at  $[-10^\circ < \Delta\alpha < 10^\circ]$  for  $\Delta\delta = 5^\circ$  and  $\Delta r = 0^\circ$ ;
- $\varepsilon_{sd}$  and  $\varepsilon_m$  at  $[-10^\circ < \Delta\alpha < 10^\circ]$  for  $\Delta\delta = 0^\circ$  and  $\Delta r = 5^\circ$ ;
- $\varepsilon_{sd}$  and  $\varepsilon_m$  at  $[-10^\circ < \Delta\delta < 10^\circ]$  for  $\Delta r = 5^\circ$  and  $\Delta\alpha = 0^\circ$ ;
- $\varepsilon_{sd}$  and  $\varepsilon_m$  at  $[-10^\circ < \Delta\delta < 10^\circ]$  for  $\Delta r = 0^\circ$  and  $\Delta\alpha = 5^\circ$ ;
- $\varepsilon_{sd}$  and  $\varepsilon_m$  at  $[-10^\circ < \Delta r < 10^\circ]$  for  $\Delta\alpha = 5^\circ$  and  $\Delta\delta = 0^\circ$ ;
- $\varepsilon_{sd}$  and  $\varepsilon_m$  at  $[-10^\circ < \Delta r < 10^\circ]$  for  $\Delta\alpha = 0^\circ$  and  $\Delta\delta = 5^\circ$ .

The results of the tests of case 1 are summarized in Figure 5.7, which shows the influence of errors in strike, dip, and rake, while keeping the other parameters fixed at their correct value. Furthermore, Table 5.2 shows the ratios of  $\varepsilon_m$  and  $\varepsilon_{sd}$  for an error of  $3^\circ$  and  $5^\circ$  in one of the three fault plane orientation parameters, compared to  $\varepsilon_m$  and  $\varepsilon_{sd}$  of the original fault plane geometry. The first difference that can be observed is the difference between strike, dip, and rake. Generally, a typical error in strike of  $5^\circ$  results in a 2–3 times larger RMSE in slip distribution and misfit than an error in dip and rake of equal magnitude (except for the transform fault at  $\theta_{az} = 180^\circ$ ). A second observation is the difference between different earthquake types. In general, normal faults and reverse faults seem to be affected more by errors in strike than transform faults, but a transform fault is affected more by an error in rake than a normal fault or reverse fault. A third observation is the difference in sensitivity due to different azimuth angles, in particular for the transform fault. Each of these observations will now be discussed in more detail.

The relative differences visible in Figure 5.7 can be explained by investigating the surface displacement field in relation with the satellite incidence angle  $\theta_i$  and the type of earthquake. Since  $\theta_i = 23^\circ$ , the satellite is more sensitive to vertical displacements than horizontal displacements. This explains why the number of fringes visible in the synthetic interferograms for the transform fault, normal fault, and reverse fault are different: the surface displacements of the transform fault are smaller in magnitude than those of the

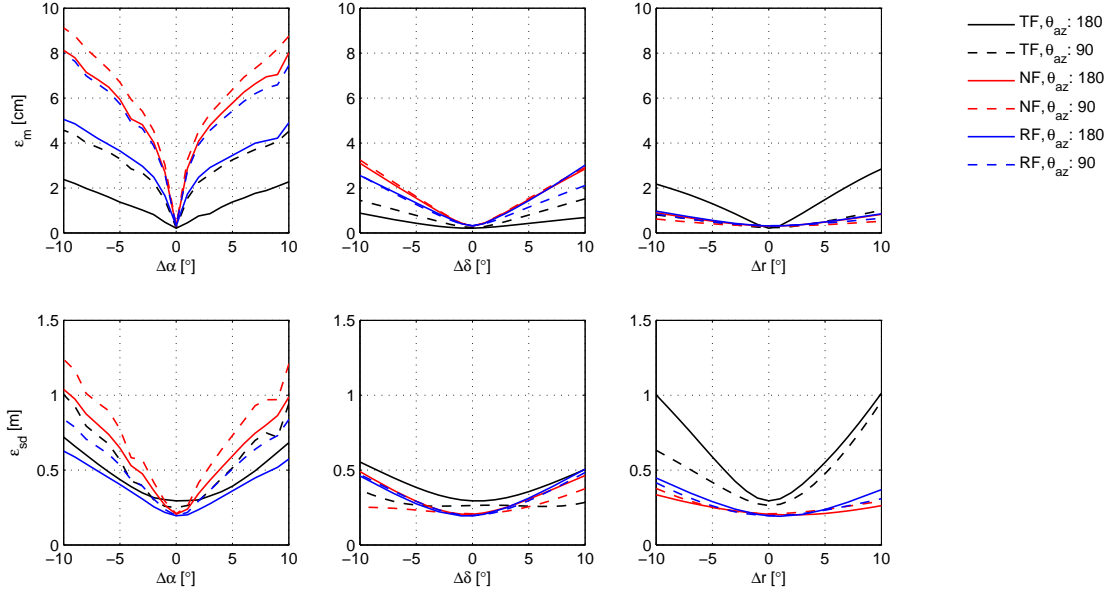


Figure 5.7: Plots of case 1:  $\epsilon_m$  and  $\epsilon_{sd}$  at  $[-10^\circ < \Delta\alpha < 10^\circ]$  for  $\Delta\delta = 0^\circ$  and  $\Delta r = 0^\circ$ ,  $[-10^\circ < \Delta\delta < 10^\circ]$  for  $\Delta r = 0^\circ$  and  $\Delta\alpha = 0^\circ$ , and  $[-10^\circ < \Delta r < 10^\circ]$  for  $\Delta\alpha = 0^\circ$  and  $\Delta\delta = 0^\circ$ . The different earthquake types are shown in black, red, and blue. Note that  $\epsilon_m$  is in [cm] and  $\epsilon_{sd}$  in [m].

normal fault and the reverse fault, because the transform fault causes horizontal displacements only, while the displacements caused by a normal fault are predominantly vertical and reverse faults cause a mixture between horizontal and vertical displacements.

The first observation, the difference in influence between errors in strike and the other two orientation parameters, can be explained as follows. An error in strike will result in a different fault trace at the Earth's surface. For normal faults and reverse faults, one side of the fault will move up or down relative to the other side of the fault. This means that, for an error in strike, part of the observations show surface displacements in the opposite direction than what would be expected based on the model. This effect is illustrated in Figure 5.8. The same holds for transform faults when they are viewed from a direction parallel to the strike. For an error in dip, assuming that the fault is a rupturing fault, the RMSE in slip distribution and misfit is much less significant. This is because an error in dip does not change the position of the fault trace, but it affects the amplitude of the surface displacements on both sides of the fault in a particular LOS. Similarly, an error in rake does not change the position of the fault trace as well, but it influences the direction of the displacements.

A similar reasoning can be applied to explain the second observation: the relative differences due to different earthquake types. Slip distributions estimated on normal faults seem to be affected more by a change in strike than transform faults or reverse faults. This is due to the fact that more surface displacements in satellite LOS are observed for normal faults compared to transform faults. This increases the effect explained in Figure 5.8. The opposite is true for the rake: since transform faults show less surface displacements in satellite LOS, the relative change in displacements is larger for the same error in rake compared to normal faults and reverse faults. The RMSE of the misfit for the normal fault and the reverse fault even shows no significant increase within the investigated error range of the rake.

Table 5.2:  $\varepsilon_m$  and  $\varepsilon_{sd}$  ratios for an error of  $3^\circ$  and  $5^\circ$  in one of the three fault plane orientation parameters, compared to  $\varepsilon_m$  and  $\varepsilon_{sd}$  of the original fault plane orientation (without errors). The absolute values for  $\varepsilon_m$  and  $\varepsilon_{sd}$  of the original fault plane orientation are given in bold in the first row of both blocks. This table shows the relative sensitivity of the slip distribution and misfit to errors in strike, dip, and rake.

Earthquake type		TF	TF	NF	NF	RF	RF
$\theta_{az}$		180°	90°	180°	90°	180°	90°
$\varepsilon_m$ [cm]		<b>0.21</b>	<b>0.23</b>	<b>0.31</b>	<b>0.30</b>	<b>0.31</b>	<b>0.32</b>
$\varepsilon_m$ (ratio)	$\Delta\alpha = 3^\circ$	4.8	11.4	15.8	17.9	9.6	14.5
	$\Delta\alpha = 5^\circ$	6.5	14.1	19.4	22.1	13.6	17.8
	$\Delta\delta = 3^\circ$	1.4	2.2	3.1	3.3	2.7	2.5
	$\Delta\delta = 5^\circ$	2.0	3.3	5.1	5.3	5.9	3.9
	$\Delta r = 3^\circ$	4.0	1.5	1.3	1.1	1.4	1.2
	$\Delta r = 5^\circ$	6.2	2.1	1.7	1.3	1.8	1.5
$\varepsilon_{sd}$ [m]		<b>0.29</b>	<b>0.25</b>	<b>0.21</b>	<b>0.21</b>	<b>0.19</b>	<b>0.20</b>
$\varepsilon_{sd}$ (ratio)	$\Delta\alpha = 3^\circ$	1.2	1.6	2.3	2.7	1.6	2.0
	$\Delta\alpha = 5^\circ$	1.5	2.3	3.2	3.7	2.5	2.7
	$\Delta\delta = 3^\circ$	1.1	1.0	1.1	1.1	1.4	1.2
	$\Delta\delta = 5^\circ$	1.3	1.0	1.4	1.1	1.8	1.5
	$\Delta r = 3^\circ$	1.5	1.3	1.1	1.1	1.2	1.1
	$\Delta r = 5^\circ$	2.0	1.6	1.2	1.2	1.5	1.3

The third observation, which is the difference due to different azimuth angles that partly determine the satellite LOS, confirms the explanations for the differences between normal faults and reverse faults on the one hand and transform faults on the other hand, since the RMSE of the slip distribution and misfit computed for the transform fault at an azimuth angle  $\theta_{az} = 90^\circ$  starts to show the behavior of  $\varepsilon_{sd}$  and  $\varepsilon_m$  for the reverse fault and normal fault. This is due to the surface displacement field of the transform fault at  $\theta_{az} = 90^\circ$ , which shows two areas in the surface displacement field (one corresponding to an increase in range and one corresponding to a decrease in range), which is similar to the normal fault and reverse fault.

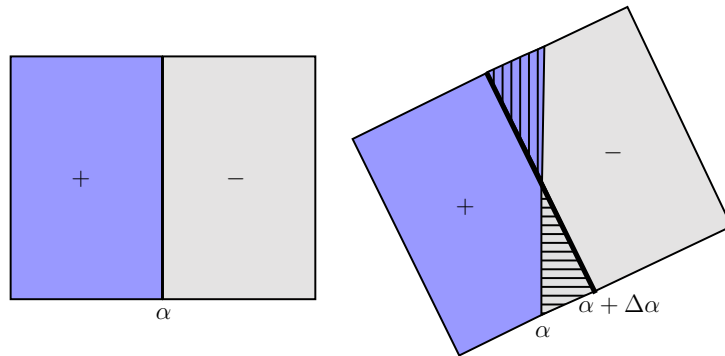


Figure 5.8: Example of the effect of an error in strike on the measured and modeled surface displacement field. The blue part corresponds to an observed increase in range towards the satellite, the light-grey part corresponds to an observed decrease in range towards the satellite. The vertical line is the true strike, the thick black line is the erroneous strike. If such an error in strike is made, the blue shaded part in the observations would correspond to an increase in range, while according to the modeled strike this part should correspond to a decrease in range. Similarly, the light-grey shaded part corresponds to a decrease in range in the observations, but an increase in range would be expected in the model.

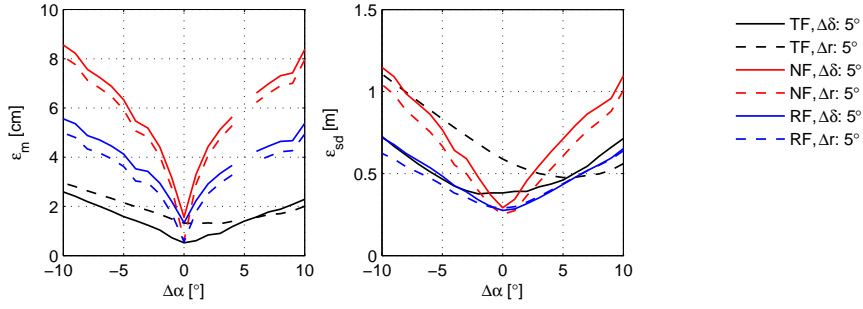


Figure 5.9: Plots of  $\varepsilon_m$  and  $\varepsilon_{sd}$  at  $[-10^\circ < \Delta\alpha < 10^\circ]$  for  $\Delta\delta = 5^\circ$  and  $\Delta r = 0^\circ$ , and  $\Delta\delta = 0^\circ$  and  $\Delta r = 5^\circ$  (case 2). The different earthquake types are shown in black, red, and blue. Note that  $\varepsilon_m$  is in [cm] and  $\varepsilon_{sd}$  in [m].

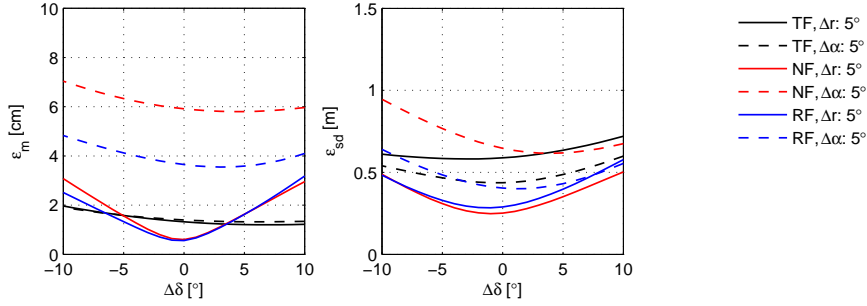


Figure 5.10: Plots of  $\varepsilon_m$  and  $\varepsilon_{sd}$  at  $[-10^\circ < \Delta\delta < 10^\circ]$  for  $\Delta\alpha = 0^\circ$  and  $\Delta r = 5^\circ$ , and  $\Delta\alpha = 5^\circ$  and  $\Delta r = 0^\circ$  (case 2). The different earthquake types are shown in black, red, and blue. Note that  $\varepsilon_m$  is in [cm] and  $\varepsilon_{sd}$  in [m].

Figure 5.9 shows plots of  $\varepsilon_{sd}$  and  $\varepsilon_m$  at  $[-10^\circ < \Delta\alpha < 10^\circ]$  for  $\Delta\delta = 5^\circ$  and  $\Delta r = 0^\circ$ , and  $\Delta\delta = 0^\circ$  and  $\Delta r = 5^\circ$  (case 2) at  $\theta_{az} = 180^\circ$ . For normal faults and reverse faults, the minimum in both  $\varepsilon_{sd}$  and  $\varepsilon_m$  still corresponds to the correct strike if an error in dip or rake is introduced. However, for the transform fault, an error in rake shifts the optimal strike (dashed black line in Figure 5.9). This shift is roughly one-to-one, i.e. an error in rake of  $5^\circ$  results in a shift of optimal strike of approximately  $5^\circ$  and vice versa. An error in dip does not change the strike corresponding to the minimum in  $\varepsilon_{sd}$  and  $\varepsilon_m$ . A similar plot of case 2 for the dip is shown in Figure 5.10. For the normal fault and the reverse fault, an error in rake does not influence the optimal dip. This is not the case for the transform fault, where apparently an error in rake slightly shifts the optimal dip. A shift of similar magnitude is caused by an error in strike for all three fault types. Finally, the results of case 2 for the rake at  $\theta_{az} = 180^\circ$  are shown in Figure 5.11. An error in strike results in a significant shift in optimal rake for transform faults (roughly one-to-one). The same error in strike introduced in the geometry of the normal fault and the reverse fault do not show a clear shift in optimal rake, but rather show large errors over the entire error range  $[-10^\circ < \Delta r < 10^\circ]$ . An error in dip, however, does not have much effect on the optimal rake for all three earthquake types.

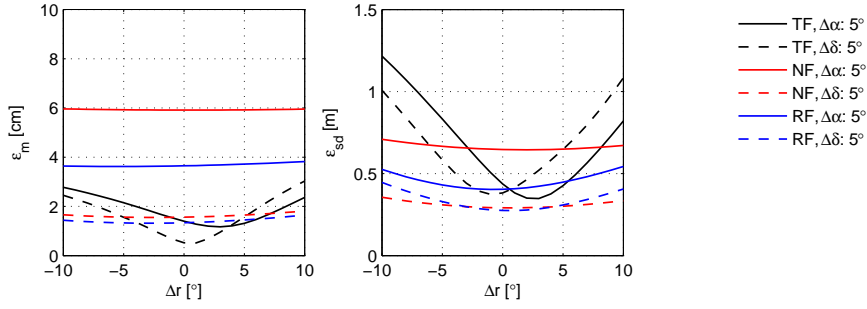


Figure 5.11: Plots of  $\varepsilon_m$  and  $\varepsilon_{sd}$  at  $[-10^\circ < \Delta r < 10^\circ]$  for  $\Delta\alpha = 5^\circ$  and  $\Delta\delta = 0^\circ$ , and  $\Delta\alpha = 0^\circ$  and  $\Delta\delta = 5^\circ$  (case 2). The different earthquake types are shown in black, red, and blue. Note that  $\varepsilon_m$  is in [cm] and  $\varepsilon_{sd}$  in [m].

The same tests for the data sets at  $\theta_{az} = 90^\circ$  show similar results, only the transform fault at this azimuth angle shows a sensitivity to the errors in fault plane geometry similar to those of the normal fault and the reverse fault at  $\theta_{az} = 180^\circ$ .

The strike and rake are more correlated than the strike and dip, and the dip and rake. For the transform fault at  $\theta_{az} = 180^\circ$ , this relation between the strike and the rake is roughly one-to-one. Thus, for real-world cases, either the rake or strike should be fixed after an initial guess of the fault plane geometry. Since an error in dip of about  $5^\circ$  has almost no effect on the optimal strike and rake, this parameter can be optimized after the rake and strike have been determined.

## 5.4 Influence of errors in fault plane position

The position of the fault plane is specified by the x- and y-coordinate of the top-center of the fault plane. In case of a blind fault, the position would correspond to the position of the top-center of a virtual extension of the plane reaching to the Earth's surface. To investigate the effect of an error in the position ( $\Delta x, \Delta y$ ) of the fault plane,  $\varepsilon_{sd}$  and  $\varepsilon_m$  are computed for  $\Delta x = \pm[0, 1, 2, 5, 10]$  km and  $\Delta y = \pm[0, 1, 2, 5, 10]$  km, including all possible combinations between the two error ranges. The results are shown as contour plots in Figure 5.12 for  $\theta_{az} = 180^\circ$  and Figure 5.13 for  $\theta_{az} = 90^\circ$ .

An error in position of the transform fault at  $\theta_{az} = 180^\circ$  results in a 2–3 times smaller RMSE of the slip distribution and misfit than a similar error in position of the normal fault or reverse fault (Table 5.3), or the transform fault at  $\theta_{az} = 90^\circ$ . These differences can be explained following the same reasoning used to explain the relative differences in sensitivity to errors in fault plane orientation, as discussed in Section 5.3.

As expected, an error in the direction perpendicular to the strike results in a 2–3 times larger RMSE than an error in the direction parallel to the strike. The shape of the contours reflects the orientation of the fault plane. Errors in slip distribution and misfit caused by a position error in the direction parallel to the strike are due to the fact that not all slip is covered on the fault plane (the fault plane becomes too small on one side). Thus, if the dimensions of the fault plane are chosen such that all significant slip is covered, optimization of the position of the fault plane in the direction parallel to the strike is not necessary.

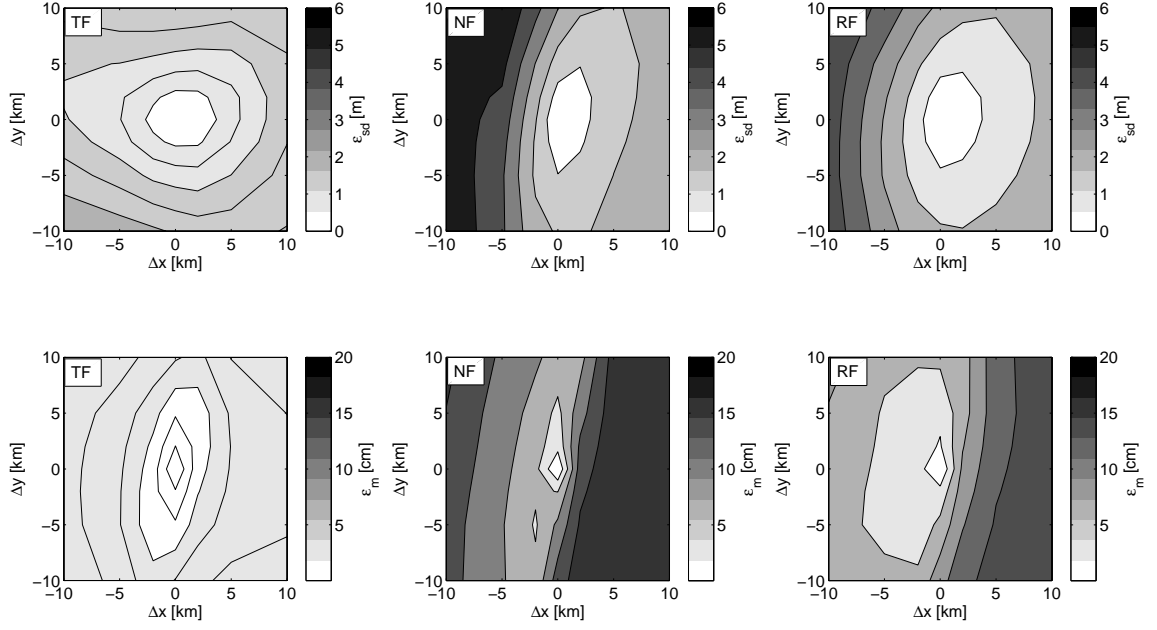


Figure 5.12: Plots of  $\varepsilon_{sd}$  and  $\varepsilon_m$  for  $\Delta x = \pm[0, 1, 2, 5, 10]$  km and  $\Delta y = \pm[0, 1, 2, 5, 10]$  km with  $\theta_{az} = 180^\circ$ . Note the relation between the contours and the orientation of the fault planes.

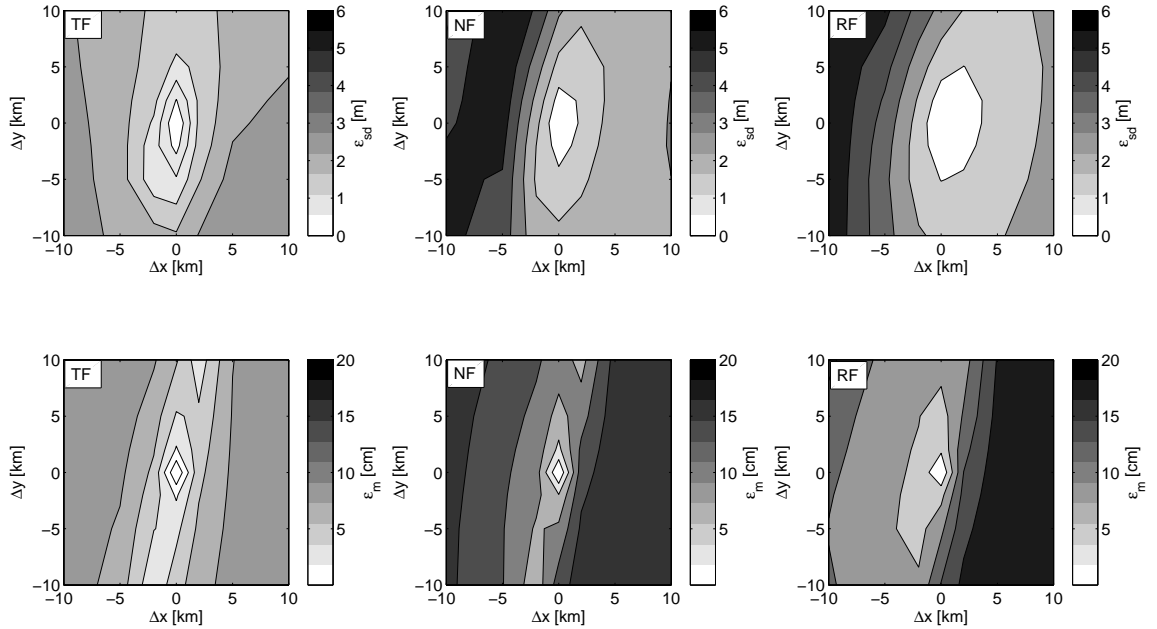


Figure 5.13: Plots of  $\varepsilon_{sd}$  and  $\varepsilon_m$  for  $\Delta x = \pm[0, 1, 2, 5, 10]$  km and  $\Delta y = \pm[0, 1, 2, 5, 10]$  km with  $\theta_{az} = 90^\circ$ . Note the relation between the contours and the orientation of the fault planes.

Table 5.3:  $\varepsilon_m$  and  $\varepsilon_{sd}$  ratios for an error of 2 km and 5 km in x-direction and y-direction, compared to  $\varepsilon_m$  and  $\varepsilon_{sd}$  of the original fault plane position (without errors). The absolute values for  $\varepsilon_m$  and  $\varepsilon_{sd}$  of the original fault plane position are given in bold in the first row of both blocks. From this table it can be concluded that the slip distribution estimation is more sensitive to an error in the position perpendicular to the strike than parallel to the strike. Furthermore, an error in position has less influence on the slip distribution estimated for the transform fault at  $\theta_{az} = 180^\circ$  compared to the other cases.

Earthquake type		TF	TF	NF	NF	RF	RF
$\theta_{az}$		180°	90°	180°	90°	180°	90°
$\varepsilon_m$ [cm]		<b>0.21</b>	<b>0.23</b>	<b>0.31</b>	<b>0.30</b>	<b>0.31</b>	<b>0.32</b>
$\varepsilon_m$ (ratio)	$\Delta x = 2$ km	8.6	27.7	45.2	47.3	30.3	46.7
	$\Delta x = 5$ km	13.3	38.0	60.2	59.4	44.8	64.7
	$\Delta y = 2$ km	3.9	14.5	14.0	18.7	9.5	14.4
	$\Delta y = 5$ km	7.4	21.8	18.7	27.5	12.3	18.4
$\varepsilon_{sd}$ [m]		<b>0.29</b>	<b>0.25</b>	<b>0.21</b>	<b>0.21</b>	<b>0.19</b>	<b>0.20</b>
$\varepsilon_{sd}$ (ratio)	$\Delta x = 2$ km	1.2	6.0	4.1	6.4	3.1	3.9
	$\Delta x = 5$ km	2.9	8.5	9.2	12.7	6.9	8.2
	$\Delta y = 2$ km	1.7	2.5	3.6	3.9	2.9	3.5
	$\Delta y = 5$ km	3.8	5.2	8.2	8.5	6.8	8.0

## 5.5 Influence of errors in fault plane dimensions

The dimensions of the fault plane are determined by its length  $L$  and the depth extent ( $d_{min}, d_{max}$ ). To test the effect of errors in fault plane dimensions, the slip distribution is estimated for a number of cases. Table 5.4 shows the different dimensions tested for all data sets and the corresponding RMSE of the misfit between the model and the observations. The RMSE of the slip distribution  $\varepsilon_{sd}$  could be calculated by assuming zero slip on the missing patches of the estimated and / or original slip distribution. However, due to the differences in fault plane size the values for  $\varepsilon_{sd}$  cannot be compared with the  $\varepsilon_{sd}$  values obtained by other fault plane geometry errors. Therefore, instead the seismic moment  $M_0$  and the location and magnitude of maximum slip on the fault plane are given in Table 5.5. From these results it can be concluded that an increase in fault plane dimensions has negligible influence on the slip distribution estimation. However, a fault plane with

Table 5.4: New fault plane dimensions and corresponding RMSE of the misfit  $\varepsilon_m$  for the transform fault. Original dimensions are:  $L = 30$  km and  $(d_{min}, d_{max}) = (0, 15)$  km.

Earthquake type		TF	TF	NF	NF	RF	RF
$\theta_{az}$		180°	90°	180°	90°	180°	90°
$L$	$(d_{min}, d_{max})$	$\varepsilon_m$ [cm]					
20 km	(0,10) km	1.8	1.8	4.3	4.1	4.3	4.9
20 km	(0,15) km	1.5	1.7	4.0	3.8	3.9	4.4
20 km	(0,20) km	1.5	1.7	4.0	3.8	3.9	4.4
30 km	(0,10) km	0.6	0.6	1.1	1.0	1.8	1.7
30 km	(0,15) km	0.2	0.2	0.3	0.3	0.3	0.3
30 km	(5,20) km	2.4	5.0	10	9.7	11	12
30 km	(0,30) km	0.2	0.2	0.3	0.3	0.3	0.3
40 km	(0,20) km	0.2	0.3	0.3	0.3	0.3	0.3
60 km	(0,15) km	0.2	0.2	0.3	0.3	0.3	0.3

Table 5.5: Seismic moment  $M_0$  in [Nm] and maximum slip for the transform fault, normal fault, and reverse fault at  $\theta_{az} = 180^\circ$ . The approximate depth of maximum slip is given between brackets. All but the three lowest seismic moment values result in a moment magnitude  $M_W = 6.9$ , which corresponds to the moment magnitude of the original slip distribution.

Earthquake type		TF at $\theta_{az} = 180^\circ$		NF at $\theta_{az} = 180^\circ$		RF at $\theta_{az} = 180^\circ$	
$L$	$(d_{min}, d_{max})$	$M_0$	$s_{max}$ [m]	$M_0$	$s_{max}$ [m]	$M_0$	$s_{max}$ [m]
20 km	(0,10) km	$2.1 \cdot 10^{19}$	5.0 (6 km)	$2.6 \cdot 10^{19}$	6.6 (7 km)	$2.4 \cdot 10^{19}$	5.9 (7 km)
20 km	(0,15) km	$2.6 \cdot 10^{19}$	4.2 (1 km)	$2.9 \cdot 10^{19}$	5.3 (7 km)	$2.7 \cdot 10^{19}$	4.9 (7 km)
20 km	(0,20) km	$2.8 \cdot 10^{19}$	4.3 (1 km)	$2.9 \cdot 10^{19}$	5.3 (7 km)	$2.7 \cdot 10^{19}$	4.9 (6 km)
30 km	(0,10) km	$2.7 \cdot 10^{19}$	5.4 (6 km)	$2.9 \cdot 10^{19}$	5.7 (7 km)	$2.8 \cdot 10^{19}$	5.5 (7 km)
30 km	(0,15) km	$3.1 \cdot 10^{19}$	4.4 (5 km)	$3.1 \cdot 10^{19}$	4.8 (5 km)	$3.1 \cdot 10^{19}$	4.8 (5 km)
30 km	(5,20) km	$2.4 \cdot 10^{19}$	10.9 (6 km)	$2.1 \cdot 10^{19}$	15.3 (6 km)	$1.7 \cdot 10^{19}$	10.8 (6 km)
30 km	(0,30) km	$3.1 \cdot 10^{19}$	4.3 (4 km)	$3.1 \cdot 10^{19}$	4.8 (5 km)	$3.1 \cdot 10^{19}$	4.8 (5 km)
40 km	(0,20) km	$3.2 \cdot 10^{19}$	4.4 (4 km)	$3.1 \cdot 10^{19}$	4.8 (5 km)	$3.1 \cdot 10^{19}$	4.8 (5 km)
60 km	(0,15) km	$3.1 \cdot 10^{19}$	4.4 (5 km)	$3.1 \cdot 10^{19}$	4.8 (5 km)	$3.1 \cdot 10^{19}$	4.8 (5 km)

dimensions that are too small results in errors. Especially an error in fault plane length or minimum depth extent can cause significant errors in model and slip distribution. Thus, it is better to extend the fault plane to larger dimensions if a realistic initial guess of the fault plane size is not possible.

## 5.6 Influence of atmospheric delay variations

The earthquakes that have been considered in the previous sections can also be used to test the influence of atmospheric delay variations in the InSAR observations. The methodology and results are discussed in this section.

### 5.6.1 Methodology

Errors due to spatial and temporal variations in atmospheric delay have been discussed in Section 3.2.4. One can describe the atmospheric delay variations in an interferogram as a sum of many different periodic atmospheric signals, each with a different angular wave number  $f$ . The relative significance of signals corresponding to different angular wave numbers can be examined by computing the power spectrum of the interferogram. Based on the power spectra observed for eight different atmospheric interferograms, Hanssen (2001) proposed an empirical atmospheric model based on power laws with three scaling regimes to approximate the power spectrum:

$$P(f) = \begin{cases} P_I(f_0/f)^{-5/3} & \text{for } 1.5 \leq (f_0/f) < 50 \text{ km;} \\ P_0(f_0/f)^{-8/3} & \text{for } 0.25 \leq (f_0/f) < 1.5 \text{ km;} \\ P_{III}(f_0/f)^{-2/3} & \text{for } 0.02 \leq (f_0/f) < 0.25 \text{ km;} \end{cases} \quad (5.2)$$

where  $P(f)$  is the power as a function of the wave number,  $f_0$  is a normalized wave number (1 cycle/km), and  $P_0$ ,  $P_I$ , and  $P_{III}$  are scaling parameters defined such that  $P(f)$  is continuous.

The above atmospheric model is used to create many realizations of atmospheric delay. These realizations are then used as observations to estimate the slip distribution on the



fault planes corresponding to the three earthquake types. The estimated slip distributions reflect typical errors that can be expected due to atmospheric delay variations.

The maximum variation in atmospheric delay depends on the value chosen for  $P_0$  (the power initialization value at 1 cycle/km) and on the initial set of random numbers used to simulate the atmospheric delay. For the same set of random numbers, the difference between the maximum and minimum delay is doubled if the value chosen for  $P_0$  is doubled. In this study, this parameter is fixed to  $P_0 = 1.0$ . For other values of  $P_0$ , the atmospheric delay and the results discussed in Section 5.6.2 are scaled accordingly.

### 5.6.2 Results and discussion

The RMSE of the slip distribution  $\varepsilon_{sd}$  for all simulations and for the transform fault, normal fault, and reverse fault at  $\theta_{az} = 180^\circ$  with two different smoothness weights  $f_w$  are summarized in Figure 5.14. Atmospheric delay variations result in a larger RMSE of the slip distribution for the transform fault compared to the normal fault and the reverse fault. This is due to the fact that the amplitude of the atmospheric delay variations is relatively larger for the transform fault, because less deformation due to the earthquake is observed in satellite LOS. Furthermore, a larger smoothness weight results in a smaller RMSE and standard deviation of this RMSE, because the slip distribution becomes more smooth for larger  $f_w$ . This reduces the possible spatial variability in slip distribution due to atmospheric delay variations.

The RMSE of the slip distribution due to atmospheric signals with  $P_0 = 1.0$  is low compared to slip distribution errors caused by errors in fault plane geometry. For all three faults, the mean of  $\varepsilon_{sd}$  lies below the  $\varepsilon_{sd}$  that is caused by the smoothness constraint, without introducing any noise or error in fault plane geometry. This suggests that atmospheric

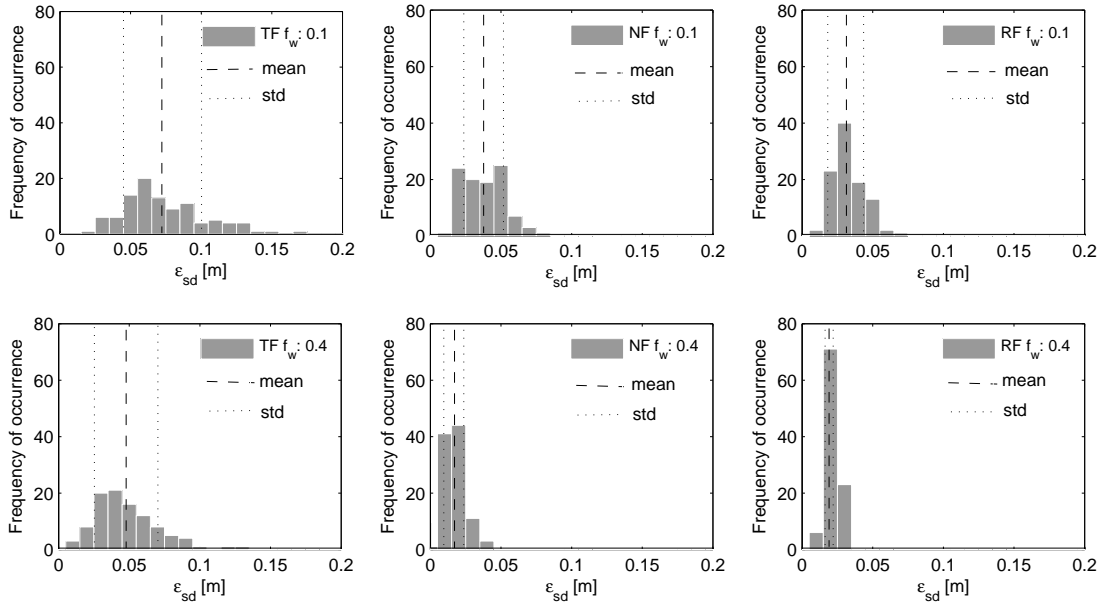


Figure 5.14: Histograms of the RMSE of the slip distribution  $\varepsilon_{sd}$  for all simulations of atmospheric delay and for the transform fault, normal fault, and reverse fault with two different smoothness weights  $f_w$ . The mean of  $\varepsilon_{sd}$  is shown as a dashed black line and the standard deviation (std) of  $\varepsilon_{sd}$  is shown as a dotted black line.

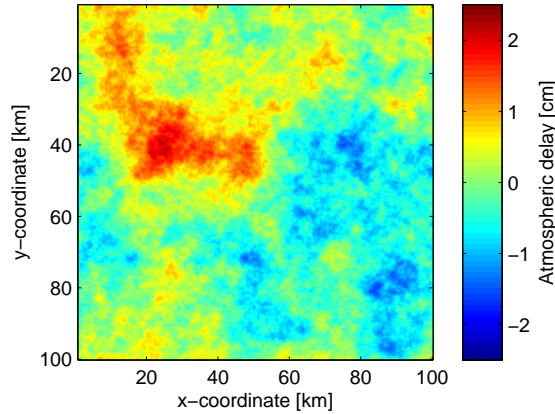


Figure 5.15: Atmospheric delay (realization 96 for the transform fault at  $\theta_{az} = 180^\circ$  with  $f_w = 0.1$ ).

signals in interferograms caused by average weather conditions have only a very small influence on the estimated slip distribution. However, this influence will gradually increase with decreasing surface deformation pattern (the relative weight of the atmospheric signal increases). Hence, the effect may be more significant for smaller earthquakes. For the transform fault at  $\theta_{az} = 180^\circ$  (with  $f_w = 0.1$ ), a value of  $P_0 \approx 4.0$  would on average equal  $\varepsilon_{sd}$  introduced by the smoothness constraint. Similarly, for the normal fault and the reverse fault at  $\theta_{az} = 180^\circ$ , the RMSE of the slip distribution introduced by the smoothness constraint equals the average error due to atmospheric delay with a value of  $P_0 \approx 5.5$  and  $P_0 \approx 5.9$ , respectively.

Extreme weather conditions will have more influence on the slip distribution estimation, but the cases in which this influence becomes significant may be rare. For example, Hanssen (2001) shows an interferogram of July 1995 with a temporal baseline of one day, covering the northern part of the Netherlands. A severe thunderstorm dominated the weather conditions during both acquisitions, resulting in a maximum atmospheric delay variation of about 8 cm. For comparison, the atmospheric delay realization which has the largest  $\varepsilon_{sd}$  of all realizations (realization 96 of the transform fault at  $f_w = 0.1$  results in  $\varepsilon_{sd} = 0.17$ ) shows a maximum difference in atmospheric delay over the interferogram of  $\sim 4$  cm (Figure 5.15). Due to the linearity of the inversion, the slip distribution estimated for this realization will be doubled if the observations are doubled. Such an error would be similar in magnitude to the error that is introduced by the smoothness constraint ( $\varepsilon_{sd} = 0.29$ ). Thus, the influence of atmospheric signals in interferograms on slip distribution estimations appears to be limited.

## 5.7 Summary and concluding remarks

### 5.7.1 Errors in fault plane geometry

This chapter showed the effect of errors in fault plane orientation, position, and dimensions for different earthquake types, viewed from two different satellite LOS. The following conclusions can be drawn from the results presented in this chapter:

- An error in strike has more effect on the RMSE of the slip distribution and misfit than an error in dip or rake; especially the normal fault and reverse fault are affected. This is due to a change in fault trace at the surface, which introduces relatively large errors in the surface deformation pattern.
- An error in strike or rake affects the optimal value for the other parameters. In particular this is the case for the transform fault at  $\theta_{az} = 180^\circ$ . An error in dip has negligible influence on the optimal strike and rake, and can therefore be optimized independently.
- Errors in strike and the position perpendicular to the strike have much more effect on a normal fault or reverse fault compared to the transform fault for this satellite incidence angle ( $\theta_i = 23^\circ$ ).
- Errors in fault plane position parallel to the strike have less effect than errors in fault plane position perpendicular to the strike. Thus, contours reflecting the RMSE in slip distribution and misfit generally follow the direction of the strike.
- An increase in fault plane dimensions has negligible influence on the slip distribution estimation. A decrease in dimensions, however, introduces significant errors in the slip distribution, especially errors in fault plane length and minimum depth extent.

It can be concluded that optimization of all parameters independently is not possible due to correlation between the parameters, which results in a very large search space. This should then be done with a non-linear optimization scheme, but this approach is not considered in this study. However, an initial inspection of the interferogram enables one to predict the sensitivity of the slip distribution to different fault plane geometry parameters, which is found to be mainly a combination between earthquake type and satellite LOS. More specific, the larger the differences in surface deformation between one side of the fault trace and the other in satellite LOS, the more sensitive the slip distribution estimation is to errors in strike and fault plane position. At the same time, the sensitivity to an error in rake decreases. Table 5.6 summarizes the parameters for which the investigated earthquake slip distributions are most and least sensitive. This information can be used in real-world cases to focus on the optimization of certain parameters (those parameters to which the slip distribution is most sensitive), while other parameters may remain fixed (the parameters to which the slip distribution is found to be least sensitive).

Table 5.6: Overview of the sensitivity analysis. Both the parameters to which the slip distribution is most and least sensitive are given. A distinction is made between a horizontal component of the LOS-vector near-perpendicular to the strike and near-parallel to the strike.

		LOS	
		$\perp$ to strike	$\parallel$ to strike
<b>TF</b>	<b>most sensitive to</b>	rake	strike, position
	<b>least sensitive to</b>	dip, position	dip
<b>NF</b>	<b>most sensitive to</b>	strike, position	strike, position
	<b>least sensitive to</b>	dip, rake	dip, rake
<b>RF</b>	<b>most sensitive to</b>	strike, position	strike, position
	<b>least sensitive to</b>	dip	dip, rake

### 5.7.2 Errors in observations due to atmospheric delay variations

An empirical atmospheric model has been used to create realizations of typical atmospheric delay variations under normal weather conditions. For all three earthquake types that have been investigated, the effect on the estimated slip distribution of atmospheric signals of this magnitude is limited and generally smaller than the error introduced by the smoothness constraint.

## Chapter 6

# Case study on the 1999 Hector Mine earthquake

At October 16, 1999, an earthquake occurred in the Eastern California Shear Zone (ECSZ), named after a nearby quarry known as the ‘Hector Mine’. The earthquake occurred in a remote part of the Mojave Desert, located approximately 20 km to the East of the Lander’s earthquake that occurred in 1992 (Kaverina et al., 2002). Due to the arid environment and lack of extensive human activity, SAR acquisitions can be processed to relatively coherent interferograms even for very long temporal baselines. This makes the Hector Mine earthquake an interesting subject of study.

This chapter presents the results of a case study of the Hector Mine earthquake. A description of the case study area and earthquake characteristics is given in Section 6.1. In Section 6.2, the observations from InSAR data are discussed. This is followed by a discussion of the fault plane geometry optimization and slip distribution inversion in Section 6.3. The final model is then used to investigate the influence of different data reduction techniques and degrees of data reduction in Section 6.4 (research objective 3). Finally, concluding remarks are presented in Section 6.5.

### 6.1 Tectonic setting and earthquake characteristics

The ECSZ is located on the boundary of the Pacific and North-American plate. It is an area with a high seismic activity. Based on slip rates of faults in this zone it is suggested that about 15% of the motion between the Pacific and North-American plate occurs in this zone (Sauber et al., 1986). Figure 6.1 shows the general tectonic setting of the plate boundary between the Pacific and the North-American plate. The Pacific plate moves to the North-West; the North-American plate to the South-East. Therefore, the plate boundary results in earthquakes on mainly right-lateral transform faults.

The study area is shown in Figure 6.2. The earthquake has a moment magnitude of  $M_W = 7.1$  ( $M_0 = 5.98 \cdot 10^{19}$  Nm, Harvard CMT catalog). Due to the remote location of the earthquake, little damage occurred despite the magnitude of the earthquake. According to the information available in the Harvard CMT catalog, the fault of the Hector Mine earthquake has a dip of  $80^\circ$  and a rake of  $174^\circ$ , which corresponds to a predominantly right-lateral fault. The depth of the earthquake focus is listed at 15 km.

Studies of the fault trace have shown that the fault plane is approximately 41 km in length (Ji et al., 2002), which is in some studies divided in smaller sub-faults of variable strike and dip with locations corresponding to mapped fault traces (Jónsson, 2002). The sub-faults have been found to vary up to a maximum of  $24^\circ$  in strike and  $10^\circ$  in dip (Ji et al., 2002). The Harvard CMT fault plane solution is shown in Figure 6.2.

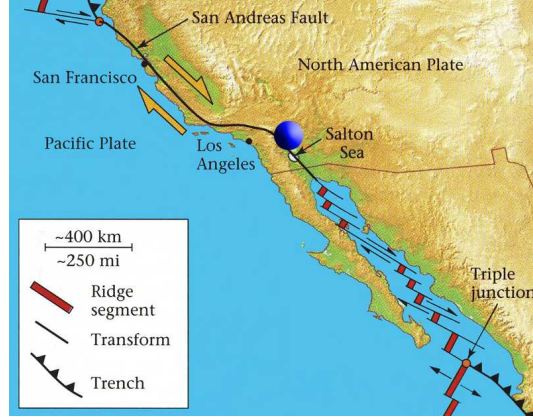


Figure 6.1: Plate boundary between the Pacific plate and North-American plate (adapted from Marshak (2001)). The location of the Hector Mine earthquake is indicated with the blue dot.

## 6.2 InSAR data

Two ascending ERS-2 SAR images are selected and processed to a coseismic interferogram of the Hector Mine earthquake: orbit 2937 acquired at November 12, 1995 and orbit 23979 acquired at November 21, 1999. These data are processed with DORIS as described in Section 3.2.2. Focusing and other preprocessing has been performed by ESA. Topography is removed by using an SRTM DEM. The wrapped interferogram is filtered using an adaptive filter developed by Goldstein and Werner (1998) and multi-looked  $5 \times 1$ , yielding square pixels with a resolution of 20 m. Finally, unwrapping is performed with SNAPHU (Statistical-cost, Network-flow Algorithm for Phase Unwrapping), proposed by Chen and Zebker (2000). Due to the overall good coherence of the interferogram and the absence of ‘islands’ (parts of the interferogram that are enclosed by decorrelated parts), unwrapping errors are expected to be limited. The unwrapped interferogram is shown in Figure 6.3.

The interferogram (Figure 6.2) has a temporal baseline of 1470 days ( $\sim 4$  years), which is rather large. However, due to the remote location of the area and its arid climate, the coherence of the interferogram is good, except for the region around the fault trace and some smaller regions further away from the fault. Fialko et al. (2001) inspected an interferogram spanning four years to two months prior to the earthquake, which shows no significant deformation. Therefore, it is assumed that the ascending interferogram shows primarily coseismic deformation.

The perpendicular baseline is 56.2 m, resulting in a large height ambiguity ( $\sim 200$  m), which limits the effects of DEM errors. The advantage of this coseismic interferogram is that the orientation of the LOS-vector with respect to the fault is similar to the case of the synthetic transform fault at  $\theta_{az} = 180^\circ$  (see Chapter 5), for which it has been shown that errors in strike and position have much less influence on the slip distribution compared to surface displacements observed from a LOS-vector more parallel to the fault.

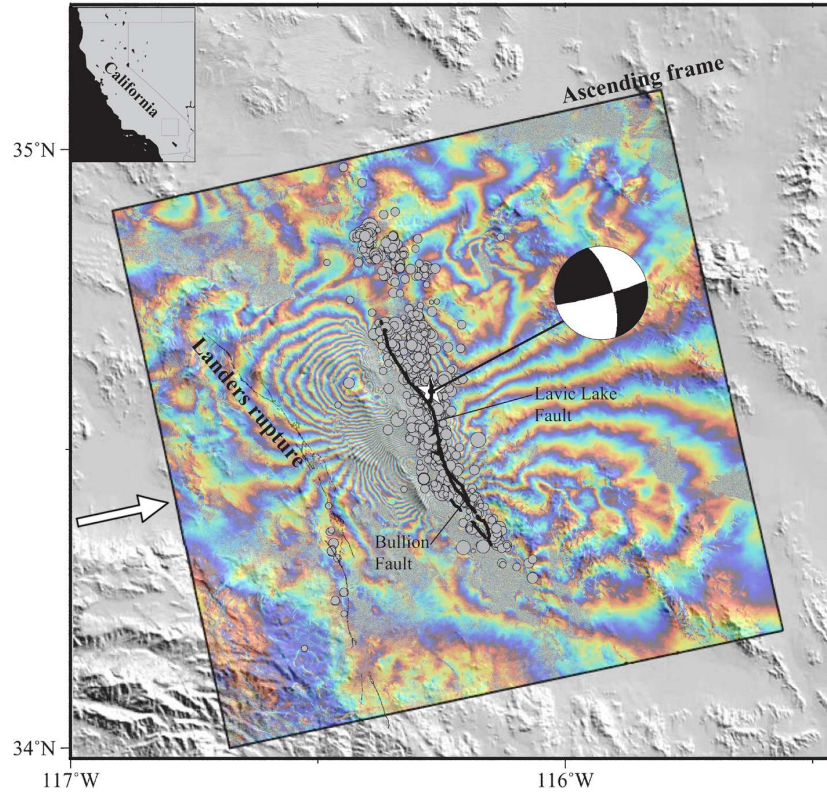


Figure 6.2: Case study area of the 1999 Hector Mine earthquake. The processed ascending SAR image frame is shown as a transparent overlay on a shaded DEM of the study area (adapted from Jónsson (2002)). One color cycle corresponds to 2.83 cm deformation in satellite LOS. The satellite viewing geometry is indicated with the white arrow. The fault trace which has been mapped by the United States Geological Survey (USGS) is shown as a thick line. The epicenter is shown as a white star with the corresponding fault plane solution of the Harvard CMT catalog. Aftershocks that occurred within a month after the earthquake are shown as grey circles. Smaller circles correspond to aftershocks with smaller magnitude.

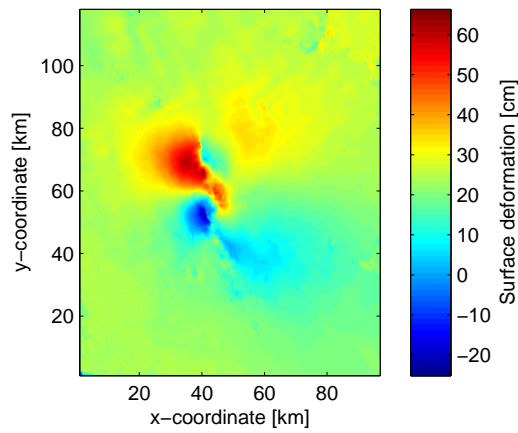


Figure 6.3: Unwrapped ascending interferogram of the Hector Mine earthquake.



## 6.3 Slip distribution estimation

### 6.3.1 Determination of the fault plane geometry

The area around the fault trace is decorrelated, nevertheless an initial guess of the fault strike can be made (Figure 6.4). This can be done either by visual interpretation of the surface deformation pattern, or else by taking into account the location and orientation of the mapped fault trace (Figure 6.2). In a local cartesian coordinate system, the initial strike is set to  $\alpha = 350^\circ$ . The dip and rake are initially set to the values listed in the Harvard CMT catalog:  $\delta = 80^\circ$  and  $r = 174^\circ$ . The position is set to  $(x, y) = (43, 54)$  km from the origin of the interferogram. The length of the fault plane is set to  $L = 50$  km, which is somewhat larger than the length of the mapped fault trace to reduce the chance that the slip distribution is not entirely captured in the inversion. Similarly, the depth extent is chosen to be  $(d_{min}, d_{max}) = (0, 24)$  km. To save computational time, the fault plane is divided into patches of  $2 \times 2$  km. Thus, the slip distribution is composed of 300 individual patches.

### 6.3.2 Smoothness constraint: trade-off between misfit and roughness

As discussed in Section 5.2, for real-world cases it is difficult to determine the optimal smoothness weight. This is due to the fact that:

- the optimal smoothness weight is case-dependent;
- the ‘true’ slip distribution is not known, therefore the deviation from any estimated slip distribution to the true slip distribution cannot be calculated to determine the optimal smoothness weight.

A plot of the misfit  $\varepsilon_m$  between the observations and modeled surface displacements as a function of the smoothness weight  $f_w$  (Figure 6.5) does not seem to be an appropriate

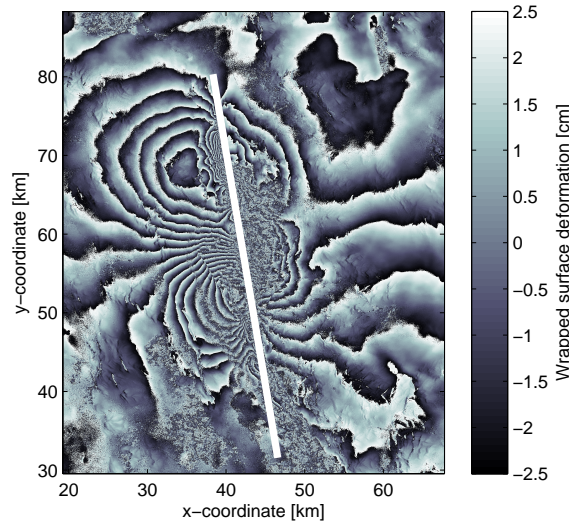


Figure 6.4: Part of the interferogram of the Hector Mine earthquake, zoomed in on the fault trace (wrapped to 5 cm deformation). The decorrelated area around the fault trace is 2-5 km in width. An initial guess of the fault plane geometry (shown as a white line) can be made by looking at the transitions in surface deformation pattern from one side of the fault to the other.



way to visualize the trade-off between the smoothness weight and the misfit. Therefore, the roughness parameter  $R_{sd}$  has been introduced in Section 5.2, which is defined as the mean absolute Laplacian of the estimated slip distribution at a certain smoothness weight. Figure 6.6 shows a plot of the roughness of the slip distribution as a function of the misfit. The plot shows that a smoothness weight between  $f_w = 0.2$  and  $f_w = 0.4$  appears to be optimal, as larger smoothness weights significantly increase the misfit  $\varepsilon_m$  and lower smoothness weights result in rough slip distributions that over-estimate the maximum slip. Although a smoothness weight  $f_w = 0.2$  results in a slip distribution pattern similar to the one estimated with  $f_w = 0.4$ , but with a slightly smaller misfit, the slip distribution estimated with  $f_w = 0.4$  is preferred. This is because the slip on the upper patches of the slip distribution calculated with  $f_w = 0.4$  corresponds better to the surface displacements mapped by the USGS at the fault trace, which are up to 6 m (Salichon et al., 2004). The slip distribution with  $f_w = 0.2$  over-estimates the upper patches with slip up to  $\sim 7.5$  m, while the slip distribution with  $f_w = 0.4$  shows upper patches with slip up to  $\sim 6.5$  m.

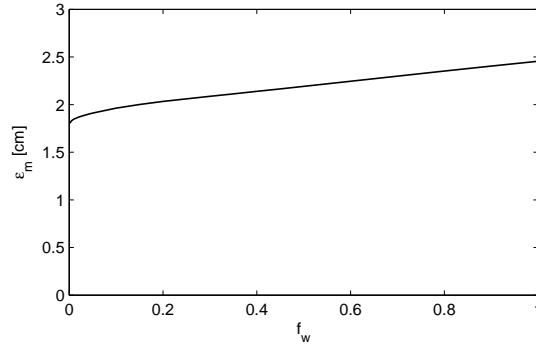


Figure 6.5: Plot of the misfit  $\varepsilon_m$  between the observations and modeled surface displacements as a function of the smoothness weight  $f_w$ .

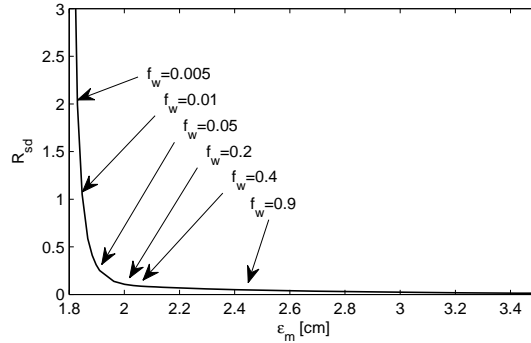


Figure 6.6: Plot of the roughness of the slip distribution  $R_{sd}$  as a function of the misfit  $\varepsilon_m$  between the observations and modeled surface displacements. Some corresponding smoothness weights  $f_w$  are indicated by arrows.

### 6.3.3 Fault plane orientation optimization

The initial fault plane orientation is optimized as follows. As shown in Section 5.3, for the combination of fault plane type and LOS-vector of this interferogram the optimal strike and rake are correlated, i.e. a change in rake shifts the optimal strike and vice versa. The optimal dip is less correlated to the error in strike and rake. These results are verified by optimizing the strike, dip, and rake for different values of the fixed parameters (Figure 6.7). As expected, the optimal strike depends on the error in rake and the optimal rake depends on the error in strike. The optimal dip is not influenced significantly by an error in either strike or rake.

Since it is not possible to optimize all three fault plane orientation parameters independently, the rake is fixed to its initial value. It is thereby assumed that the rake is determined more accurately compared to the initial guess of the strike, which was based on visual interpretation. The Harvard CMT catalog lists the calculated errors in the elements of the moment tensor, of which strike, dip, and rake can be determined. However, computation of the propagation of these moment tensor errors to fault plane orientation errors is a non-trivial procedure and is not considered in this study. See for the mathematical relation between the moment tensor components and the strike, dip, and rake Aki and Richards (1980).

With the rake set to  $r = 174^\circ$ , the optimal strike is found to be  $\alpha = 347^\circ$ , which is only  $3^\circ$  off the initial guess. After the strike is optimized, the dip is optimized in a similar way and found to be  $\delta = 82^\circ$ , which is  $2^\circ$  off the initial guess. Note that the difference in estimated slip distribution is small, see Figure 6.8 and Figure 6.9. However, two improvements in the slip distribution estimated with the optimized set of orientation parameters are a decrease of the number of patches with negative slip and a decrease of maximum slip at the surface, which corresponds better to previous research (Salichon et al., 2004). The modeled surface displacements resulting from the final slip distribution are shown in Figure 6.10.

The slip distributions shown in Figure 6.8 and Figure 6.9 both contain patches with a small amount of negative slip. These patches are mainly deep patches, which contribute less to the surface displacements than more shallow patches. The maximum absolute surface deformation caused by the patches with negative slip is less than 2 cm, which is only about 5% of the maximum absolute surface displacements of the final model. Due to this limited effect of negative slip, it is decided not to use NNLS to estimate the final slip distribution.

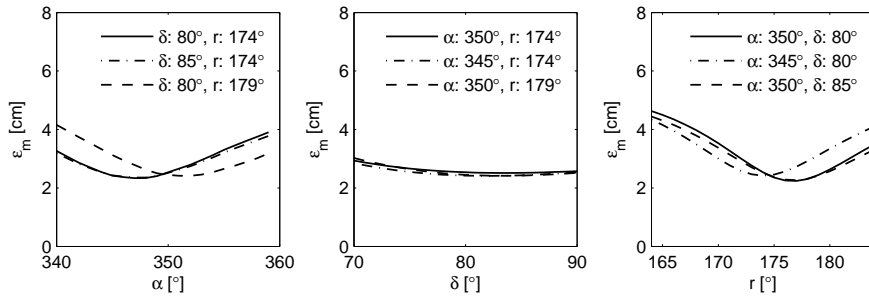


Figure 6.7: Plot of the misfit  $\varepsilon_m$  between the observations and modeled surface displacements as a function of the strike, dip, and rake, each for different values of the two fixed parameters.

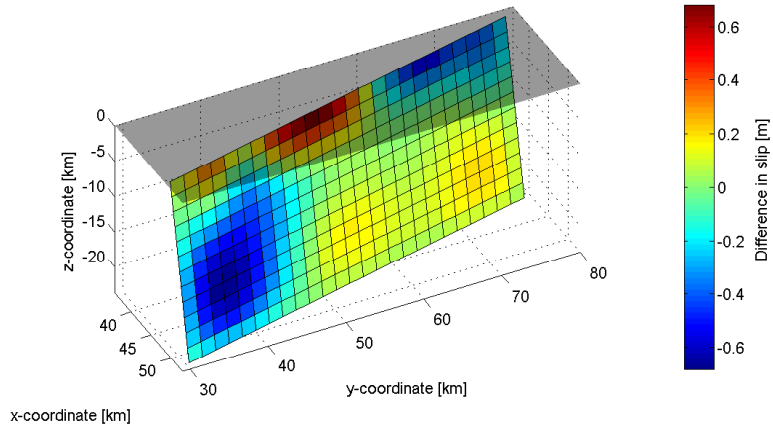


Figure 6.8: Difference in slip between the slip distribution estimated with the initial set of fault plane orientation parameters and the final set of fault plane orientation parameters.

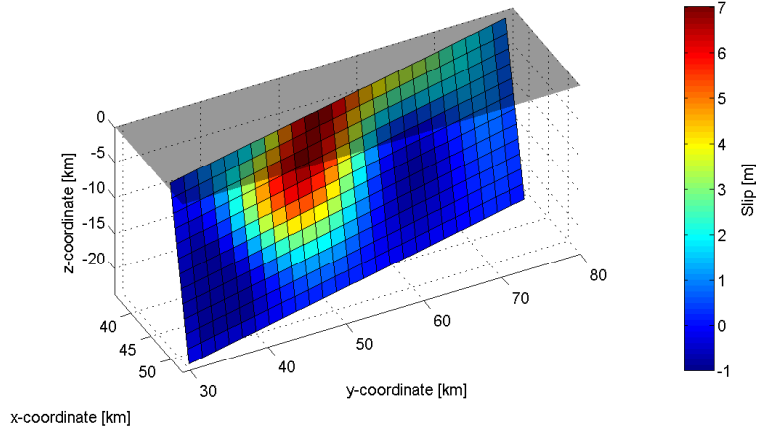


Figure 6.9: Estimated slip distribution for the final strike, dip, and rake.

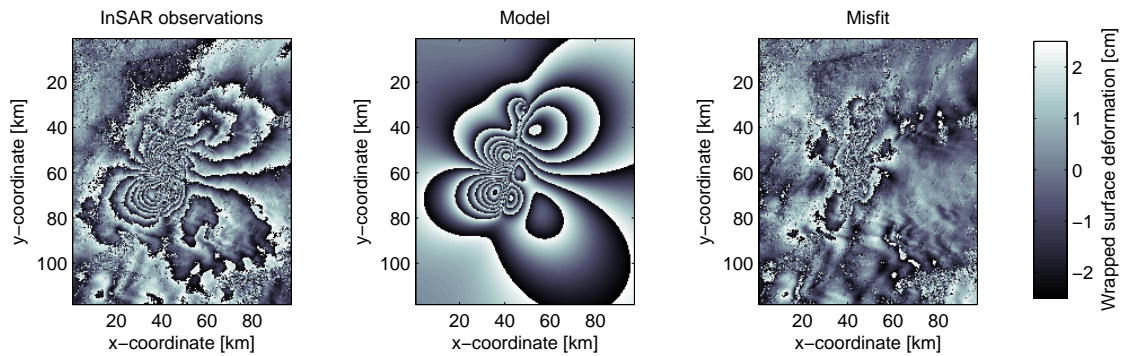


Figure 6.10: InSAR observations, modeled surface displacements, and misfit for the final strike, dip, and rake.

### 6.3.4 Comparison with previous research

A direct comparison between the slip distribution estimated in this study and the results presented elsewhere is difficult, because in most research a joint inversion is applied, either by combining ascending and descending interferograms, or else by combining InSAR data with GPS or seismic data. Exceptions are the work of Jónsson (2002) and Salichon et al. (2004), who presented the results of the inversion of the individual data sets as well.

Figure 6.11 shows the same estimated slip distribution as Figure 6.9, but now with the color of all patches with zero or negative slip clipped to white. This makes it easier to perform a visual comparison between this slip distribution and the results presented by Jónsson (2002). Figure 6.12 shows the slip distribution estimated in his study with the same ascending interferogram using a more complicated fault plane geometry.

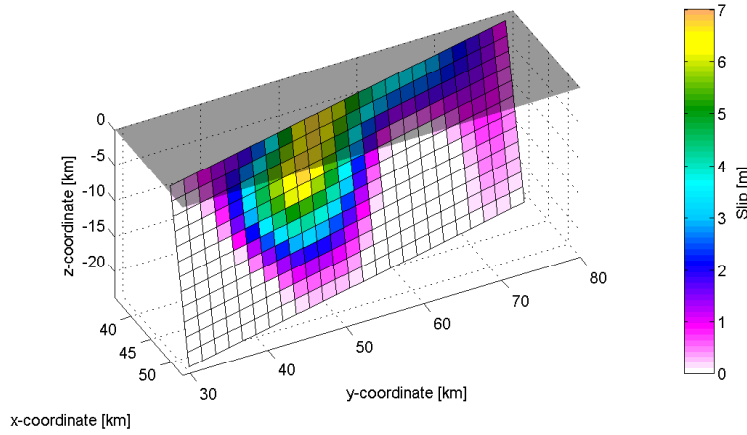


Figure 6.11: Same as Figure 6.9, but now with the color of all patches with zero or negative slip clipped to white and a color scale similar to the one used by Jónsson (2002).

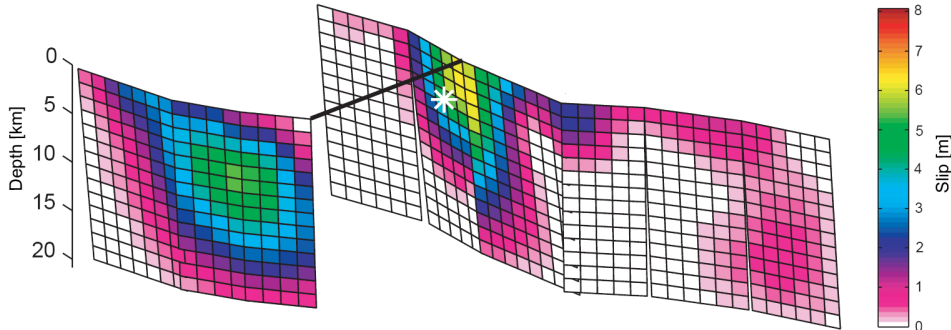


Figure 6.12: Results of the slip inversion performed by Jónsson (2002). The fault plane geometry has been divided into nine segments in a fork structure. The two connected parts of the fork structure are separated by the thick black line for visualization. Each patch is  $1.5 \times 1.5$  km.

The results of this study seem to be in good correspondence with the results presented by Jónsson (2002) in terms of slip distribution pattern and slip amplitude, taking into account that:

- the fault plane geometry in Jónsson’s study is complex, consisting of nine sub-faults with varying strike and dip.
- the patch size used by Jónsson is  $1.5 \times 1.5$  km instead of  $2 \times 2$  km;
- Jónsson used NNLS to solve for the slip distribution instead of conventional LSE.

This suggests that using NNLS and modeling a complex fault-plane geometry is not always necessary to obtain a reasonable estimate for the slip distribution.

The slip distribution estimation presented by Salichon et al. (2004) shows a similar maximum slip as the slip distribution presented here. Furthermore, the locations of the maximum slip in of both studies correspond well. Salichon et al. (2004) inverted for the slip direction as well, which shows to be predominantly in one direction. This is in accordance with the assumption of a uniform rake.

When ignoring patches with negative slip (integrating the slip only on those patches that have non-negative slip), the seismic moment for the final slip distribution is  $M_0 = 5.7 \cdot 10^{19}$  Nm. Without ignoring patches with negative slip (integrating the slip on all patches), the seismic moment is slightly smaller due to a decrease in average slip on the fault plane as a consequence of negative slip. However, for the computation of the moment magnitude this difference is negligible since both estimates for the seismic moment result in a moment magnitude of  $M_W = 7.1$ , which is in accordance with the moment magnitude listed by the Harvard CMT catalog and the moment magnitude calculated by Jónsson (2002), Salichon et al. (2004), and Ji et al. (2002).

## 6.4 Influence of applied data reduction technique

All previous results presented in this study have been obtained by applying uniform re-sampling as a data reduction technique, with a resampled pixel size of  $500 \times 500$  m. Since the degree and method of data reduction is a case-dependent trade-off between acceptable information loss, noise reduction, and available computational time, it is interesting to investigate the influence of the choice of data reduction on the estimated slip distribution. The two data reduction techniques considered here – uniform resampling and quad-tree partitioning – have been described in Section 4.2.2.

### 6.4.1 Results with uniform resampling

The inversion is performed with the InSAR observations resampled to five different resolutions: 300 m, 500 m, 640 m (multi-looked  $32 \times 32$  for comparison with quad-tree partitioning), 1 km, and 2 km. A better resolution than 300 m for a full InSAR frame resulted in computer memory problems (for a computer with 2 GB internal memory), and is therefore not considered. A resolution of 2 km results already in significant information loss (Figure 6.13), more coarse resolutions are therefore also excluded from the tests. The slip distributions estimated for these five cases are given in Appendix B.

The number of data points at each resolution and a rough indication of the computational time are given in Table 6.1. An increase in resolution from 500 m to 300 m shows no large improvement in slip distribution, except for a further decrease in significance of negative slip, at the cost of roughly four times the computational time. A decrease in

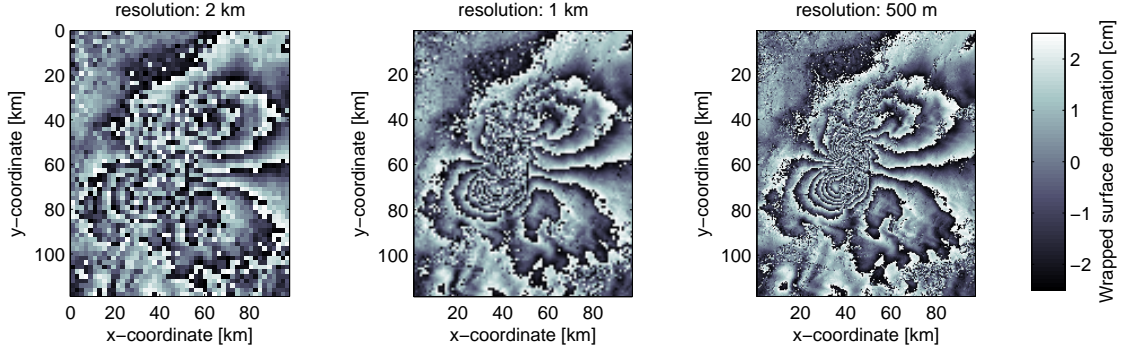


Figure 6.13: InSAR observations after uniform resampling at different resolutions: 2 km, 1 km, and 500 m.

resolution to 640 m has negligible effect on the estimated slip distribution. Decreasing the resolution to 1 km or 2 km results in an increase in significance of negative slip, and a slight increase of overall misfit. However, the slip distribution pattern and the location and magnitude of maximum slip are similar to the results at a resolution of 500 m and 300 m, although the roughness of the slip distribution increases. Therefore, it can be concluded that the uniform resampling resolution does not seem to have a large influence, as long as the resolution is within acceptable bounds. These bounds depend on the scale of the earthquake. Further research on this topic could focus on the determination of optimal resolution as a function of the dimensions of the fault plane, thereby taking into account computational time and information detail.

#### 6.4.2 Results with quad-tree partitioning

To implement quad-tree partitioning a small trick needs to be applied, since the algorithm described in Section 4.2.2 only works on images with dimensions that are a power of 2, 3, ..., and so on. Reducing an original interferogram to dimensions that fulfill this criterion would result in a significant loss of data, and is therefore not an option. Another possibility is to extend the original interferogram with parts containing no information (zeros) to obtain an interferogram that has dimensions which are a power of, for instance, 2. However, this often results in a large amount of additional useless data to perform quad-tree partitioning on, which is too computationally expensive. Therefore, an alternative method is proposed to divide the original interferogram in smaller blocks with dimensions  $q_{max}$ , which are a power of 2 (for example, blocks of  $128 \times 128$  pixels or  $256 \times 256$  pixels) and perform quad-tree partitioning on each of these blocks individually. After all blocks have been partitioned in segments according to the specified threshold (which is the maximum allowed displacement difference within one block), the trees containing the structure of the segments in all blocks are merged together. Of each segment, the new observation is the average of the original individual observations within that segment. A minimum number of pixels to be merged  $q_{min}$  can be specified to reduce noise.

The proposed quad-tree partitioning method is found to be efficient both in terms of computational time and data reduction. The thresholds  $q_t$  that have been tested and their corresponding number of data points are given in Table 6.1. Three examples of InSAR observations after quad-tree partitioning for different quad-tree thresholds  $q_t$  with  $q_{min} = 32$  pixels (640 m resolution) are shown in Figure 6.14. All slip distribution estimations for the different quad-tree thresholds and minimum block size are given in Appendix B.

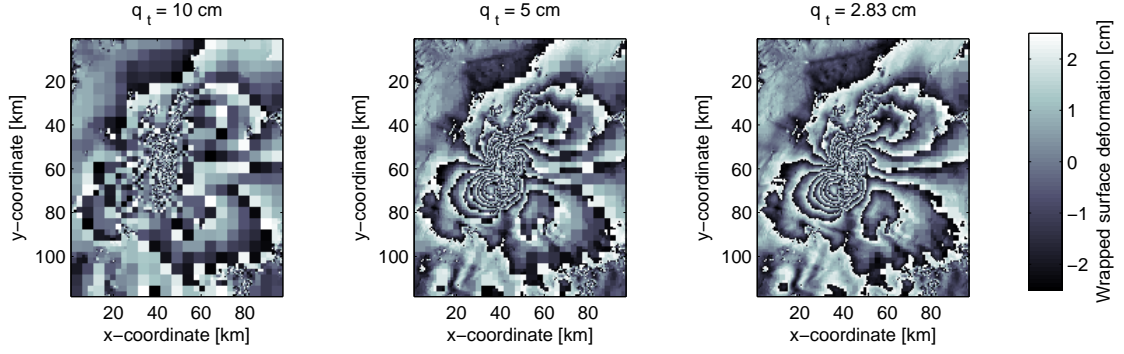


Figure 6.14: InSAR observations after quad-tree partitioning for different quad-tree thresholds  $q_t$  with  $q_{min} = 32$  pixels (640 m).

Table 6.1: Tested data reduction cases. The minimum and maximum segment dimensions  $q_{min}$  and  $q_{max}$  are specified in meters and correspond to the resampling resolution for uniform resampling. The time indication is a rough estimate of the computational time, relative to the case of uniform resampling with a pixel size of  $500 \times 500$  m. The time required to complete the inversion at this resolution is about 4-7 minutes for a computer with 2 GB internal memory and a dual-core processor.

	$q_{min}$ [m]	$q_{max}$ [m]	$q_t$ [cm]	Data points	Time [%]
UR	300	300	0	128444	400
	500	500	0	46020	100
	640	640	0	28120	70
	1000	1000	0	11349	30
	2000	2000	0	2784	10
QT	160	5120	28.3	563	5
	160	5120	10	5285	15
	160	5120	5	64316	150
	160	5120	2.83	178139	700
	640	5120	28.3	560	5
	640	5120	10	2969	10
	640	5120	5	12674	30
	640	5120	2.83	20618	50

An important observation is that the results with  $q_t = 2.83$  cm and  $q_{min} = 32$  pixels (640 m) are similar to the results with uniform resampling at a resolution of 500 m and 640 m, but the number of observations using quad-tree partitioning is roughly half or two-thirds of the number of observations used with uniform resampling at a resolution of 500 m and 640 m, respectively. This is a significant improvement in efficiency. However, the result of the inversion appears to be influenced by both  $q_{min}$  and  $q_t$ . The threshold  $q_t$  determines the maximum difference in surface displacements that is allowed in a block before it is split in four segments. The lower this threshold, the more information is preserved after data reduction.

The total number of observations is not only determined by the quad-tree threshold, but also by  $q_{min}$ , which specifies the minimum number of pixels that should be merged prior to partitioning. In other words, it determines the resolution after initial uniform resampling, before the actual quad-tree partitioning is performed. Without applying uni-

form resampling prior to quad-tree partitioning, noise is preserved if its spatial variation exceeds the threshold  $q_t$ . The results of the inversion with  $q_{min}$  set to 32 pixels (640 m) are found to differ less for different thresholds than the same results with  $q_{min}$  set to 8 pixels (160 m). This is probably due to less reduction of noise in the latter case. More research needs to be done on the trade-off between noise reduction and information loss, as this is shown to be important when using quad-tree partitioning as a data reduction technique.

A threshold of one fringe in the original interferogram (2.83 cm) with a minimum number of 32 pixels to be merged is adequate to obtain a reasonable slip distribution, which is comparable to the same results obtained with uniformly resampled observations at a resolution of 500 m. The advantage of quad-tree partitioning is that a much smaller number of observations is required compared to uniformly resampled observations, which is a significant improvement of efficiency in terms of computational time and memory requirements.

## 6.5 Summary and concluding remarks

### 6.5.1 Hector Mine slip distribution inversion

This chapter showed the results of a case study on the Hector Mine earthquake, which occurred in California on October 16, 1999. The selected InSAR data consisted of two ascending ERS-2 frames that were processed to a coseismic interferogram. After an initial guess of the fault plane geometry, which was determined from the combination of visual inspection of the interferogram and seismic data from the Harvard CMT catalog, the fault plane orientation was optimized by varying the strike, dip, and rake independently to search for a minimum in misfit between the observations and the modeled surface displacements. The results from Chapter 5 that suggested a dependency between the optimal strike and the optimal rake have been verified: optimization of both parameters independently is not possible. The optimal dip showed almost no correlation with the strike and rake, and was therefore optimized independently.

The slip distributions estimated for both the initial fault plane geometry and the final fault plane geometry show no significant differences; only a slight improvement in maximum slip and a decrease of the significance of negative slip is observed. The patches of negative slip in the final model show negligible surface deformation. Therefore, a three-step inversion with NNLS is not considered.

The estimated slip distribution has a moment magnitude of  $M_W = 7.1$ , which is in accordance with previous research and the moment magnitude estimates from seismic data. Furthermore, the slip distribution pattern and amplitude is similar to the results obtained by Jónsson (2002), who modeled a much more complicated fault plane geometry. Considering this difference in fault plane geometry, the results are in good correspondence in terms of slip distribution pattern and magnitude, which suggests that using NNLS and modeling a complex fault-plane geometry is not always necessary to obtain a reasonable estimate for the slip distribution.

### 6.5.2 Influence of different methods and degrees of data reduction

Two data reduction techniques have been compared: uniform resampling and quad-tree partitioning, which have been explained in Chapter 4. The slip distribution of the Hector Mine earthquake has been inverted for five different uniform resampling resolutions. Furthermore, the inversion is applied with four different quad-tree thresholds, each with two different minimum segment sizes that determine the minimum number of observations to



merge. It has been found that the slip distribution estimation is sensitive to the spatial distribution of the observations, but not to the number of observations. Furthermore, it has been shown that the results obtained with quad-tree partitioning with a threshold of 1 fringe in the original interferogram (2.83 cm) and a minimum number of 32 observations to merge are almost identical to those obtained with uniform resampling at a resolution of 500 m or 640 m, but with a much smaller number of observations. Thus, if the threshold and minimum number of observations to merge are chosen such that detail is preserved while at the same time noise is reduced, an increase in efficiency in terms of computational time and memory requirements can be achieved by using quad-tree partitioning.



## Chapter 7

# Conclusions and recommendations

This thesis focused on the inversion of earthquake slip distributions using InSAR data. The result of such an inversion depends on the assumptions made in the inverse model and on the observations. Therefore, the sensitivity of the slip distribution to errors in fault plane geometry and atmospheric errors in observations has been investigated. Furthermore, slip distribution estimations have been compared for different methods and degrees of data reduction. The conclusions of this work are presented in Section 7.1, structured according to the research objectives that were defined in the introduction.

During the research, various issues have been encountered that need attention in future research on this topic. These recommendations are discussed in Section 7.2.

### 7.1 Conclusions

In the introduction three research objectives have been defined:

1. Investigate the sensitivity of the slip distribution to errors in fault plane geometry.
2. Investigate the sensitivity of the slip distribution to errors in observations due to spatial and temporal variations in atmospheric delay.
3. Investigate the sensitivity of the slip distribution to the number and spatial distribution of the observations.

The conclusions of these research objectives are presented in the following sections.

#### 7.1.1 Sensitivity to errors in fault plane geometry

In general, the sensitivity of the slip distribution estimation to errors in fault plane geometry depends on the surface deformation field in the satellite LOS. The results of the tests with the synthetic interferograms show that it can be deduced based on information about the earthquake type and the satellite LOS to which fault plane geometry parameters the sensitivity of the slip distribution is largest. Since the earthquake type and satellite LOS are generally known prior to the actual inversion procedure, deducing the parameters to which the slip distribution is sensitive can be used to:

- facilitate the choice of InSAR data;
- prioritize the optimization of certain parameters over others.

The observed surface displacement field depends on the earthquake type, the fault plane geometry, the magnitude of the earthquake, and the satellite characteristics (LOS and wavelength). Generally, the sensitivity to errors in strike and position increases if the difference in surface deformation between one side of the fault and the other side of the fault increases in satellite LOS. For example, this can be due to differences in:

- earthquake type: a normal fault or reverse fault compared to a transform fault;
- earthquake magnitude: an earthquake with  $M_W = 7.5$  compared to an earthquake with  $M_W = 5.5$ ;
- satellite azimuth angle: parallel to the fault plane compared to perpendicular to the fault plane in case of a transform fault;
- satellite incidence angle:  $\theta_i = 55^\circ$  compared to  $\theta_i = 23^\circ$  for a transform fault or vice versa for a normal fault or reverse fault.

Similarly, the influence of an error in rake decreases if the overall surface deformation field increases.

### 7.1.2 Sensitivity to atmospheric errors in observations

The sensitivity of the slip distribution to errors in observations due to spatial and temporal variations in atmospheric delay depends on the amplitude of the surface deformation field compared to the amplitude of these atmospheric errors. For large earthquakes such as the earthquakes examined in this study, the effect of atmospheric delay on the slip distribution is negligible under normal weather conditions.

### 7.1.3 Sensitivity to the number and spatial distribution of observations

The slip distribution of the 1999 Hector Mine earthquake has been estimated using two data reduction techniques for the InSAR data: uniform resampling and quad-tree partitioning. Different degrees of uniform resampling showed no significant change in slip distribution, as long as the resolution after uniform resampling is reasonable, which depends on the scale of the earthquake. The slip distribution estimation is thus not sensitive to the number of observations.

For inversions performed with quad-tree partitioned data, the sensitivity of the slip distribution to the choice of different quad-tree thresholds is larger if less pixels are resampled prior to quad-tree partitioning, due to the fact that less noise is reduced. Thus, the slip distribution estimation is found to be sensitive to the distribution of observations, in particular when only a small number of observations is used in the inversion. However, if the threshold and minimum number of observations to merge is chosen such that detail is preserved while at the same time noise is reduced, an increase in efficiency in terms of computational time and memory requirements can be achieved by using quad-tree partitioning as a data reduction technique.

## 7.2 Recommendations

### 7.2.1 Smoothness constraint: an alternative approach

An important issue of debate in the proposed inversion procedure is the smoothness constraint. Both in previous research (e.g. Jónsson (2002), Wright et al. (2003)) and in this study a discrete Laplacian smoothness operator is used to constrain the slip distribution. This mathematical ‘trick’ is necessary to obtain a unique slip distribution and to stabilize the solution. However, the main problem with this smoothness constraint is that its relative weight (compared to the observations) is case-dependent and chosen by the user. It is therefore not an objective approach. A potential approach to solve the non-uniqueness and instability of the slip distribution makes use of Bayesian probability theory (see for example Koch (1999)), in which an a-priori variance-covariance matrix  $Q_{pp}$  of the slip distribution is used. This variance-covariance matrix acts as a-priori information to steer the solution in a certain direction. The solution using  $Q_{pp}$  equals the solution given in Equation (4.12) if one substitutes  $Q_{pp} = \nabla^T Q_{\nabla}^{-1} \nabla$ . The method of pseudo observations can thus also be seen from a Bayesian probability perspective, where the smoothness weight of the slip distribution is a-priori information: the slip distribution is assumed to be smooth to a certain degree before it is actually estimated.

The challenge lies in defining a realistic  $Q_{pp}$ . However, if  $Q_{pp}$  can be defined on a physical basis (i.e. based on a physical quantity that can be measured), the subjectivity problem associated with the smoothness weight  $f_w$  is solved. One possible way of defining  $Q_{pp}$  is to build the variance-covariance matrix based on a distance-correlation function. This function ‘fills’ entries in the variance-covariance matrix with a large positive covariance if the patches corresponding to these entries have a small Euclidean distance. In other words, patches on a fault plane that are far away from each other are less correlated than patches that are located near to each other. The covariance as a function of distance can be defined as:

$$C(p_1, p_2) = w \cdot e^{-\frac{1}{C_l} \text{dist}(p_1, p_2)}, \quad (7.1)$$

where  $C(p_1, p_2)$  is the covariance of patch  $p_1$  and patch  $p_2$ ,  $w$  is the weight assigned to the distance-correlation function,  $C_l$  is the correlation length determining how fast the correlation deteriorates with length, and  $\text{dist}(p_1, p_2)$  is the Euclidean distance between patch  $p_1$  and patch  $p_2$ .

Future research should explore the ways to determine a reliable function to build an a-priori variance-covariance matrix (possibly with the proposed distance-correlation function), since it can potentially solve the subjectivity issues that are currently associated with the widely used Laplacian smoothness method.

### 7.2.2 Optimal data reduction

By now, InSAR has proven to be a powerful tool for many applications in a variety of study and working fields. The popularity of InSAR as a space-borne Earth observation technique has contributed to the development of new satellites that keep on improving in terms of for example spatial resolution, repeat-time, and accuracy. This development increases the need for advanced data reduction techniques, such as quad-tree partitioning. For both uniform resampling and quad-tree partitioning, guidelines need to be developed to determine the optimal method and amount of data reduction, given a certain scene and data set. For example, for uniform resampling a possible approach is to define a relation between the dimensions of the fault plane and the minimum and maximum acceptable resolution, thereby taking into account both information loss and noise reduction. For

quad-tree partitioning, the minimum number of pixels to be merged prior to partitioning should be determined in a similar way. The threshold could for instance be determined as a function of the radar wavelength.

Other research on this topic could focus on the development of other variable resolution resampling techniques.

### 7.2.3 General resolvability of slip distributions

Three main earthquake types have been used to study the sensitivity of the slip distribution estimation to errors in fault plane geometry and observations. Clear differences between these three earthquake types in terms of resolvability of the slip distribution have not been observed, other than those that can be subscribed to relative differences in smoothness weight. However, it is expected that the general resolvability of earthquake slip distributions is to some extent influenced by the type of earthquake and the satellite LOS. More specific, in theory it is possible that from a certain satellite LOS almost no surface deformation can be observed. This is the case if the satellite LOS is exactly perpendicular to the fault plane and the direction of movement. It is not yet investigated if there is a clear relation between the resolvability of the slip distribution and the satellite LOS relative to the fault plane geometry and earthquake type. A possible method to explore this issue is to assume that the fault plane geometry parameters and the smoothness weight are random variables, each with a certain probability density function. The slip distribution can be estimated for many sets of fault plane geometry realizations. Subsequently, the RMSE of the slip distribution can be determined for each realization of the fault plane geometry. The RMSE of the slip distribution will have a certain probability density function with a mean and variance. Suppose one runs this simulation for several LOS-vectors and for several earthquake types, differences in the statistics of the RMSE of the slip distribution can then be used to examine the differences in general resolvability of the slip distribution. For example, if from a certain satellite LOS the mean of the RMSE of the slip distribution of an earthquake is larger than the mean of the RMSE of the slip distribution for the same earthquake, but viewed from another satellite LOS, this suggests that the slip distribution can be resolved better for the latter satellite LOS.

### 7.2.4 Other improvements and additions to this study

The results of this research show that the relative sensitivity of different parameters can be deduced based on information about the earthquake and satellite characteristics. However, only one slip distribution is investigated. The results of this work need to be verified for completely different slip distributions and fault planes consisting of multiple sub-faults as well.

Furthermore, more research needs to be done on the effect of atmospheric signals on slip distributions estimated for earthquakes of smaller magnitudes than the earthquakes considered in this study, under a variety of weather conditions. The results presented here can serve as a basis for future work on this topic.

# References

- Aki, K. and Richards, P. G., 1980, *Quantitative seismology: theory and methods*, WH Freeman, New York. 932 pp.
- ALOS, 2008. Advanced Land Observing Satellite, <http://www.eorc.jaxa.jp/ALOS/>.
- Arikan, M. and Hanssen, R. F., 2008, *Structural deformation of the High-Speed Line (HSL) infrastructure in the Netherlands: observations using satellite radar interferometry*, 13<sup>th</sup> FIG International Symposium on Deformation Measurements and Analysis, Lisbon, Portugal, 12–15 May, 2008, Vol. 1.
- Bamler, R. and Hartl, P., 1998, *Synthetic aperture radar interferometry*, Inverse Problems, Vol. 14, R1–R54.
- Chen, C. W. and Zebker, H. A., 2000, *Two-dimensional phase unwrapping using statistical models for cost functions in nonlinear optimization*, Journal of the Optical Society of America A., Vol. 18, 338–351.
- Curlander, J. C. and McDonough, R. N., 1991, *Synthetic aperture radar: systems and signal processing*, John Wiley & Sons, Inc, New York.
- Du, Y., Aydin, A. and Segall, P., 1992, *Comparison of various inversion techniques as applied to the determination of a geophysical deformation model for the 1983 Borah Peak earthquake*, Bulletin of the Seismological Society of America, Vol. 82, No. 4, 1840–1866.
- Fialko, Y., Simons, M. and Agnew, D., 2001, *The complete (3-D) surface displacement field in the epicentral area of the 1999 Mw=7.1 Hector Mine earthquake, California, from space geodetic observations*, Geophysical Research Letters, Vol. 28, No. 16, 3063–3066.
- Fowler, C. M. R., 1990, *The solid Earth: an introduction to global geophysics*, first edn, Cambridge University Press. 472 pp.
- Goldstein, R. M. and Werner, C. L., 1998, *Radar interferogram filtering for geophysical applications*, Geophysical Research Letters, Vol. 25, No. 21, 4035–4038.
- Hanks, T. C. and Kanamori, H., 1979, *A moment magnitude scale*, Journal of Geophysical Research, Vol. 84, 2348–2350.
- Hanssen, R. F., 2001, *Radar interferometry: data interpretation and error analysis*, Kluwer Academic Publishers, Dordrecht, The Netherlands.
- Hernandez, B., Cotton, F., Campillo, M. and Massonnet, D., 1997, *A comparison between short term (co-seismic) and long term (one year) slip for the Landers earthquake: Measurements from strong motion and SAR interferometry*, Geophysical Research Letters, Vol. 24, No. 13, 1579–1582.

- Ji, C., Wald, D. J. and Helmberger, D. V., 2002, *Source description of the 1999 Hector Mine, California, earthquake, part II: complexity of slip history*, Bulletin of the Seismological Society of America, Vol. 92, No. 4, 1208–1226.
- Jónsson, S., 2002, *Modeling of volcano and earthquake deformation from satellite radar interferometric observations*, PhD thesis, Stanford University.
- Kampes, B. and Usai, S., 1999, *Doris: the Delft Object-oriented Radar Interferometric Software*, 2nd International Symposium on Operationalization of Remote Sensing, Enschede, The Netherlands, 16–20 August, 1999, Vol. 1.
- Kaverina, A., Dreger, D. and Price, E., 2002, *The combined inversion of seismic and geodetic data for the source process of the 16 October 1999 Mw=7.1 Hector Mine, California, earthquake*, Bulletin of the Seismological Society of America, Vol. 92, No. 4, 1266–1280.
- Koch, K.-R., 1999, *Parameter estimation and hypothesis testing in linear models*, 2 edn, Springer-Verlag, New York.
- Lawson, C. L. and Hanson, R. J., 1974, *Solving Least-Squares problems*, Prentice Hall, Englewood Cliffs, New Jersey. 340 pp.
- Marshak, S., 2001, *Earth: portrait of a planet*, first edn, Norton & Company. 733 pp.
- Massonnet, D. and Feigl, K. L., 1998, *Radar interferometry and its application to changes in the Earth's surface*, Reviews of Geophysics, Vol. 36, No. 4, 441–500.
- Massonnet, D., Rossi, M., Carmona, C., Adagna, F., Peltzer, G., Feigl, K. and Rabaute, T., 1993, *The displacement field of the Landers earthquake mapped by radar interferometry*, Nature, Vol. 364, No. 8, 138–142.
- Michel, R., Avouac, J.-P. and Taboury, J., 1999, *Measuring ground displacement from SAR amplitude images: application to the Landers earthquake*, Geophysical Research Letters, Vol. 26, No. 7, 875–878.
- Motagh, M., Klotz, J., Tavakoli, F., Djamour, Y., Arabi, S., Wetzell, H.-U. and Zschau, J., 2006, *Combination of precise leveling and InSAR data to constrain source parameters of the Mw=6.5, 26 December 2003 Bam earthquake*, Pure and Applied Geophysics, Vol. 163, 1–18.
- Okada, Y., 1985, *Surface deformation due to shear and tensile faults in a half-space*, Bulletin of the Seismological Society of America, Vol. 75, No. 4, 1135–1154.
- Pedersen, R., Jónsson, S., Árnadóttir, T., Sigmundsson, F. and Feigl, K. L., 2003, *Fault slip distribution of two June 2000 Mw=6.5 earthquakes in South Iceland estimated from joint inversion of InSAR and GPS measurements*, Earth and Planetary Science Letters, Vol. 213, 487–502.
- RADARSAT-2, 2008. <http://www.radarsat2.info/about/mission.asp>.
- Salichon, J., Lundgren, P., Delouis, B. and Giardini, D., 2004, *Slip history of the 16 October 1999 Mw=7.1 Hector Mine earthquake (California) from the inversion of InSAR, GPS, and teleseismic data*, Bulletin of the Seismological Society of America, Vol. 94, No. 6, 2015–2027.



- Sauber, J., Thatcher, W. and Solomon, S. C., 1986, *Geodetic measurement of deformation in the central Mojave Desert, California*, Journal of Geophysical Research, Vol. 91, 2683–2693.
- Seeber, G., 2003, *Satellite geodesy*, second edn, De Gruyter, Berlin, Germany. 589 pp.
- Sigmundsson, F., 2008. Personal communication. Subject: expected maximum error ranges in fault plane solutions obtained from seismic data.
- Simons, M., Fialko, Y. and Rivera, L., 2002, *Coseismic deformation from the 1999 Mw=7.1 Hector Mine, California, earthquake as inferred from InSAR and GPS observations*, Bulletin of the Seismological Society of America, Vol. 92, No. 4, 1390–1402.
- Tarantola, A., 2005, *Inverse problems theory and methods for model parameter estimation*, SIAM, Philadelphia. 342 pp.
- TerraSAR-X, 2008. Infoterra, EADS Astrium, <http://www.infoterra.de>.
- van Zwieten, G., 2008. DeformTool, Delft University of Technology.
- Vanicek, P., Castle, R. O. and Balazs, E. I., 1980, *Geodetic leveling and its applications*, Reviews of Geophysics, Vol. 18, No. 2, 505–524.
- Villasenor, J. and Zebker, H. A., 1992, *Temporal decorrelation in repeat-pass radar interferometry*, igarss92, Vol. 2, 941–943.
- Welstead, S. T., 1999, *Fractal and wavelet image compression techniques*, SPIE Optical Engineering Press, Bellingham, WA. 232 pp.
- Wright, T. J., Lu, Z. and Wicks, C., 2003, *Source model for the Mw=6.7, 23 October 2002, Nenana Mountain earthquake (Alaska) from InSAR*, Geophysical Research Letters, Vol. 30, No. 18, 12/1–12/4.
- Wright, T., Parsons, B. E., Jackson, J. A., Haynes, M., Fielding, E. J., England, P. C. and Clarke, P. J., 1999, *Source parameters of the 1 October 1995 Dinar (Turkey) earthquake from SAR interferometry and seismic bodywave modelling*, Earth and Planetary Science Letters, Vol. 172, 23–37.



## Appendix A

### Selection of inversion results for the synthetic transform fault

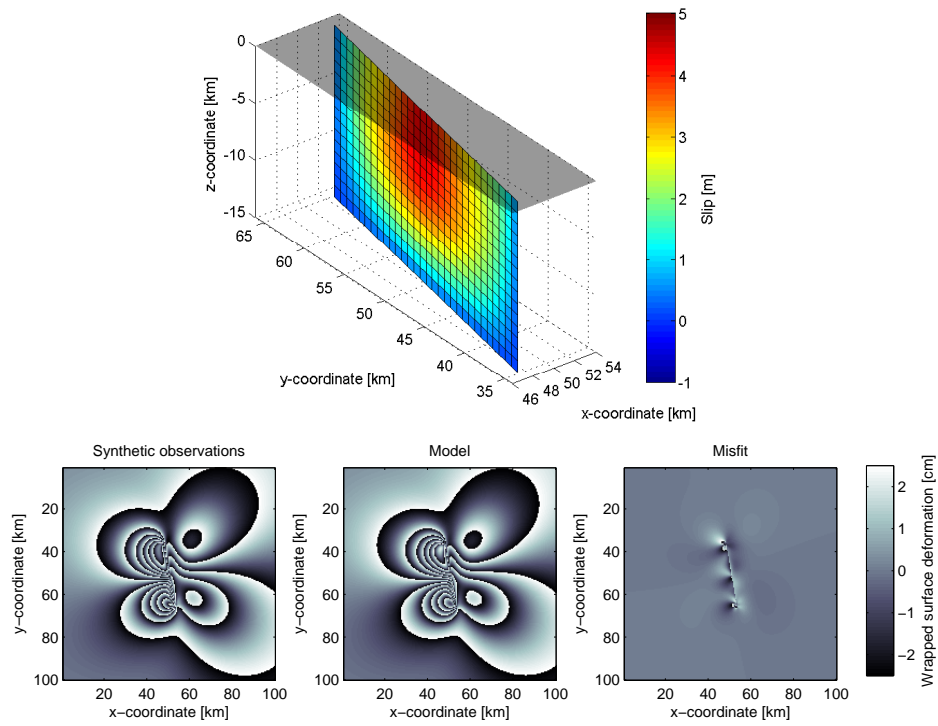


Figure A.1: Slip distribution and surface displacements estimated for the transform fault at  $\theta_{az} = 180^\circ$  with the correct fault plane geometry.

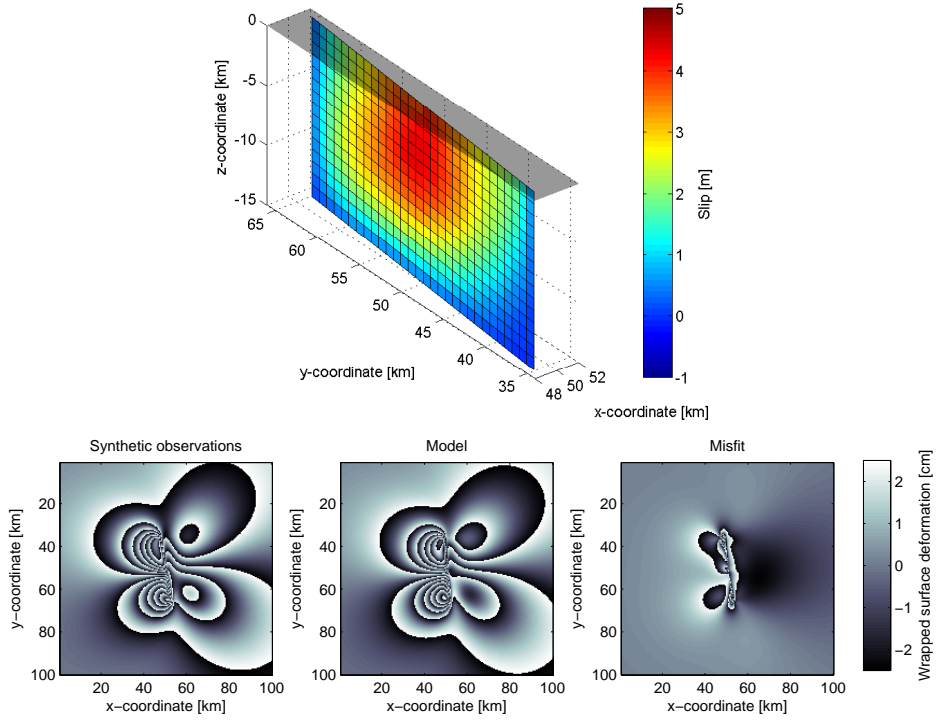


Figure A.2: Slip distribution and surface displacements estimated for the transform fault at  $\theta_{az} = 180^\circ$  with  $\Delta\alpha = -5^\circ$ .

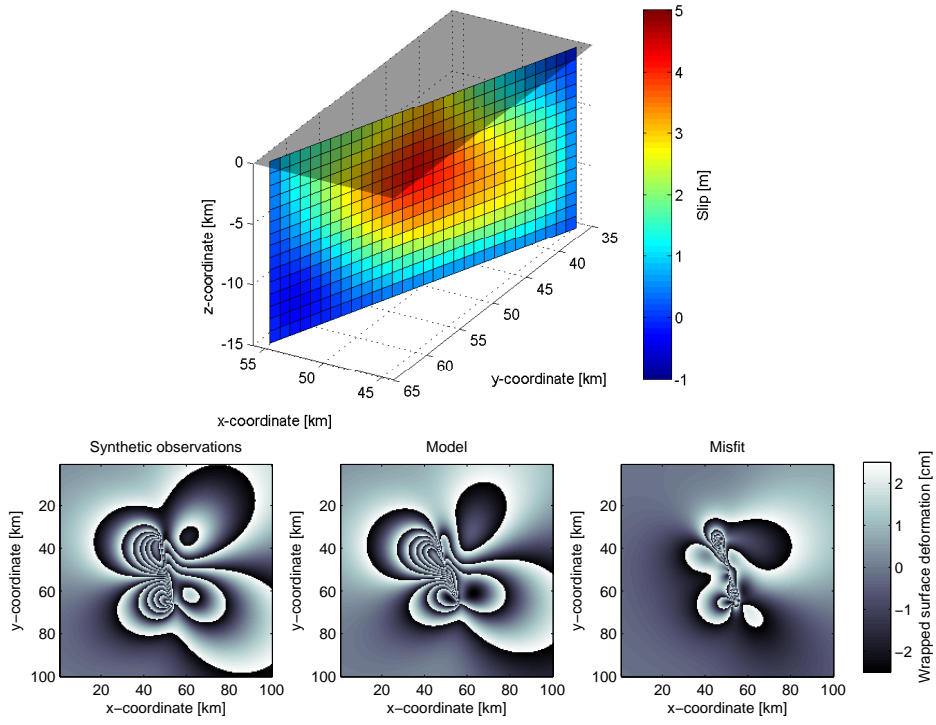


Figure A.3: Slip distribution and surface displacements estimated for the transform fault at  $\theta_{az} = 180^\circ$  with  $\Delta\alpha = 10^\circ$ .

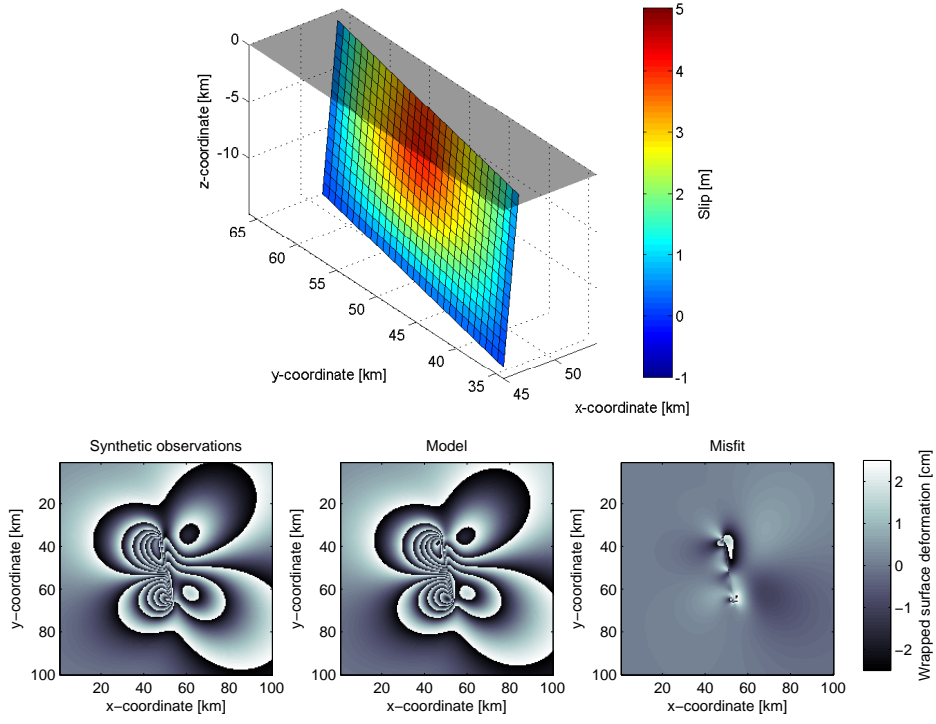


Figure A.4: Slip distribution and surface displacements estimated for the transform fault at  $\theta_{az} = 180^\circ$  with  $\Delta\delta = -5^\circ$ .

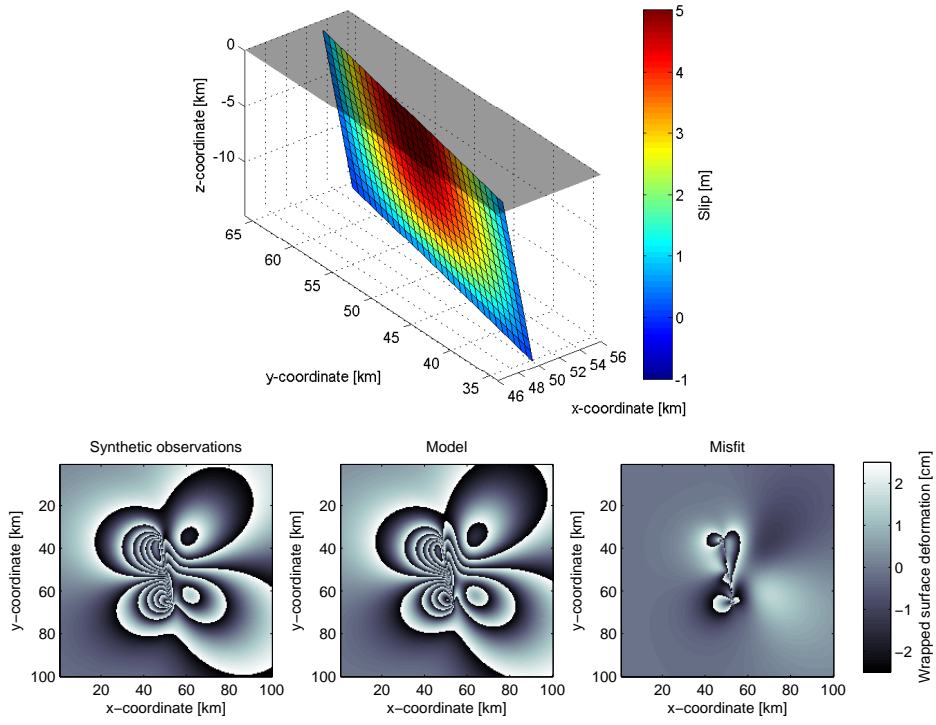


Figure A.5: Slip distribution and surface displacements estimated for the transform fault at  $\theta_{az} = 180^\circ$  with  $\Delta\delta = 10^\circ$ .

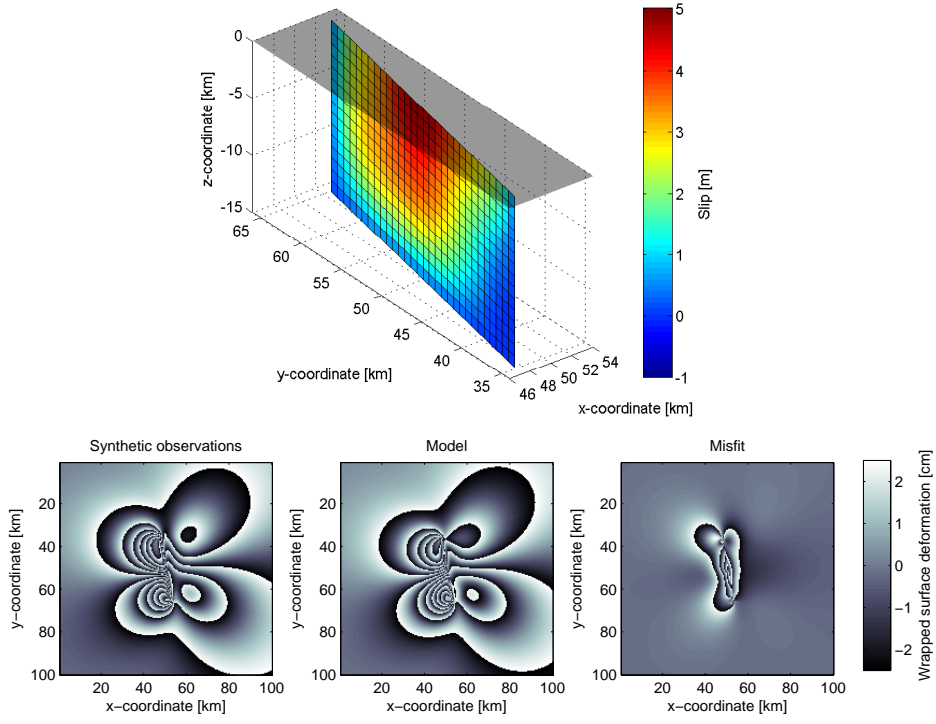


Figure A.6: Slip distribution and surface displacements estimated for the transform fault at  $\theta_{az} = 180^\circ$  with  $\Delta r = -5^\circ$ .

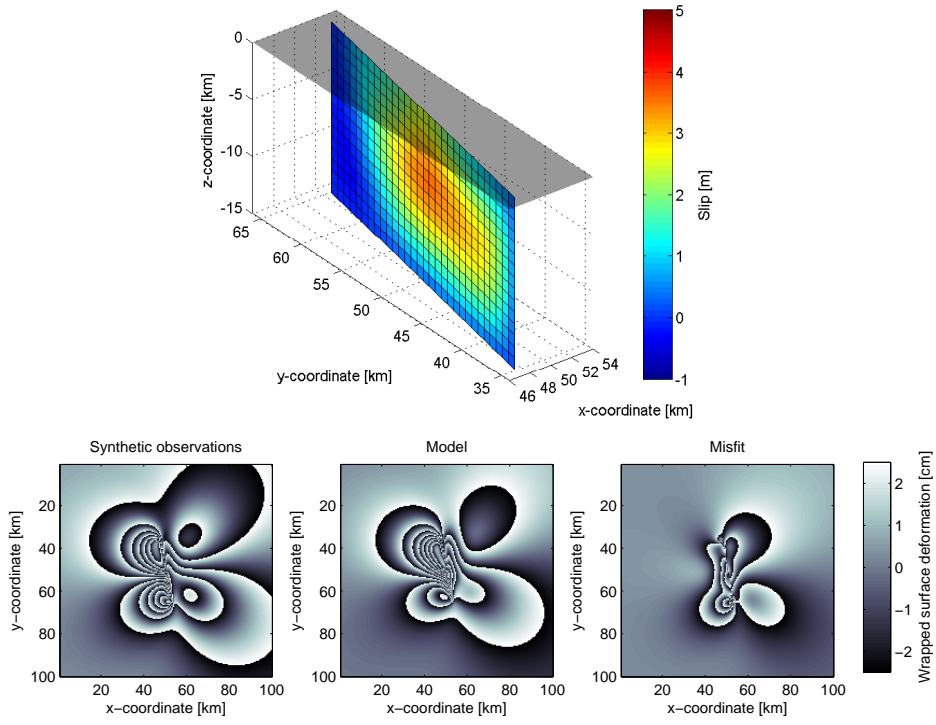


Figure A.7: Slip distribution and surface displacements estimated for the transform fault at  $\theta_{az} = 180^\circ$  with  $\Delta r = 10^\circ$ .

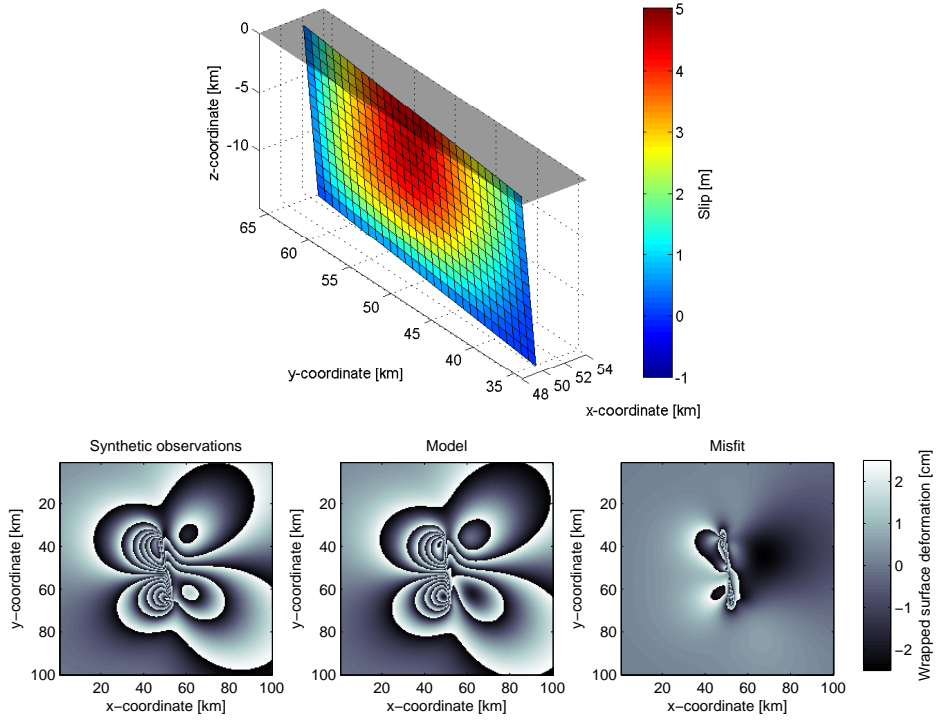


Figure A.8: Slip distribution and surface displacements estimated for the transform fault at  $\theta_{az} = 180^\circ$  with  $\Delta\alpha = -5^\circ$  and  $\Delta\delta = 5^\circ$ .

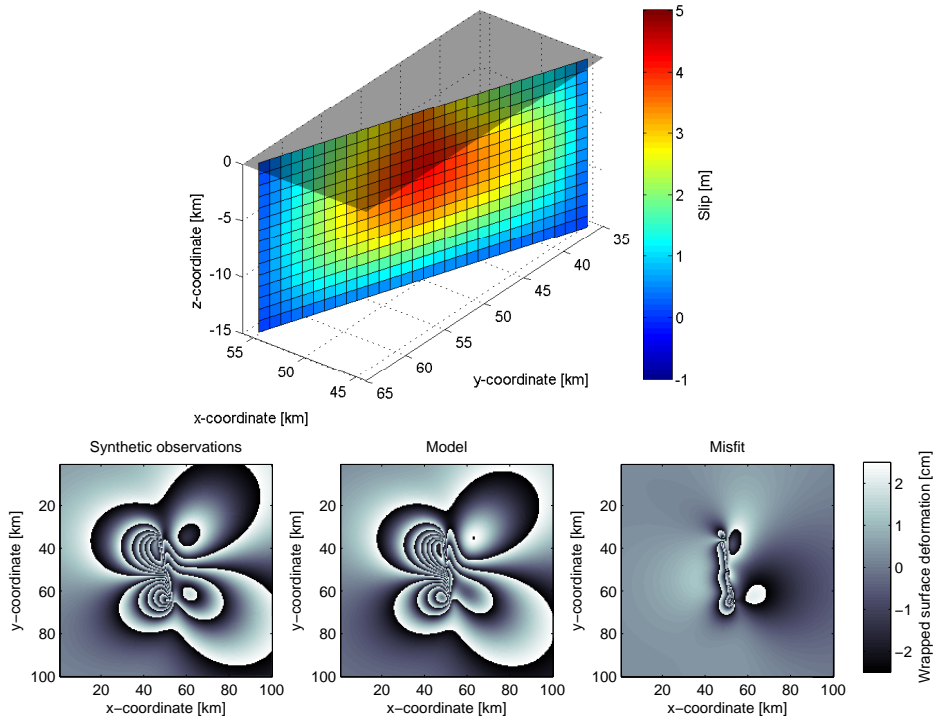


Figure A.9: Slip distribution and surface displacements estimated for the transform fault at  $\theta_{az} = 180^\circ$  with  $\Delta\alpha = -5^\circ$  and  $\Delta r = 5^\circ$ .

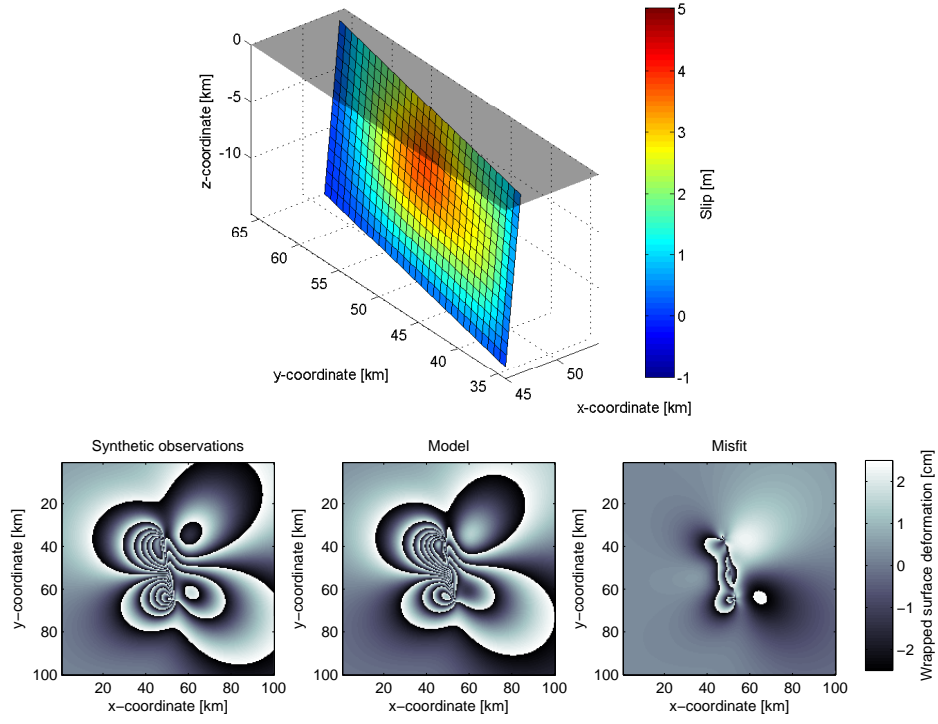


Figure A.10: Slip distribution and surface displacements estimated for the transform fault at  $\theta_{az} = 180^\circ$  with  $\Delta\delta = -5^\circ$  and  $\Delta r = 5^\circ$ .

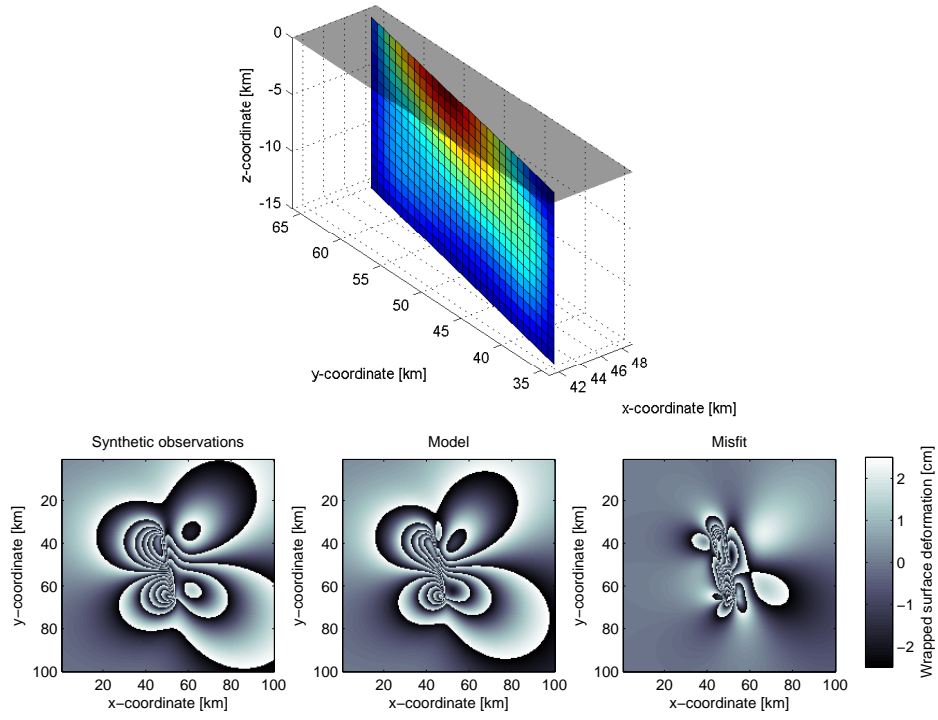


Figure A.11: Slip distribution and surface displacements estimated for the transform fault at  $\theta_{az} = 180^\circ$  with  $\Delta x = -5$  km.



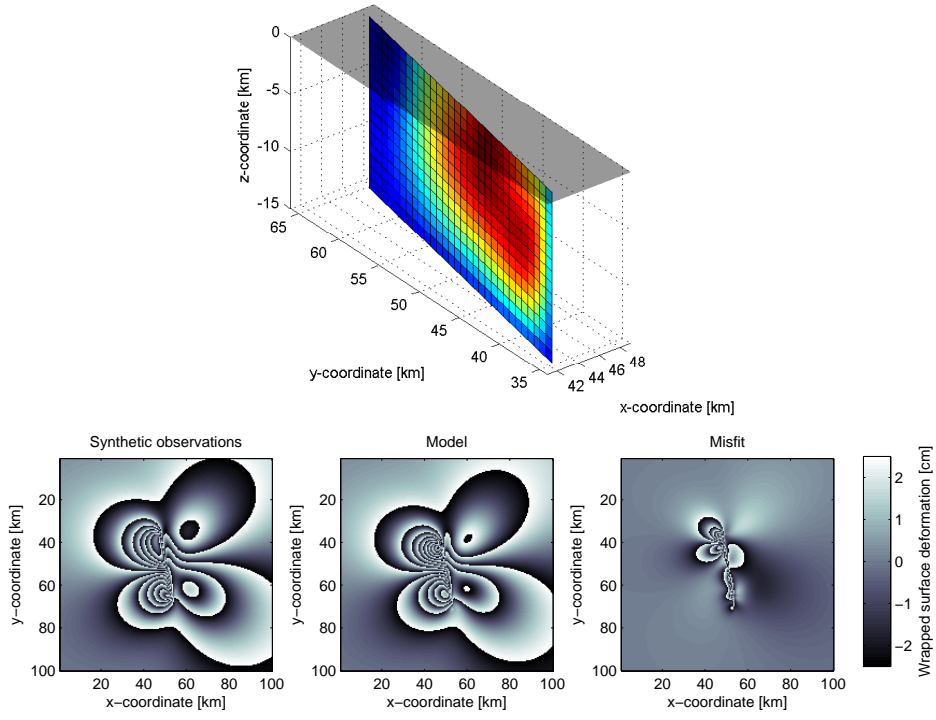


Figure A.12: Slip distribution and surface displacements estimated for the transform fault at  $\theta_{az} = 180^\circ$  with  $\Delta y = 5$  km.

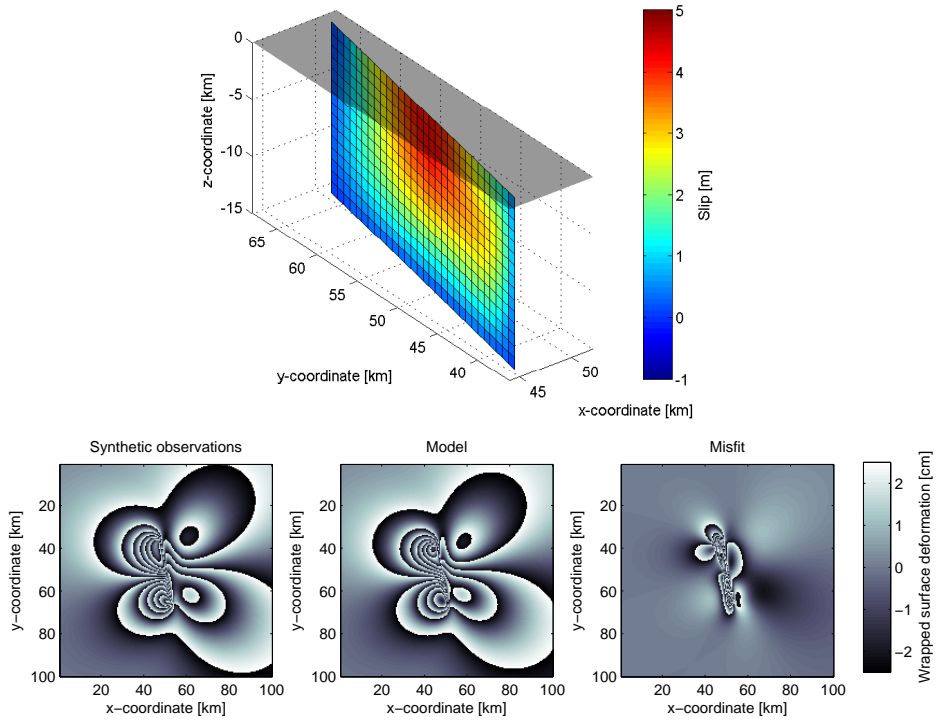


Figure A.13: Slip distribution and surface displacements estimated for the transform fault at  $\theta_{az} = 180^\circ$  with  $\Delta x = -2$  km and  $\Delta y = 2$  km.

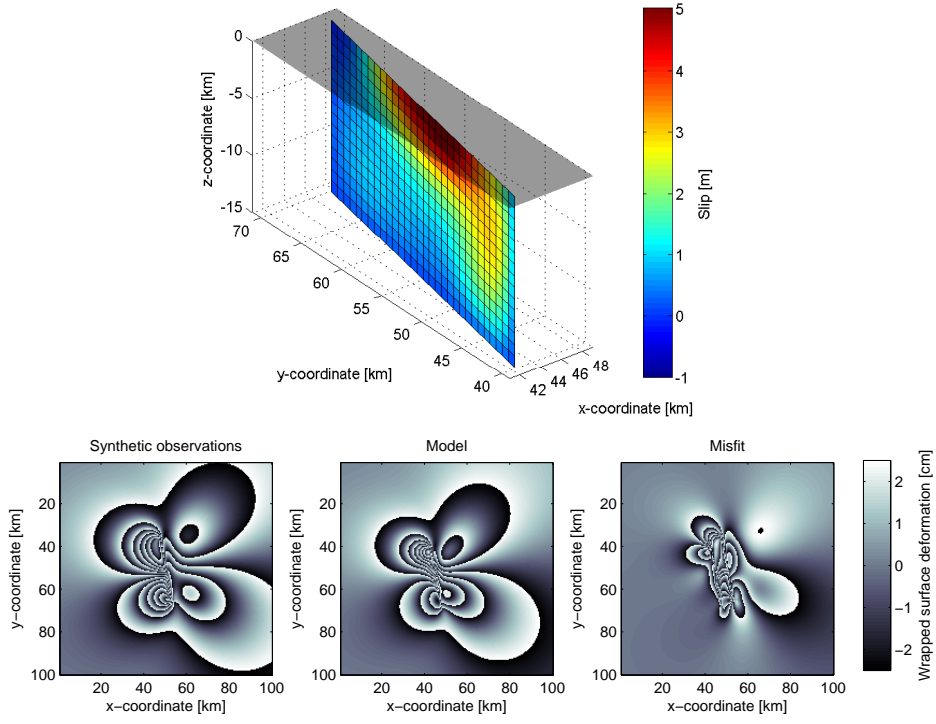


Figure A.14: Slip distribution and surface displacements estimated for the transform fault at  $\theta_{az} = 180^\circ$  with  $\Delta x = -5$  km and  $\Delta y = 5$  km.

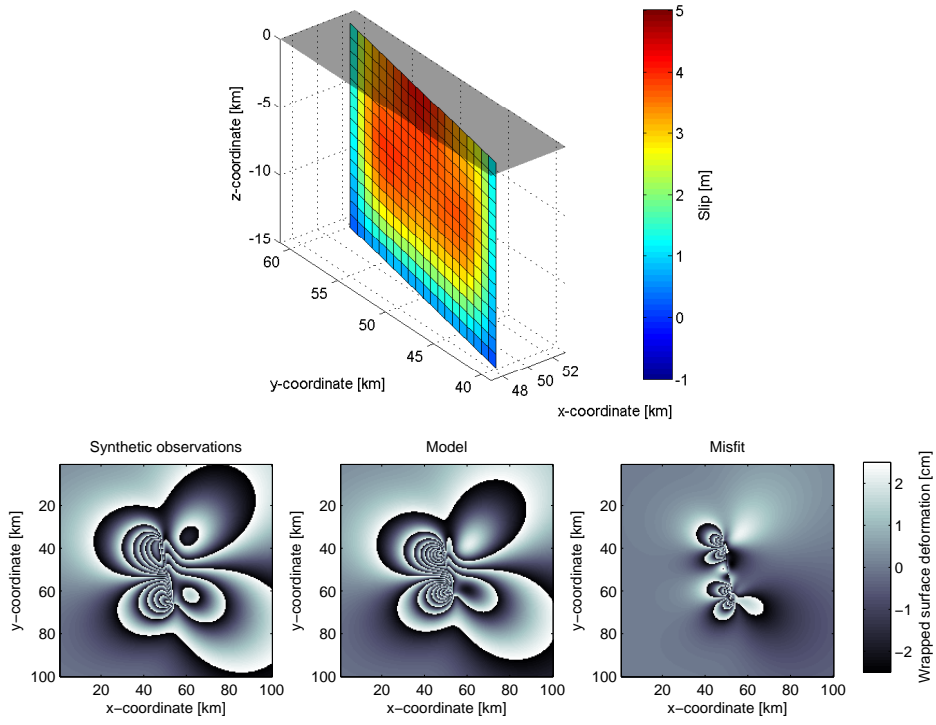


Figure A.15: Slip distribution and surface displacements estimated for the transform fault at  $\theta_{az} = 180^\circ$  with  $L = 20$  km.

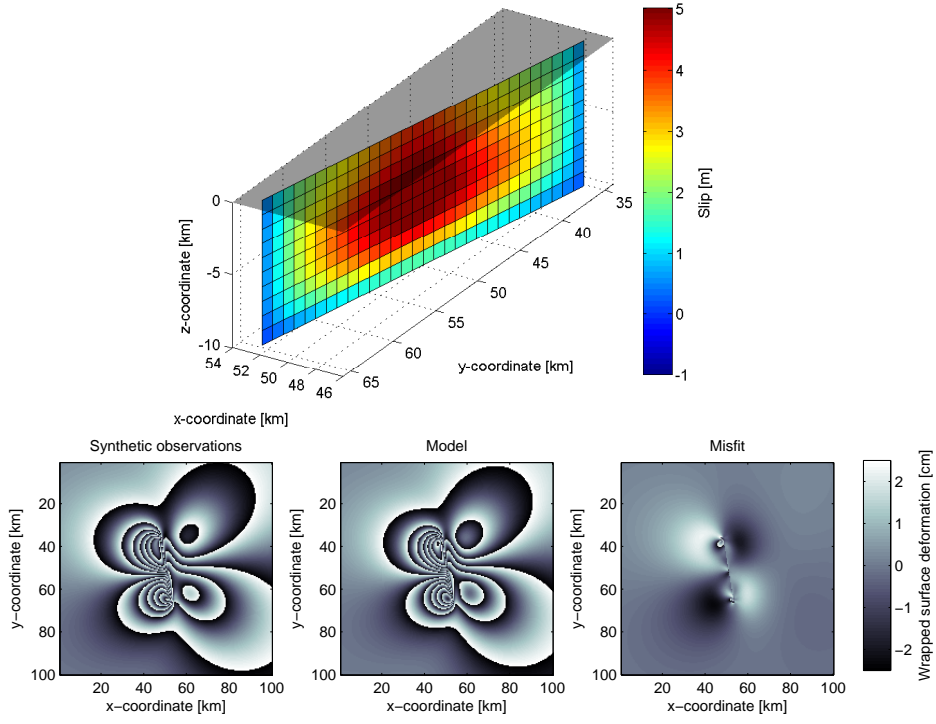


Figure A.16: Slip distribution and surface displacements estimated for the transform fault at  $\theta_{az} = 180^\circ$  with  $d_{max} = 10$  km.

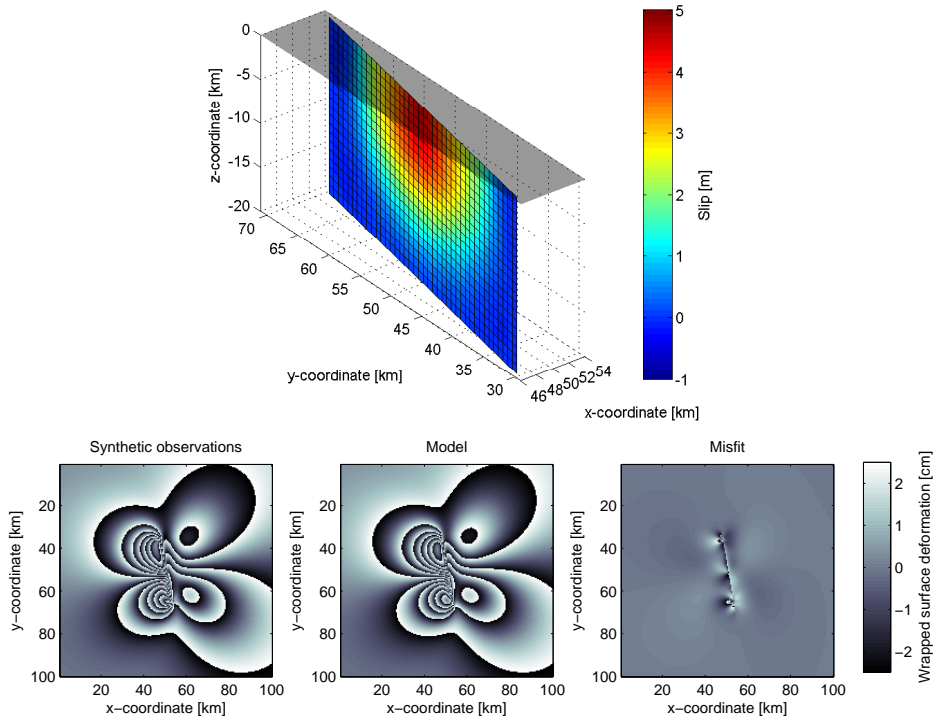


Figure A.17: Slip distribution and surface displacements estimated for the transform fault at  $\theta_{az} = 180^\circ$  with  $L = 40$  km and  $d_{max} = 20$  km.

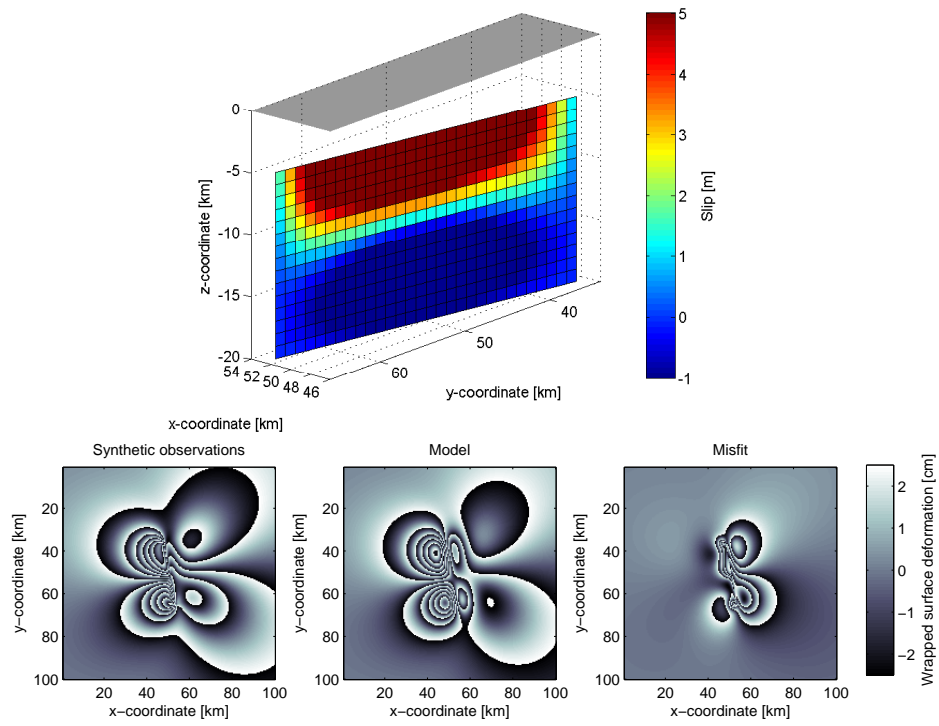


Figure A.18: Slip distribution and surface displacements estimated for the transform fault at  $\theta_{az} = 180^\circ$  with  $d_{min} = 5$  km.

## Appendix B

# Inversion results for Hector Mine with different data reduction

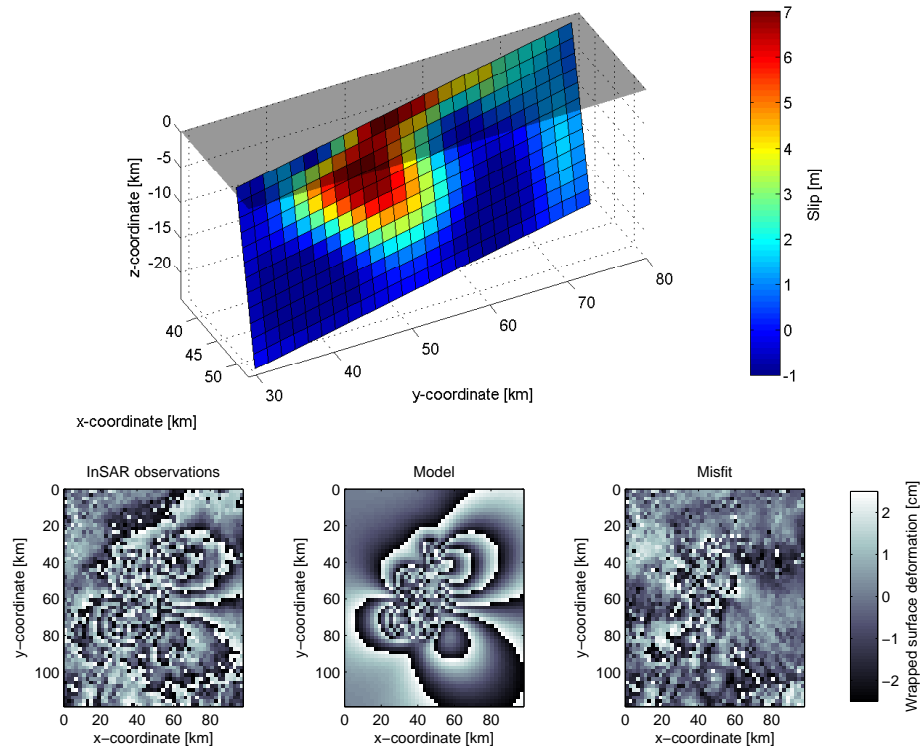


Figure B.1: Hector Mine slip distribution and surface displacements estimated with observations at a resolution of 2 km.

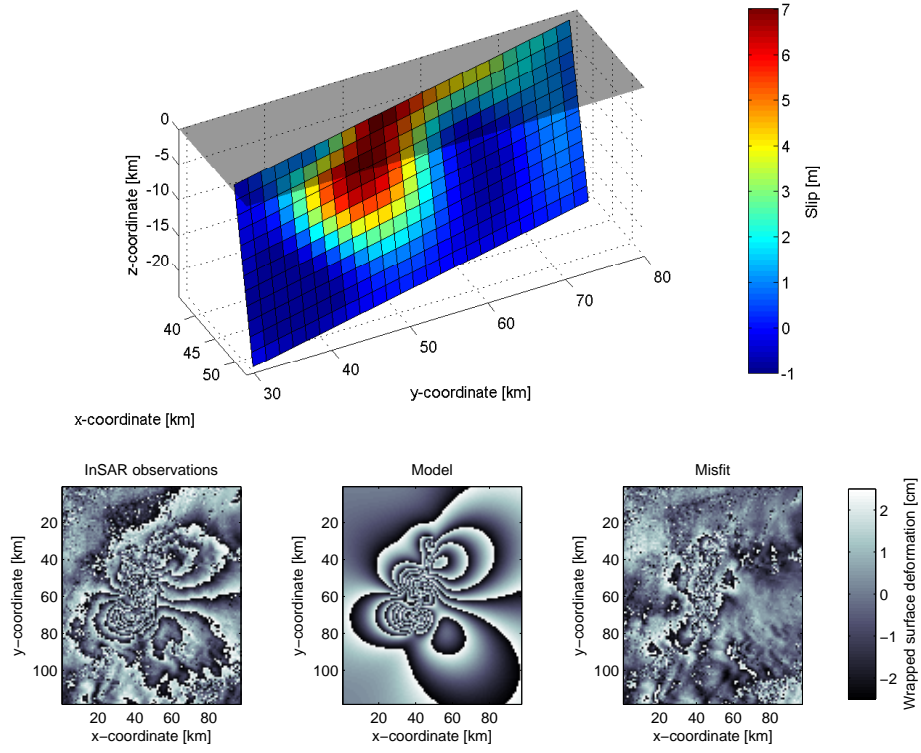


Figure B.2: Hector Mine slip distribution and surface displacements estimated with observations at a resolution of 1 km.

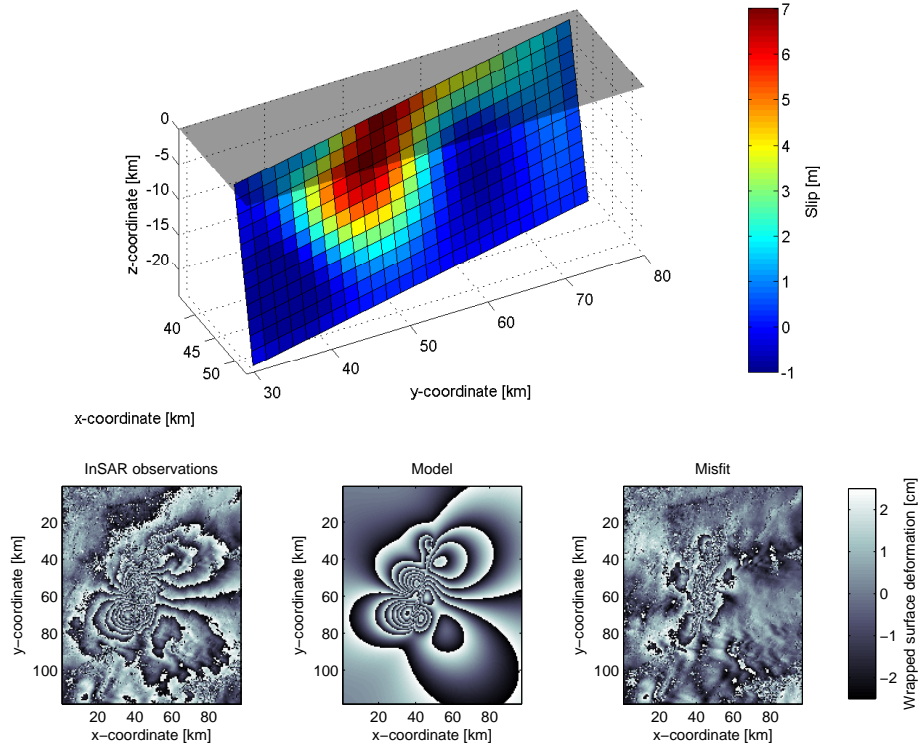


Figure B.3: Hector Mine slip distribution and surface displacements estimated with observations at a resolution of 640 m.

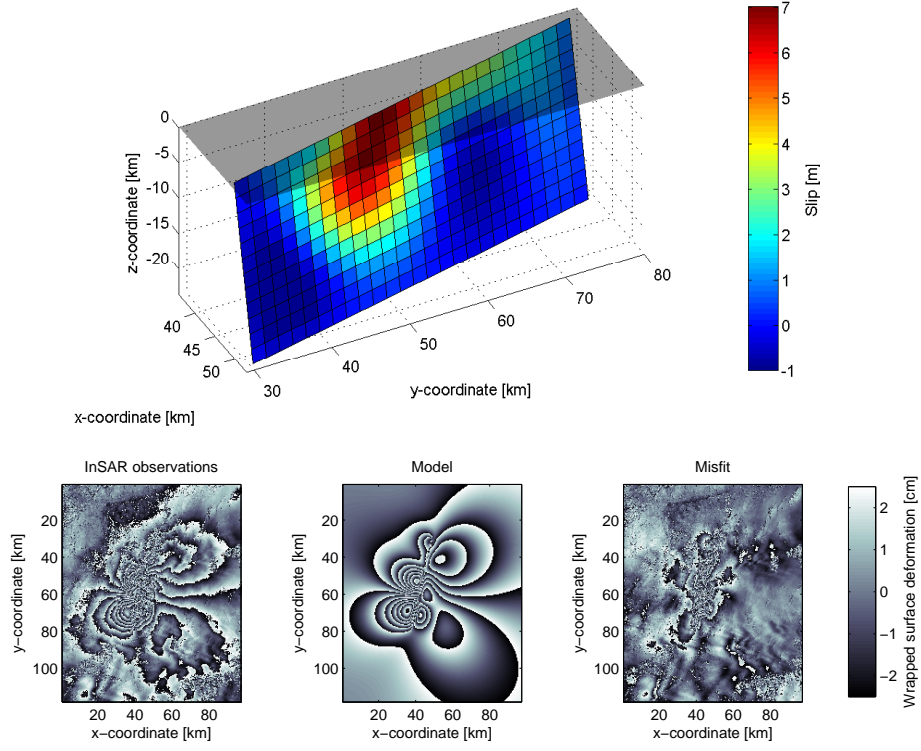


Figure B.4: Hector Mine slip distribution and surface displacements estimated with observations at a resolution of 500 m.

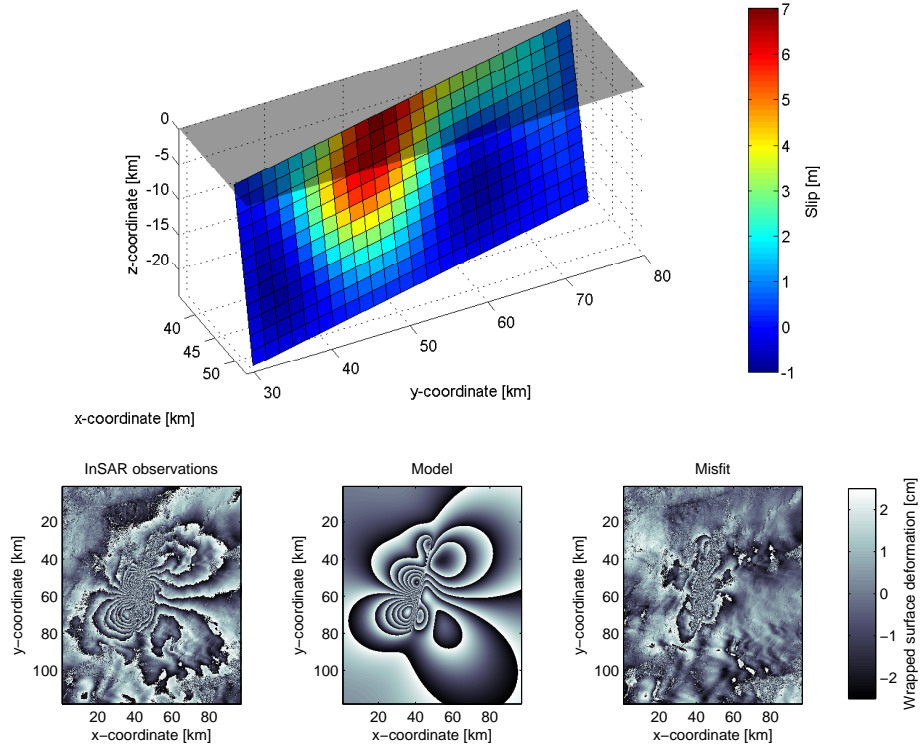


Figure B.5: Hector Mine slip distribution and surface displacements estimated with observations at a resolution of 300 m.



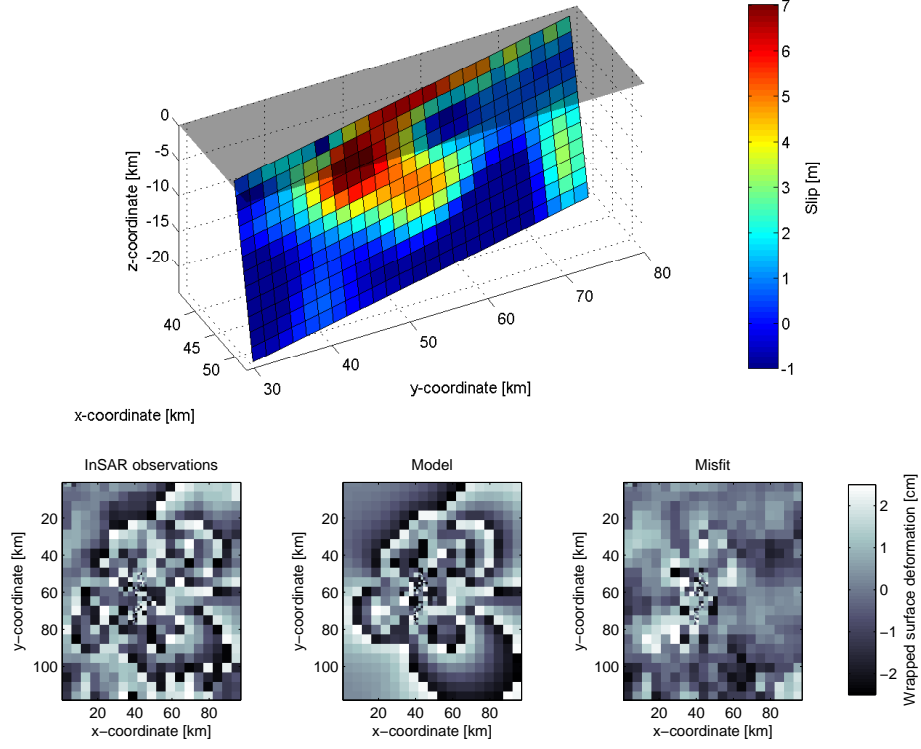


Figure B.6: Hector Mine slip distribution and surface displacements estimated with quad-tree partitioned observations with  $q_{min} = 8$  pixels (160 m resolution) and  $q_t = 28.3$  cm (10 original InSAR fringes).

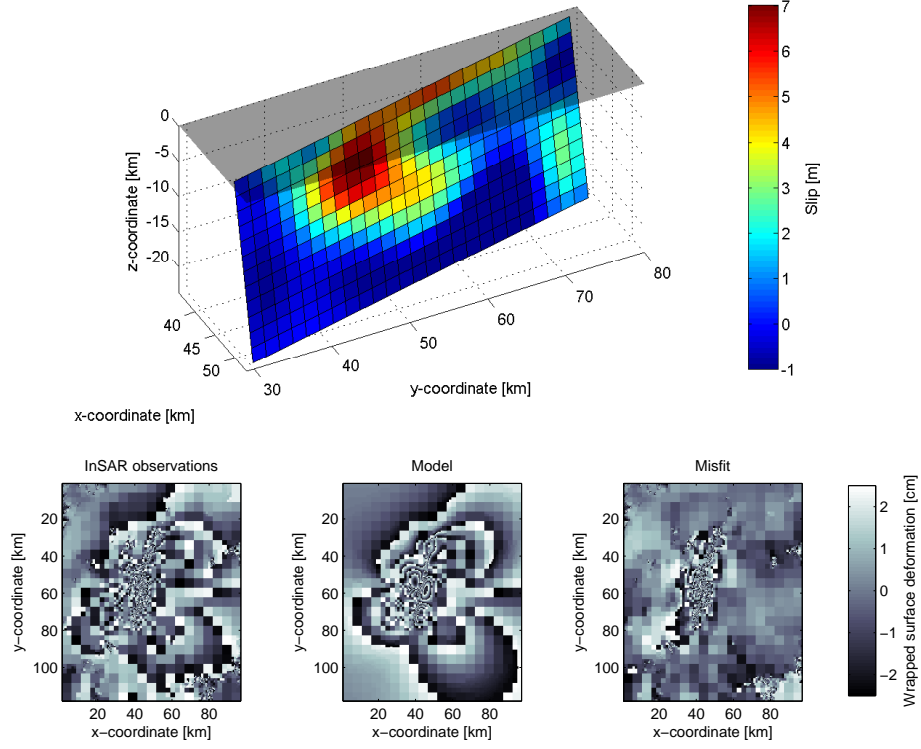


Figure B.7: Hector Mine slip distribution and surface displacements estimated with quad-tree partitioned observations with  $q_{min} = 8$  pixels (160 m resolution) and  $q_t = 10$  cm.



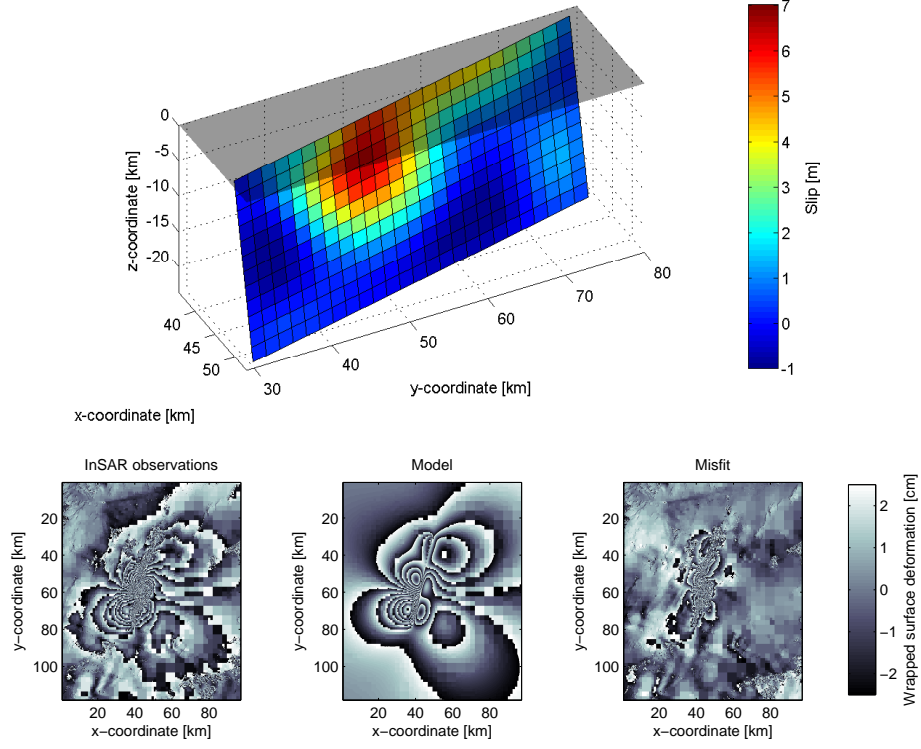


Figure B.8: Hector Mine slip distribution and surface displacements estimated with quad-tree partitioned observations with  $q_{min} = 8$  pixels (160 m resolution) and  $q_t = 5$  cm.

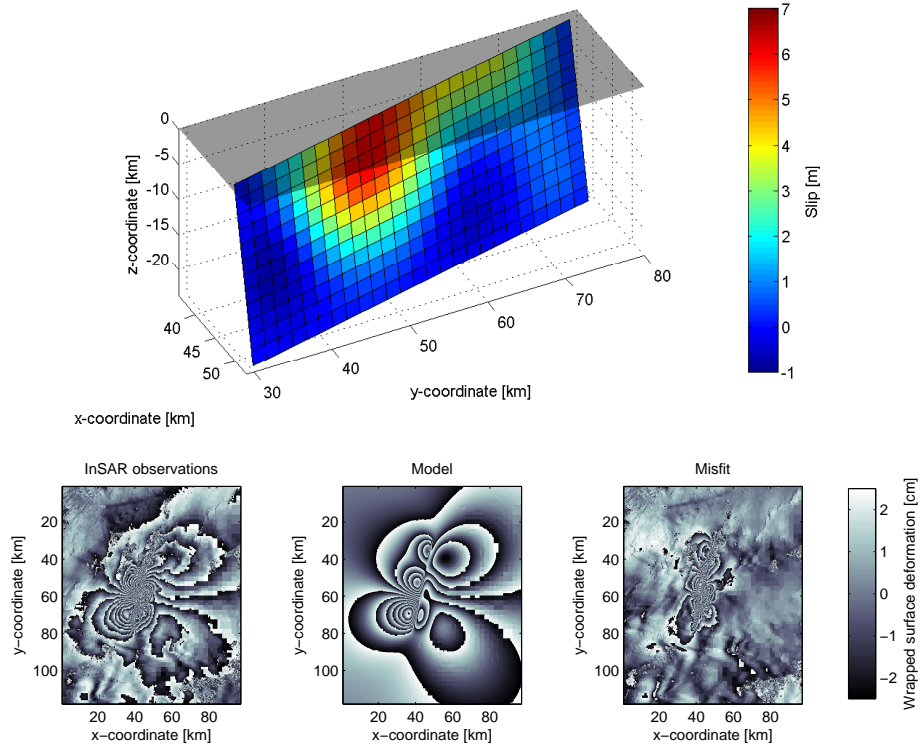


Figure B.9: Hector Mine slip distribution and surface displacements estimated with quad-tree partitioned observations with  $q_{min} = 8$  pixels (160 m resolution) and  $q_t = 2.83$  cm (1 original InSAR fringe).

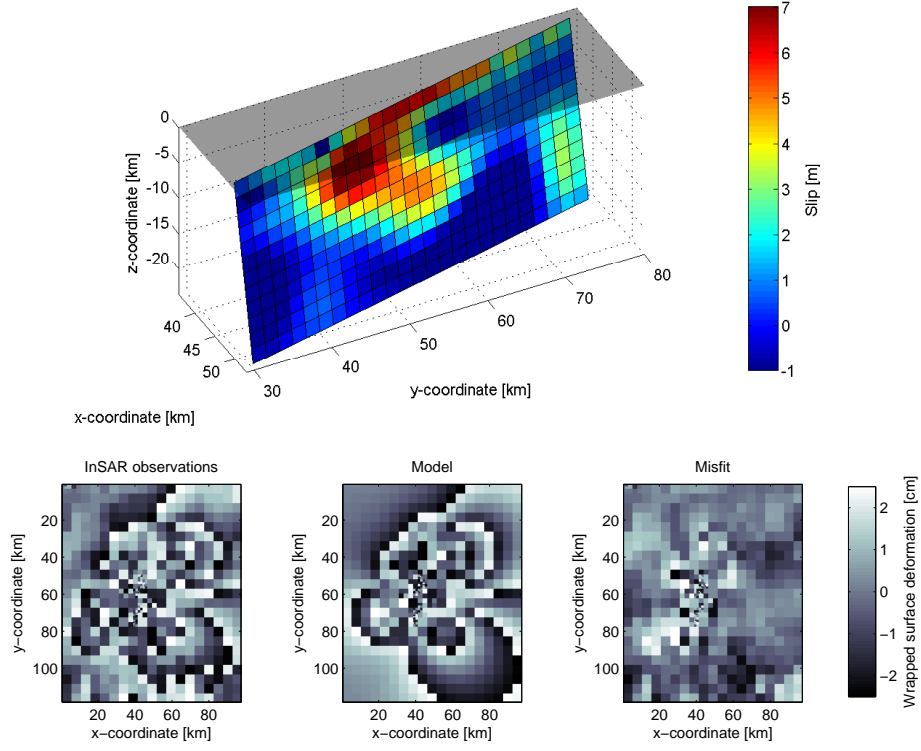


Figure B.10: Hector Mine slip distribution and surface displacements estimated with quad-tree partitioned observations with  $q_{min} = 32$  pixels (640 m resolution) and  $q_t = 28.3$  cm (10 original InSAR fringes).

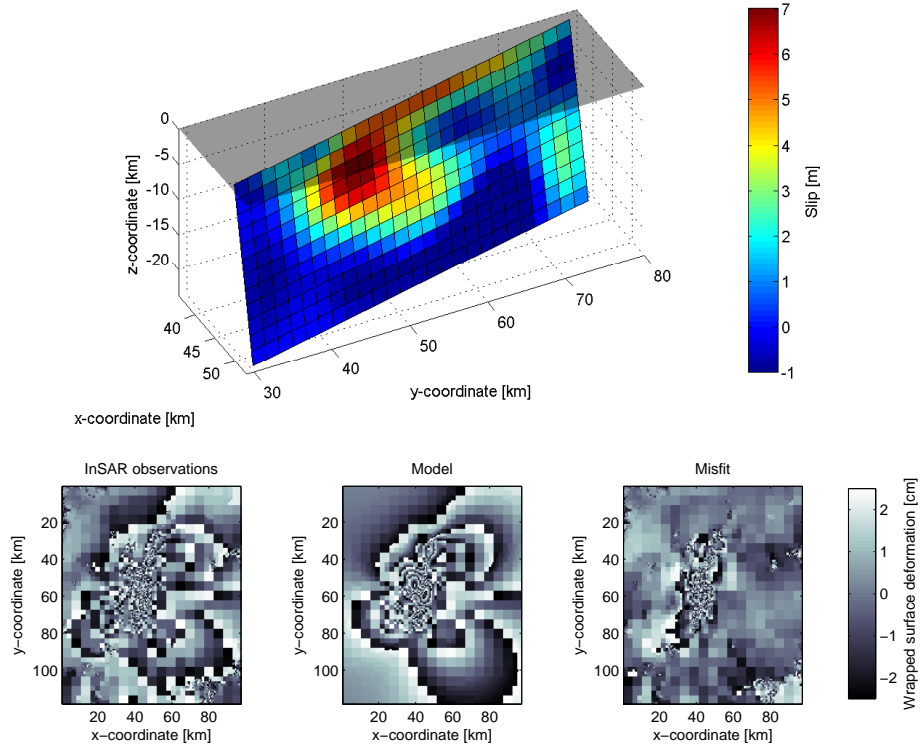


Figure B.11: Hector Mine slip distribution and surface displacements estimated with quad-tree partitioned observations with  $q_{min} = 32$  pixels (640 m resolution) and  $q_t = 10$  cm.

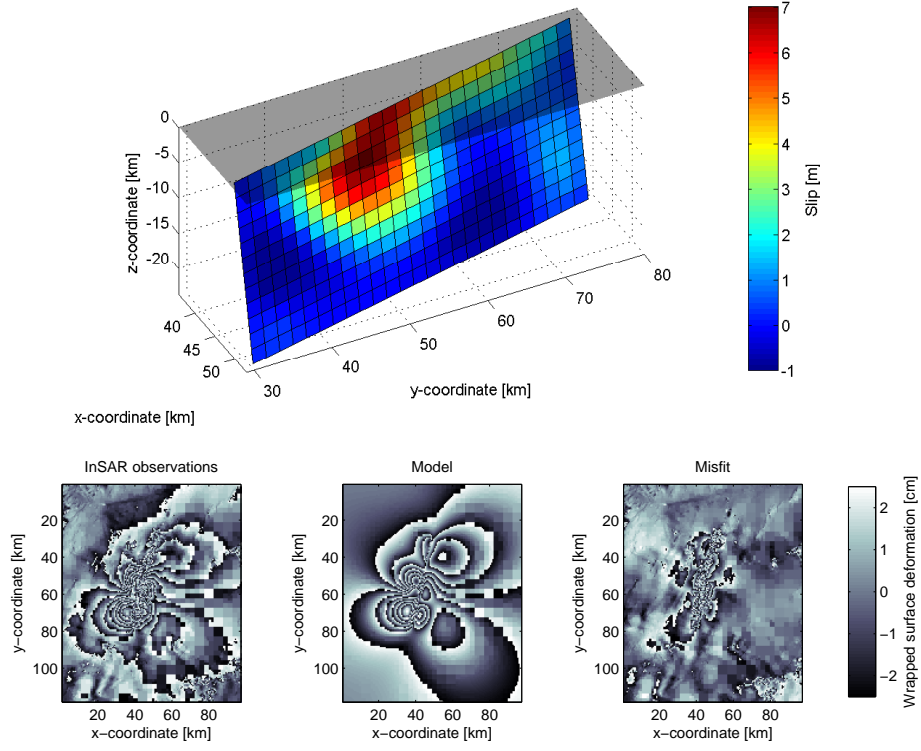


Figure B.12: Hector Mine slip distribution and surface displacements estimated with quad-tree partitioned observations with  $q_{min} = 32$  pixels (640 m resolution) and  $q_t = 5$  cm.

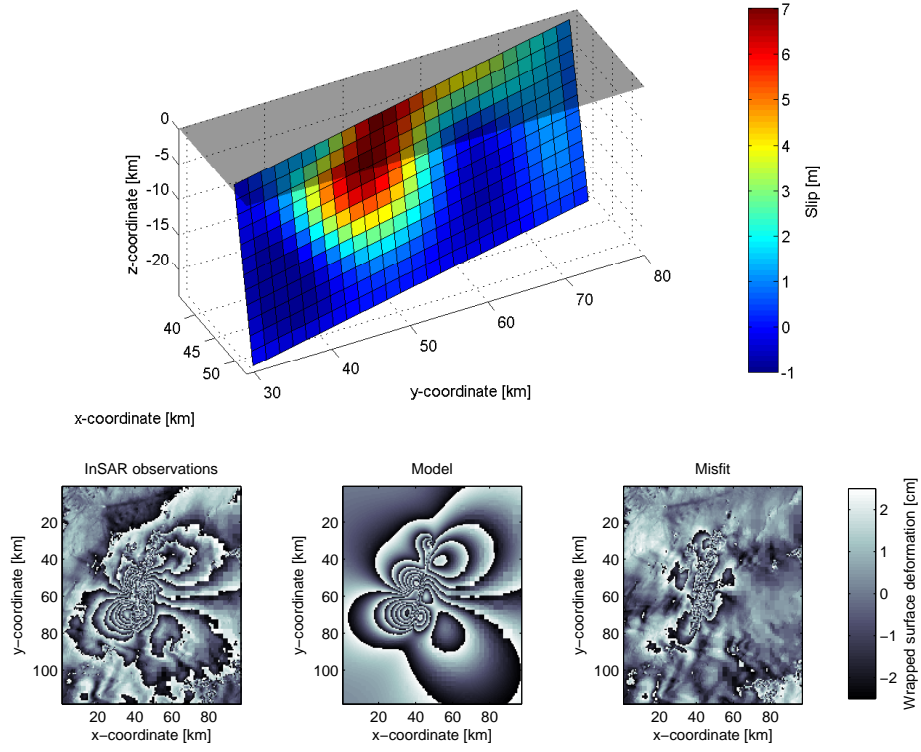
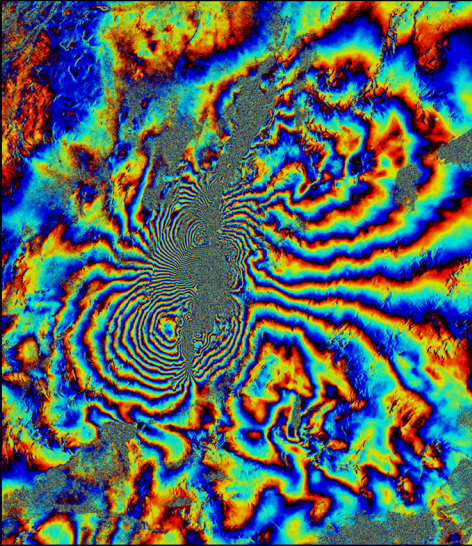


Figure B.13: Hector Mine slip distribution and surface displacements estimated with quad-tree partitioned observations with  $q_{min} = 32$  pixels (640 m resolution) and  $q_t = 2.83$  cm (1 original InSAR fringe).



The research presented in this M.Sc. thesis focuses on the inversion of earthquake slip distributions using Synthetic Aperture Radar Interferometry (InSAR). This space-borne remote sensing technique enables one to observe surface deformation caused by earthquakes. These observations can be used to estimate earthquake slip distributions. A slip distribution shows the variable amount of displacement on a fault plane that caused the earthquake. Slip distributions can be used to point out areas of potential earthquake hazard.

---

Sabine Put  
December 2008

M.Sc. Thesis Geomatics  
Department of Earth Observation and Space Systems  
Delft University of Technology